

2008

Photometric variability of Sun-like stars in the old open cluster M67

Ryan Wesley Tobin
Iowa State University

Follow this and additional works at: <https://lib.dr.iastate.edu/rtd>



Part of the [Astrophysics and Astronomy Commons](#)

Recommended Citation

Tobin, Ryan Wesley, "Photometric variability of Sun-like stars in the old open cluster M67" (2008). *Retrospective Theses and Dissertations*. 15295.
<https://lib.dr.iastate.edu/rtd/15295>

This Thesis is brought to you for free and open access by the Iowa State University Capstones, Theses and Dissertations at Iowa State University Digital Repository. It has been accepted for inclusion in Retrospective Theses and Dissertations by an authorized administrator of Iowa State University Digital Repository. For more information, please contact digirep@iastate.edu.

Photometric variability of Sun-like stars in the old open cluster M67

by

Ryan Wesley Tobin

A thesis submitted to the graduate faculty
in partial fulfillment of the requirements for the degree of
MASTER OF SCIENCE

Major: Astrophysics

Program of Study Committee:
Guillermo Gonzalez, Major Professor
Stephen J. Willson
James P. Vary
Charles R. Kerton

Iowa State University

Ames, Iowa

2008

Copyright © Ryan Wesley Tobin, 2008. All rights reserved.

UMI Number: 1453111



UMI Microform 1453111

Copyright 2008 by ProQuest Information and Learning Company.
All rights reserved. This microform edition is protected against
unauthorized copying under Title 17, United States Code.

ProQuest Information and Learning Company
300 North Zeeb Road
P.O. Box 1346
Ann Arbor, MI 48106-1346

TABLE OF CONTENTS

List of Figures	v
List of Tables	viii
Acknowledgements	ix
Abstract	x
Chapter 1. Introduction	1
1.1 Goals	1
1.2 Choosing a test 'sight'	2
1.2.1 Cluster versus Field	3
1.2.2 Open versus Globular	3
1.3 M67 as a Test Laboratory	5
1.4 Overview of Procedure	6
1.5 Outline of Thesis Sections	6
Chapter 2. History	8
2.1 Photographic & Photoelectric Studies	8
2.2 CCD Studies	11
Chapter 3. Observations	15
3.1 Observatory	15
3.1.1 Location	15
3.1.2 Light Gathering	16
3.2 Calibration Data and Standards	18
3.2.1 Linearity	18
3.2.2 Shutter Error	20
3.2.3 Biases and Flat Fields	22
3.2.4 Darks	23
3.2.5 Determination of Readnoise and Gain	23
3.3 Program of Observation	26
3.3.1 Positioning Field on CCD	26
3.3.2 Focusing	26
3.3.3 Exposure Times	28
3.3.4 Cadence	28
3.3.5 Biases	29
3.3.6 Flats	30
3.3.7 Organization and Application	31
Chapter 4. Analysis	33
4.1 Data Reduction in <i>IRAF</i>	33
4.1.1 Bias Subtraction	33

4.1.2 Low Count Flats	34
4.1.3 Accounting for Shutter Error	34
4.1.4 Flat Division	35
4.1.5 Standardization	36
4.2 Determining Magnitudes	36
4.2.1 Selecting Reference Images	36
4.2.2 <i>SExtractor</i> and <i>Astrometrica</i>	37
4.2.3 Least-Squares Fit	39
4.2.4 Balaguer-Núñez Matching	41
4.2.5 <i>Optimal Photometry</i>	43
4.3 Color Corrections	45
4.3.1 Preparation of Data	45
4.3.2 Theory of Color-Corrections	46
4.3.3 Method of Applying Corrections	49
4.4 Improving Precision	52
4.4.1 Ensemble Routine – Honeycutt 1992	52
4.4.2 <i>Ensemble Photometry</i> Program	53
4.5 Optimal versus Aperture	60
Chapter 5. Discussion of Results	62
5.1 Results	62
5.1.1 The Sun in M67	62
5.1.2 Color-Magnitude Diagram	63
5.1.3 Variability	67
5.2 The Sun-like M67	73
5.2.1 Define Sun-like	73
5.2.2 Solar-type Stars with Relatively-High Uncertainty	75
5.3 Single versus Binary	77
5.3.1 Uncertainties	77
5.3.2 RS CVn System 1046	78
5.4 Uncertainties and Errors	79
5.4.1 General Uncertainties	79
5.4.2 Propagation of Error	80
5.4.3 First-Order Extinction	89
Chapter 6. Conclusions	92
6.1 Summary of Research	92
6.1.1 Observations and Procedure	92
6.1.2 Variability	92
6.1.3 Small Research-Grade Telescope Limitations	93
6.2 Suggestions for Improvements	94
6.2.1 Longer Exposures	94
6.2.2 First-Order Extinction	94
6.2.3 Vignetting Correction	96
6.2.4 Longer Baseline	97

6.2.5 Focus	97
Appendix A. Mathematica Code for Least-Squares Analysis	99
Appendix B. C++ Code for Color-Correction	100
Appendix C. C++ Code for Categorization and Group Statistics	102
Bibliography	105

List of Figures

Figure 1.1 M67 Field of View. This image was taken using the V filter. North is up; East is left.	4
Figure 2.1 A plot from Montgomery et al. (1993). The solid lines are theoretical isochrones fit to the data set, each line representing a different possible age for the cluster.	12
Figure 3.1 Light pollution near Erwin W. Fick Observatory. Credit: P. Cinzano, F. Falchi, and C.D. Elvidge. Copyright Royal Astronomical Society. Reproduced from the Monthly Notices of the RAS by permission of Blackwell Science.	16
Figure 3.2 Transmission passbands for the B and V filters. B filter is in blue (left) and the V filter is in red (right).	17
Figure 3.3 Linearity Test – Variance is plotted versus mean count. Note the second linear regime starting near 26000 counts and the extreme turnoff near 42500 counts.	19
Figure 3.4 Images of a screen taken at different exposure times. Similar vignetting effects can be seen (the darkened corners) in both, but on the left the central intensity decreases radially due to shutter error.	21
Figure 3.5 Shutter Test – Normalized standard deviation is plotted versus exposure time. Note that the curves are not aligned due to differences in transmission fraction.	21
Figure 3.6 Noisemodel Output – Variance is plotted versus mean counts. The solid curve indicates the location of the median and the dotted curves represent the values for ± 2 standard deviations.	25
Figure 4.1 Image in B of the field of M67 with an overlay of the detected star locations in red circles. The axes are in units of pixels. Note that there are no circles around the brightest stars.	42
Figure 4.2 Extinction coefficient versus wavelength plot for Landolt standard stars from the Cerro Tololo Interamerican Observatory in Chile. Courtesy of Stritzinger et al., 2005.	46
Figure 4.3 Plot showing the instrumental color versus standard color. Orange squares signify the aperture catalog data, and green circles signify the optimal catalog data.	51
Figure 4.4 Plot of standard deviation versus magnitude with parabolic fit from B filter data. Variable stars will appear at higher standard deviations than the typical star. Note the outlier star at magnitude 14.5 has a well-known photometric variability.	56
Figure 4.5 Same plot as Figure 4.4, only with a log scale. Here you can see the width of the scatter around the parabolic fit.	57
Figure 4.6 Standard deviation versus magnitude plot of the B filter data set. Multiple variability thresholds are shown, with designated variables in separate colors.	58

- Figure 4.7 Standard deviation versus magnitude plot of the V filter data set. Multiple variability thresholds shown, with designated variables in different colors. 58
- Figure 4.8 Standard deviation versus magnitude (without designated variable stars) diagrams from the optimal catalog output of *Ensemble Photometry*. Blue squares are data points from the B filter and red circles are data points from the V filter. Note the large scatter of the data, such that hardly any trend is noticeable. 60
- Figure 4.9 Standard deviation versus magnitude (without designated variable stars) diagrams from the aperture catalog output of *Ensemble Photometry*. Blue squares are data points from the B filter and red circles are data points from the V filter. Note the gap in the B filter data between magnitudes 14 and 15.6 is from setting the variability threshold too low, such that all stars near the bottom of the fitted parabola are designated variables. 61
- Figure 5.1 CMD of all stars in our field-of-view. The Sun is labeled with a filled black circle and designated variable stars are marked with an 'X'. 64
- Figure 5.2 CMD of cluster member stars. The Sun is marked by a filled black circle, and designated variable stars are marked with an 'X'. The 'overall contraction phase' and binary sequence are visible. 64
- Figure 5.3 Labeled CMD. 65
- Figure 5.4 A closer look at the Turn Off reveals the bend (overall contraction phase) caused by convective core mixing in massive stars. The line is a guide for the reader and is similar to the shape and location of a plotted theoretical isochrone. 65
- Figure 5.5 CMD of cluster members with error bars. The error bars in some cases can indicate a variable star. The unusual size of the error bar at the bottom of the turnoff indicates a large amplitude variable star at that location. 66
- Figure 5.6 Light curve of W UMa system labeled 1176. Note the 0.02 difference in maximums and 0.09 difference in minimums. 68
- Figure 5.7 Light curve of W UMa system labeled 1352. Because of the consistently varying properties of the system, the light curve has discrepant points. There is a hint of flat bottoms indicating total eclipses. 69
- Figure 5.8 Light curve of the W UMa system labeled 777. Note that the precision is not much better than the amplitude of variability. 70
- Figure 5.9 Light curve for the variable system labeled 905. This system is peculiar in its location and its variation of unknown origin. Note the variation of data points and error bars. 71
- Figure 5.10 Variable star locations. Notice that these stars are well-separated from other stars. Axes units are in pixels. 72
- Figure 5.11 CMD with variables marked and box indicating the definition of Sun-like stars. The black filled circle is the Sun and designated variables are both marked with an 'x' and labeled. 74

- Figure 5.12 A light curve showing the variability of the RS CVn system. The horizontal axis is in Julian date, and the vertical axis is in B magnitude. Note that the light curve varies by about 107 millimagnitudes. 78
- Figure 5.13 Plot of scintillation noise in millimagnitudes versus airmass. Typical airmass for our observations is closer to 1.2, and never exceeds 2.0. The top curve is using the V filter characteristics, whereas the bottom curve is using the B filter characteristics. 86
- Figure 5.14 Sigma versus magnitude plot. Vertical axis is in millimagnitudes. Note that there are several curves, each represent a different background sky count per pixel. Higher background sky count per pixel values result in the leftmost curve, whereas lower count per pixel values result in the rightmost curve. 87
- Figure 5.15 Standard deviation versus magnitude plot. The black line is the *Ensemble Photometry* parabola that is fit to the data. The blue curve (on top) is the estimate of error using the highest sky counts per pixel. The pink curve (on bottom) is the estimate of error using the lowest sky counts per pixel. 88
- Figure 6.1 Standard deviation versus magnitude plot. The black curve is the parabola fit produced by *Ensemble Photometry*. The blue curve (top) is a theoretical model of where the data should be located during a full moon. The pink curve (middle) models where the data is expected for a clear night when the moon is not bright. The green curve (bottom) is the expected location of data for a clear, moonless night using the same conditions as the pink curve, except it uses a 4-minute exposure (double the original exposure time). 95

List of Tables

Table 1.1	Properties of M67 (NGC 2682)	5
Table 3.1	Observations	27
Table 3.2	Master Flat Combinations	31
Table 5.1	Designated Variable Stars	67
Table 5.2	Extinction Effect	90

Acknowledgements

There are many people that have helped me along the way. Both in success and in failure, these people were there to help when help was needed:

First, and foremost, I would like to thank my advisor, Guillermo Gonzalez, whose straightforward attitude, experience, patience and guidance was never less than I needed. For always mixing the bad with some good, for helping me stay on track and for always being available, thank you.

Because all of the late nights, long hours, and inconsistent schedules take a larger toll on her, I would especially like to thank my wife, Amy for her love and support. For all of the little things, thank you.

Special thanks should go to Joshua Anderson and Daniel Risse for helping me when Linux fails and C++ codes misbehave. Without your help, this thesis would be stuck in a segmentation fault.

Others, whose support makes this thesis possible include: Joseph Eitter, for observing when I could not; Lee Anne Willson and Steven D. Kawaler, for answering even the small, irrelevant questions; and Michelle Hartwell and Tom Stroman, without whom I would run in fear.

Abstract

Few physical processes can affect the earth's climate on a global scale. The variability of the Sun is one such process. The Sun is known to vary by about 0.1% due to Sunspots and other surface activity. We do not yet know whether the Sun's variability is normal. Using the well-known properties of the old open cluster M67, we look for variations in Sun-like stars.

In this thesis, we present the results of observation, calibration, correction and analysis of stars in M67. We focus on Sun-like stars and binary systems. We also determine the limits of observation using a small research-grade telescope.

We find several known variable stars with comparable amplitudes of variability. Our precision is as high as 10 millimagnitudes, ranging 10-20 for Sun-like stars. Variability is detected as low as 20 millimagnitudes in amplitude. Our current precision, however, fails to detect solar-like variations.

Chapter 1. Introduction

Few processes can have an effect on the Earth on a global scale. One such process is the total luminosity output from the Sun. Changes in the Earth's climate have been linked to the Sun's variable irradiances (Lean & Rind 2001). The total luminosity of the Sun varies on nightly to century time-scales (Lockwood et al. 1997; Pap et al. 1999). By observing variability in stars like the Sun, we can learn about typical stellar behavior. Understanding where the Sun fits among Sun-like stars can lead to better predictions of the Sun's variability, including solar flares and prominences, over the coming decades. For astrobiological purposes, it is also helpful to know if the Sun is anomalous in its level of variability.

1.1 Goals

In this research, we examine the small-timescale variability of stars similar to the Sun. Observations of the Sun show variability in timescales from minutes to the years that make up the Solar Cycle (Lockwood et al. 1997; Pap et al. 1999). Our project, however, lasts only one season; therefore it is only sensitive to nightly to monthly variability timescales.

Our primary goal is to examine broadband brightness fluctuations due to stellar activity cycles, e.g. starspots rotating into and out of view. Giampapa et al. (2000) reported that only 30% of Sun-like stars in M67 exhibit activity that is unusual for the Sun. So the effect of starspots should be similar to that of

sunspots. Willson et al. (1981) of the Solar Maximum Mission notes that sunspots cause dimming of up to 0.2% in total luminosity. Pap et al. (1999) note that this effect is larger at shorter wavelengths. They also note that the strongest modulation of the Sun's amplitude of variability is an effect of sunspots across the surface.

It has been suggested that variability of stars is linked to binarity (van den Berg et al. 2002). Stassun et al. (2002) reports that 14 of 29 cluster member variable stars are in known binary systems. This suggests that the differences of variability of these systems is not clear. In light of this, we will focus our attention on how the variability is different between stars that are in known binary systems and single stars.

A final goal of this study is to probe the usefulness of a small research-grade telescope for millimagnitude photometry. Some concern is that the telescope is located too close to the city of Des Moines for reasonable background sky noise levels. Another concern is that the telescope is not large enough to provide high-precision photometry. Understanding the limit of this photometry, whether it is limited by the telescope or by the location, will be useful for future observations with this equipment.

1.2 Choosing a test “sight”

The night sky is filled with stars. Choosing which star to observe may seem trivial, but it can be difficult. Most of the stars that you see are in the solar neighborhood. Though many of them fall on the main sequence, most are not

particularly Sun-like. Many Sun-like stars are observable with a telescope.

However, it is not clear exactly which stars are best to observe.

1.2.1 Cluster versus Field

Since we want to study stars that are similar to the Sun, we should look for stars with a similar spectral type, age and composition. For field stars, age can be difficult to determine accurately. Clusters generally do not have such a problem. If we were to use a star cluster, we can determine age with much less uncertainty by studying the cluster members' locations on the Hertzsprung-Russell diagram. Furthermore, because these stars are close together on the sky, we only need a single line-of-sight, whereas with field stars, in order to find several stars similar to the Sun, we would need a line-of-sight for almost every star. For field stars, however, differences in extinction due to differences in air mass cannot be neglected. This is discussed in detail in Chapter 5.

Current studies of field stars are plagued by variable comparison stars. Lockwood et al. (2007) notes that too many comparison stars results in nearly all of the observing time is spent on calibration stars and almost none is spent on the science object. They go on to note that the level of variability is much higher in field stars than in the Sun, and that the Sun appears to be an outlier in variability with respects to other Sun-like stars.

1.2.2 Open versus Globular

With all of the star clusters available to us, we need to find clusters that are populous, nearby, and similar in age and composition to the Sun. The typical globular cluster is much older and farther than the typical open cluster. Globular

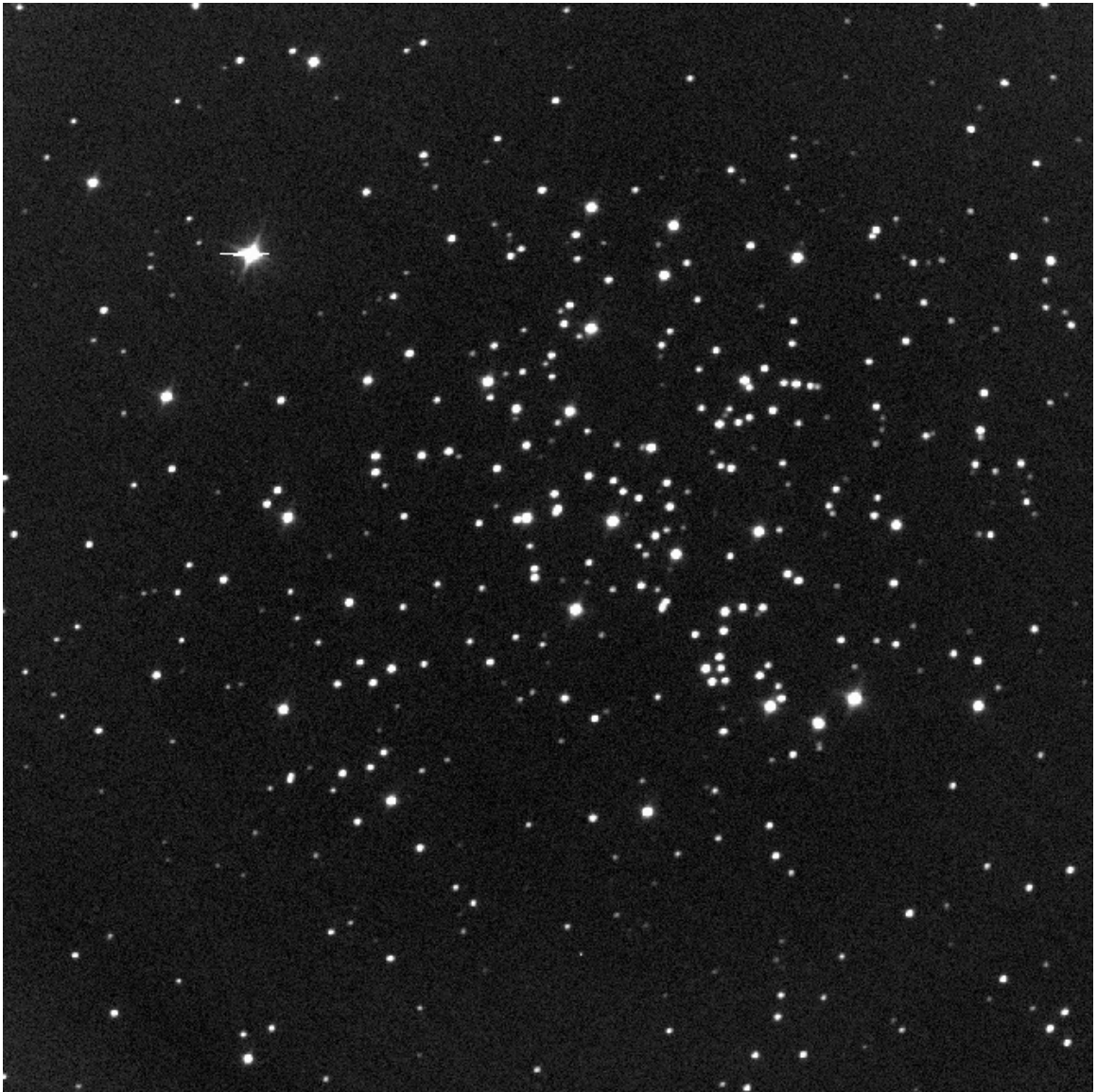


Figure 1.1 – M67 Field of View. This image was taken using the V filter. North is up; East is left.

clusters are also much denser, permitting ground-based photometry of only the stars in the sparser outer regions. On the other hand, it is harder to determine which stars are members and which are foreground or background field stars for an open cluster. The ideal case is to have an open cluster that is sufficiently far from the plane of the galaxy in order to limit the density of contaminating field stars. This same open cluster should be not so close that the cluster members

cover too large of an area on the sky, but close enough that the stars are still bright, and, of course, it should have plenty of member stars.

1.3 M67 as a Test Laboratory

Out of the small list of close open clusters, there is one that best satisfies the requirements for a test subject. The open cluster M67 fulfills all of these requirements, and it will be our stellar laboratory. We should note that at least one study has referred to M67 cluster members as the “paradigm sample for

Table 1.1 Properties of M67 (NGC 2682)

Property	Value	Source
Right Ascension (Ep. 2000.0)	08 ^h 51 ^m 23. ^s 3	Yadav et al. (2008)
Declination (Ep. 2000.0)	+11° 49' 02"	Yadav et al. (2008)
Distance Modulus	(m-M) ₀ = 9.7 ± 0.2	Balaguer-Núñez et al. (2007)
Galactic Longitude	215.688°	Yadav et al. (2008)
Galactic Latitude	31.923°	Yadav et al. (2008)
Proper Motion	-6.51 ± 0.30 mas yr ⁻¹ (α) -4.54 ± 0.28 mas yr ⁻¹ (δ)	Loktin (2003) Loktin (2003)
Radial Velocity	33.67 ± 0.09 km s ⁻¹	Yadav et al. (2008)
Reddening	E(B-V) = 0.04 ± 0.004	Taylor et al. (2007)
Metallicity	[Fe/H] = 0.03 ± 0.01	Randich et al. (2006)
Angular Size	θ = 25 arcminutes	Tadross et al. (2002)
Age	4.2 ± 0.2 Gyr	Balaguer-Núñez et al. (2007)

studies of structure and evolution of Population I solar-age stars” (Montgomery et al. 1993). We should learn a little bit about it. The cluster is shown in Figure 1.1 using an image from April 2nd, 2007, V filter image. Notice the “dipper” asterism of four bright stars in a curved pattern that make up the “handle” and the five bright stars in the shape of a trapezoid on its side (to the right and slightly down

from the center of the image. M67 is located in the constellation Cancer. This open cluster is also known as NGC 2682 and C 0847+120. The rest of its properties are summarized in Table 1.1.

1.4 Overview of the Expected Procedure

We start by collecting the data, and we will reduce it with the *Image Reduction and Analysis Facility* (hereafter *IRAF*). Using *SExtractor* and *Astrometrica*, we will identify stars on the images and determine their equatorial positions. We will then color-correct the photometry. Then we will use Tim Naylor's *Optimal Photometry* code to extract optimal and aperture magnitudes from each image. After this, the program *Ensemble Photometry* will be used to improve the certainty of the data. This program will also identify (and remove) variable stars to improve the differential photometric precision of the non-variable stars in an iterative procedure. The last part of the procedure is to combine the data from each night to produce a more accurate night-to-night data set.

1.5 Outline of Thesis sections

The remaining chapters are described in a brief synopsis. Chapter two describes the literature background on the subject of the open cluster M67. It also contains relevant information on the variability of the Sun, describing how previous studies related Sun-like stars from other sources to the Sun.

Chapter three describes the location and method of observations. It also describes calibrations of the optical systems. The chapter explains what the systematic sources of error are and how they are corrected. This chapter also discusses the organization of the material.

The fourth chapter is the general analysis of the photometry. It starts by extracting photometry and transforming it to the standard system. The chapter will discuss how to improve uncertainties and how the variables are designated.

Chapter five discusses the variability of stars outright. This chapter is designed to focus on and discuss the goals in Section 1.2. This chapter will also report in depth on the errors of the method. Any parts that are left out due to time constraints will be addressed here.

To conclude the thesis, the sixth chapter contains a brief synopsis of previous work. A summary of the current work is presented with error estimates. The final portion of this chapter will be devoted to future work and advanced measures that would improve the method and the findings.

Chapter 2. History

M67 is one of the most well-studied open clusters. In this chapter, we review previous studies of the cluster, focusing primarily on broadband studies.

2.1 Photographic and Photoelectric Studies

Prior to the advent of the charge couple device (hereafter CCD) camera, there were two primary ways of recording telescopic observations. The first is a simple photograph, which, at best, was accurate to about 0.01 magnitudes (Birney et al. 2006). The second was a photoelectric detector. This kind of detector allowed for a much easier use of filters to measure only the light of a certain color. The photomultiplier tube, is more sensitive and has broader spectral response than the photographic plate. With the improved technology, there was also an improvement in the photometric standard. Johnson and Morgan (1953) developed a new standard in three colors (UBV). Future broadband color studies would be based on this original standard.

The new standards and technology revitalized interest in studies of star clusters, specifically in three-color studies. Johnson and Sandage (1955) used three-color studies to develop a standard sequence useful for conversion between photographic and photoelectric magnitudes for the M67 field. As well as studying clusters in three colors, a general and relative color-magnitude diagram (hereafter CMD) was produced. Johnson and Sandage (1955) noted that M67's

main sequence terminated fainter and redder than many other clusters, and a relative age was suggested to be around 5 Gyr.

Further studies using three colors included the ability to estimate and remove the interstellar reddening. Eggen and Sandage (1964) found that the reddening was $E(B-V)=0.06$. With a known reddening value, they went on to determine a general distance of about 752 ± 70 parsecs.

Racine (1971) used advances in technology to refine our knowledge of the cluster's properties. She noted that there was a clearly delineated binary sequence visible just above (0.8 mag) the main sequence and there is an absence of white dwarfs above a magnitude of $V=17$. Her study ended at a limiting magnitude of $V=20.5$, a large increase from the previous limit of $V=14$ (Eggen & Sandage, 1964).

It is important to note that many studies of this cluster did not differentiate which stars were members of the cluster and which were field stars located in front of (between us and the cluster) or behind the cluster. M67 has a high galactic latitude, which minimizes the ratio of field stars to cluster stars (Johnson & Sandage, 1955), so the assumption was that the field stars would not contribute significantly. Sanders (1971, 1977) used a mathematical algorithm to determine the membership of M67. He employed the proper motion and relative location of each star in the field of view to determine a probability of membership to the cluster.

Since the 1950s, there have been several advances in the techniques of determining cluster membership. Sander's method is recognized to be limited.

Francic (1989) explains more clearly what the problems are with Sander's method. Sander's method is biased towards the fainter stars, but cluster membership is likely to go down with magnitude. Another limitation to Sander's method is that there is a bias towards stars that exist far from the center. Jones and Walker (1988) outline fixes to the algorithm to adjust for such biases.

Sander's method was further improved by Zhao et al. (1993). However, the observations made by Zhao et al. were not synchronized. This means that stars do not appear on every image, the baseline between photographic plates is not relatively uniform and each pair of photographic plates has a different accuracy than the next. Despite all of the corrections made, there is still a strong correlation for membership among the study of Zhao to Sanders and Girard et al.

Girard et al. (1989) include radial velocities of stars within their membership algorithm. Radial velocities can help to distinguish field stars that have unusually similar properties. At this time, however, the radial velocity measurements are limited to stars brighter than $V=12.8$. For stars without radial velocity data, they use a weighted version of Sander's method to complete a membership probability.

Due to the proximity of the cluster and the high number of binary members that had been found, there was concern that binary motion could be contributing to the dispersion of proper motion velocities. Girard et al. studied this aspect with radial velocity measurements and found that binary motions are negligible, and the the dispersion of proper motion velocities are due to some other source.

2.2 CCD Studies

The CCD for observational astronomy has become the primary tool for astronomical research. The CCD has far greater sensitivity than the best photographic emulsions and higher spatial resolution than photoelectric detectors. However, before measurements with new equipment can have meaning, standards must be made.

For M67, the photometric standard stars were identified by Johnson & Sandage in 1955. A portion ($M_V = 11.5-16.0$) were revisited by Landolt (1992) for calibration with the standard filter set and photoelectric detector. A calibration field for BVRI CCD photometry in M67 was first observed by Montgomery et al. (1993). This field was made from several criteria. First, a star that could be considered standard must be brighter than the 14th magnitude in the V filter. Second, the star must be less than five arcminutes from the center of the cluster. Third, the star must have an uncertainty of less than 15 millimagnitudes in at least four different images. The last criterion is the star must be published in two other sources (typically Sanders 1977 and Girard et al. 1989), and is not a known variable. Montgomery et al. standard fit the Landolt (1992) standards with an RMS error of 15 to 20 millimagnitudes, thus providing a reasonable transformation of data from prior studies. This was the standard used for M67 until Stassun et al. (2002) improved to 10 millimagnitude uncertainty and Sandquist (2003) improved certainty with high-precision photometry in BVI.

Before CCDs, proper motions of stars in M67 were completed by comparing two photographic plates. The best measurements were produced by

using two plates that were separated by a lot of time. These studies were summarized by Jones (1997). He also produced the first proper motion study on M67 using a CCD. Due to the higher sensitivity and large area of measurement, CCDs are ideal for proper motion studies.

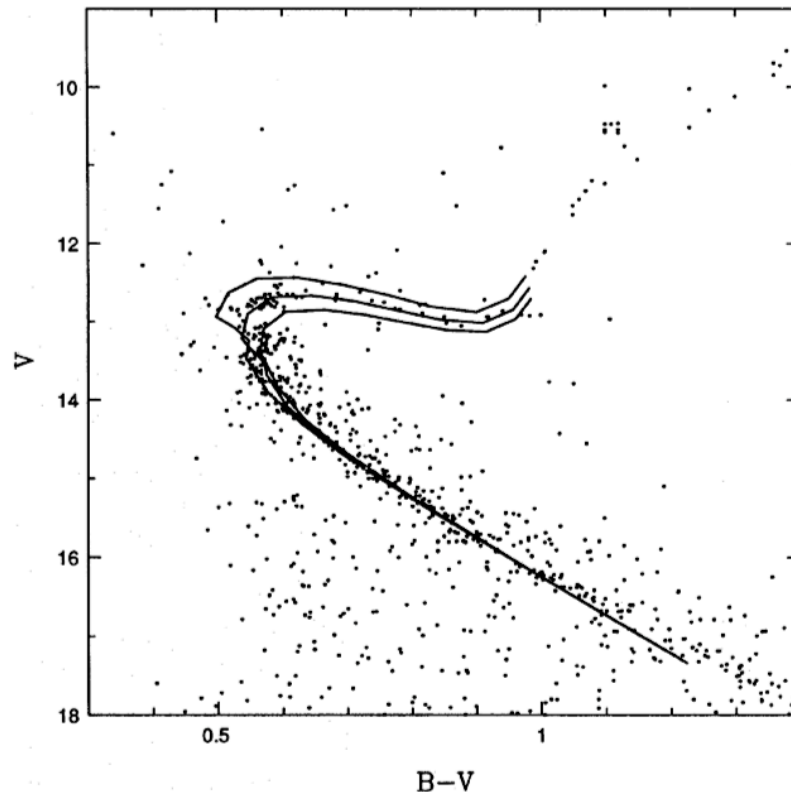


Figure 2.1 A plot from Montgomery et al. (1993). The solid lines are theoretical isochrones fit to the data set, each line representing a different possible age for the cluster.

With the improvement of technology, many groups sought to redefine the characteristics of M67. As a part of the study, Montgomery et al. (1993) use an isochrone to determine certain characteristics. An isochrone is a model of the expected location of stars on a CMD with a large range of mass and a precise, unified, age and composition. By adjusting the models age and composition, the fit should mimic the main sequence, turnoff and red giant branch. An example of

this can be found in Figure 2.1, where Montgomery et al. use theoretical models from Vandenberg (1985) to fit their data. The age they determined had a high uncertainty at 3 to 5 Gyr.

Metallicity is one of multiple variables in an isochrone fit. Because of the isochrone they used (only applicable for metallicities between -1.00 and 0.00), they determined the best match was $[Fe/H] = -0.05 \pm 0.03$. Besides this measurement, nearly all isochrone derived values of metallicity are positive. Vandenberg (2007) present more accurate theoretical models to find a better isochrone. The result is a metallicity value of $[Fe/H] = 0.0165$. This is the same value that Grevesse & Sauval (1998) found for the metallicity of the Sun.

Spectroscopy yields a higher certainty for metallicity. Randich et al. (2006) use 10 stars brighter than $M_V = 14.2$ of different stellar types to estimate the metallicity of M67. They find a value of $[Fe/H] = 0.03 \pm 0.01$. Uncertainties from previous studies are more than three times larger. Taylor (2007) uses several studies to find a weighted average metallicity. The final result is $[Fe/H] = -0.009 \pm 0.009$. However, due to the questionable nature of this average (little information is given as to why parts of each study were left out of the final weighted average) we resort to the Randich et al. value as the most recent and most certain value for metallicity.

The isochrone can also be used to determine the reddening of the system based on the amount of color correction needed for the isochrone to match the observations. Montgomery et al. found the color excess to be $E(B-V) = 0.05 \pm 0.01$. Sandquist (2003) found a different reddening value of $E(B-V) = 0.04 \pm 0.01$ from

an isochrone. An improvement in precision wasn't achieved until Taylor (2007) used a weighted average method to find a value of $E(B-V) = 0.0409 \pm 0.0041$.

Variability in the cluster was explored thoroughly by Stassun et al. (2002) where variability is measured with a precision of better than 20 millimagnitudes. Amplitude of variability detected was limited to about 10 to 100 millimagnitudes with about half of the variables existing in known binary systems. Many of these stars were further studied by Sandquist et al. (2003), Sandquist & Shetrone (2003) and Stello et al. (2007). These studies were on specific variable members with little focus on Sun-like stars.

One study (van den Berg, et al. 2002) links the variability of a system with likelihood of it occurring in a binary system. Since Racine (1971), the binary sequence of M67 has been a popular topic. Montgomery et al. (1993), Girard et al. (1989) and Zhao et al. (1993) all note it near 0.7 magnitudes above the main sequence. Montgomery et al. (1993) note that 38% of cluster members are binaries, and Stassun et al. (2002) note that there is a large amount of binary systems outside the well-defined binary sequence.

Chapter 3. Observations

There are two ways of obtaining data for this project. We can use data from previous studies, or we can take new data. We chose to acquire new data because we can configure the observation method to suit our needs for this project. Previous studies focus on the high-amplitude variability.

3.1 Observatory

3.1.1 Location

We used the Erwin W. Fick Observatory, which is owned and operated by Iowa State University. It is located southwest of Boone, Iowa ($93^{\circ} 56' 38.2''$ west longitude, $42^{\circ} 00' 20.2''$ north latitude, at an altitude of 342 meters). This observatory also has the advantage of availability; there is no competition for observation time.

Though not far from a relatively large city, this location has good seeing with a naked-eye viewing limit on a typical moonless night at a magnitude of about 5.5. The limiting magnitude depends on the light pollution around the location of the observatory. You can see in Figure 3.1 (next page), that there are large sources of light pollution near Fick observatory (Cinzano et al. 2001). The observatory is located at the large cross, while the smaller crosses located just to the east and southeast indicate the location of Ames, Iowa and Des Moines, Iowa, respectively. Cinzano et al. determines the sky brightness for Fick Observatory's location at a magnitude in V of 20.49 to 21.25. Any stars fainter

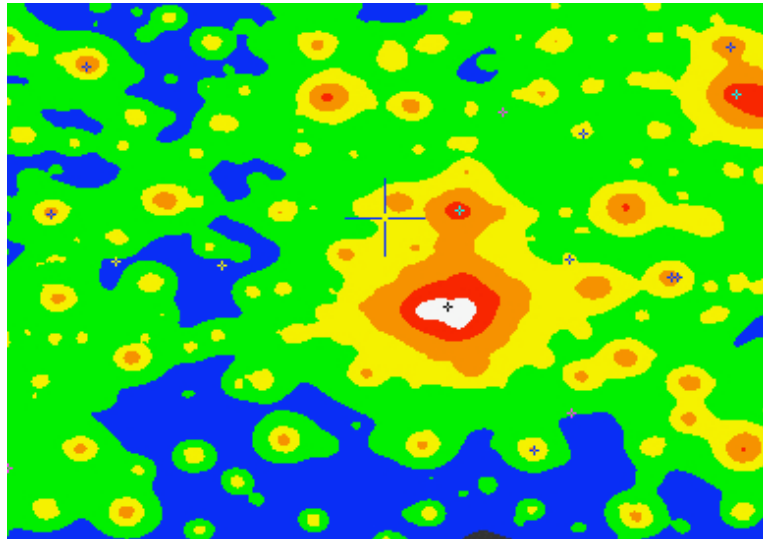


Figure 3.1 Light pollution near Erwin W. Fick Observatory. Credit: P. Cinzano, F. Falchi, and C. D. Elvidge. Copyright Royal Astronomical Society. Reproduced from the Monthly Notices of the RAS by permission of Blackwell Science.

than this range will be dominated by sky brightness. The majority of the light pollution at our location comes from the city of Boone, Iowa (just to the northeast), but there is large contribution by the city of Des Moines.

3.1.2 Light Gathering

We employed the 0.6 meter aperture, computer controlled Mather Telescope for this project. This telescope has a fast focal ratio of $f/4.2$ and it is mounted equatorially. Due to the type of the mount, the telescope is limited to just over 8 hours of right ascension (beginning at about 2 hours east of the meridian). The angular resolution of this telescope is limited to about one arcsecond when using the Marconi CCD47-10 CCD. The camera has a 1024 by 1024 pixel CCD, which covers an area of 13.3 mm by 13.3 mm; the pixel size is 13 microns. The gain for the CCD is about $2.25 \text{ e}^-/\text{ADU}$, and the effective

Johnson/Bessell BV Passbands

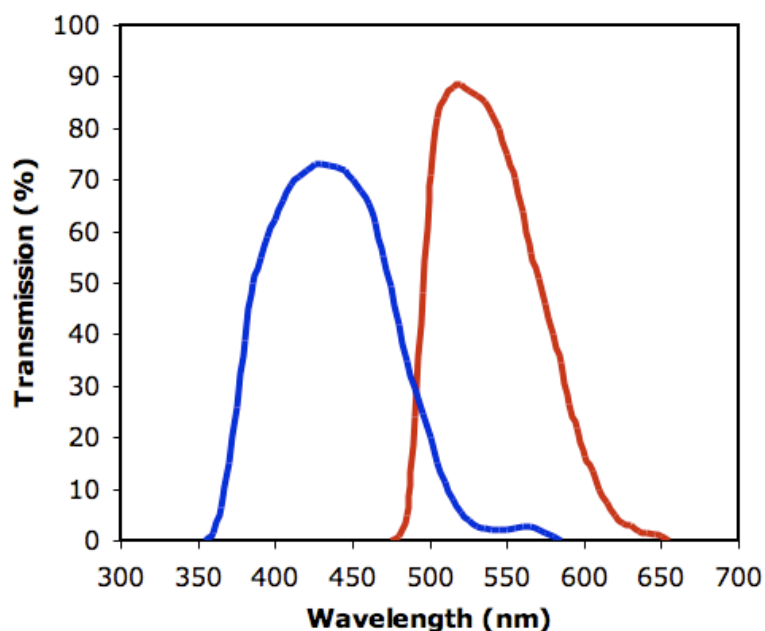


Figure 3.2 Transmission passbands for the B and V filters. B filter is in blue (left) and the V filter is in red (right).

readnoise is about 5.04 electrons per pixel. The CCD covers a spectral range of about 200 to 1100 nm, and with filters, the spectral range of the data will cover a smaller bandwidth.

The filters used with observation are Andover Corporation BVI Johnson/Bessell filters. Unlike the original Johnson-type filters that were designed to work with photoelectric detectors, these filters were designed to account for the sensitivity curve of the CCD as recommended by Bessel (1990). The filters are square so they have little contribution to the vignetting error of the system. According to the spectrophotometric data curve supplied by the manufacturer, the B filter has a center wavelength of 432.6 nm, a peak transmission of 73% with an effective width of 100.9 nm. The V filter has a

higher transmission, at 88% with a center wavelength of 535.1 and an effective width of 96.6 nm. Transmission as a function of wavelength is plotted in Figure 3.2.

3.2 Calibration Data and Standards

The calibration of the instrument is essential in order to achieve the highest quality of images. We discuss the steps used for calibration.

3.2.1 Linearity

CCD cameras respond to light linearly. This means that there is a proportionality between the amount of light enters the detector, the number of photo-electrons produced, and in turn the number of counts, or Analog-to-Digital Units (ADU) that are recorded by the computer. When the pixel full-well capacity is approached, however, CCD sensitivity becomes non-linear. We must complete a linearity test to ensure that our data remain within the linear range.

The test, according to Bryan (2001), involves imaging an illuminated board in pairs of images taken over a range of exposure times. Each pair of images is taken close together in time. There are two parts to a linearity test. In the first part, these exposures are averaged together to minimize the effect of random noise (noise is discussed in detail in Chapter 5). From the result, the mode of each image is plotted against the exposure time. This plot should have a linear trend. Though it is quick to determine a break point from the linear response region, this method is limited. In the second part, we combine the images by

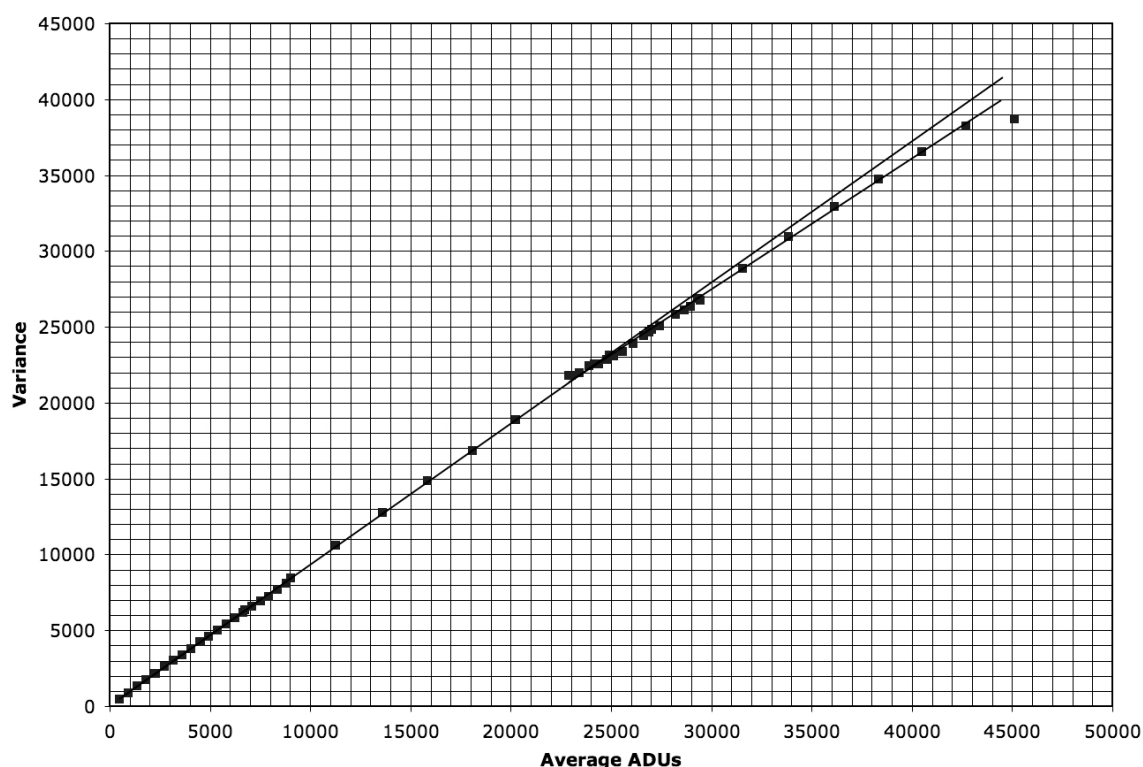


Figure 3.3 Linearity Test – Variance is plotted versus mean count. Note the second linear regime starting near 26000 counts and the extreme turnoff near 42500 counts.

dividing one by its pair (resultant image is called the quotient image). This is done to eliminate most systematic sources of error, such as vignetting. It also provides an image of counts close to unity. After this, the mean of a localized measurement area (in our case, the central 200 by 200 pixels) is extracted from one of each pair of original images. The quotient image is then multiplied by the mean to scale each image back to its original average. Now we determine from this scaled quotient image the mean and the standard deviation, we can use these to make a plot of variance (standard deviation squared) versus mean. As you can see in Figure 3.3, the primary linear regime ends at about 26000 ADU, limiting our useful data to values at or under this mark.

It is interesting to note that we did not expect to have two linear regimes. We completed this test twice, confirming in both cases to have a second linear regime between the values of 26000 and 42500 ADU. Since the second region is smaller and implies a much higher read noise (see section 3.2.6 for determination of the readnoise), we will disregard values that enter that region. We therefore determined any star with a peak above 26000 to be saturated and removed from further analysis.

3.2.2 Shutter Error

While taking calibration data, an observer would notice that the entire field is not illuminated evenly. Mostly, this is caused by vignetting, which we will address later. There is, however, a change in illumination from the shortest exposures to the longest exposures. This is called shutter error. At shorter exposure times, the shutter requires a higher fraction of the total exposure time for opening and closing. For the shutter at Fick, this results in higher illumination near the center of the image relative to the edges. This effect can be seen clearly in the V filter images in Figure 3.4, whose shutter times are 0.1 seconds and 3.2 seconds respectively. We can eliminate this problem by maintaining exposure times above some minimum value. This minimum value will be different based on the filter, since each filter has a different transmission fraction, as well as the precision of the photometry. We start with taking many images across a wide range of exposure times. Each image is normalized. We then divide the longest exposure image by each of the other images. The result is a

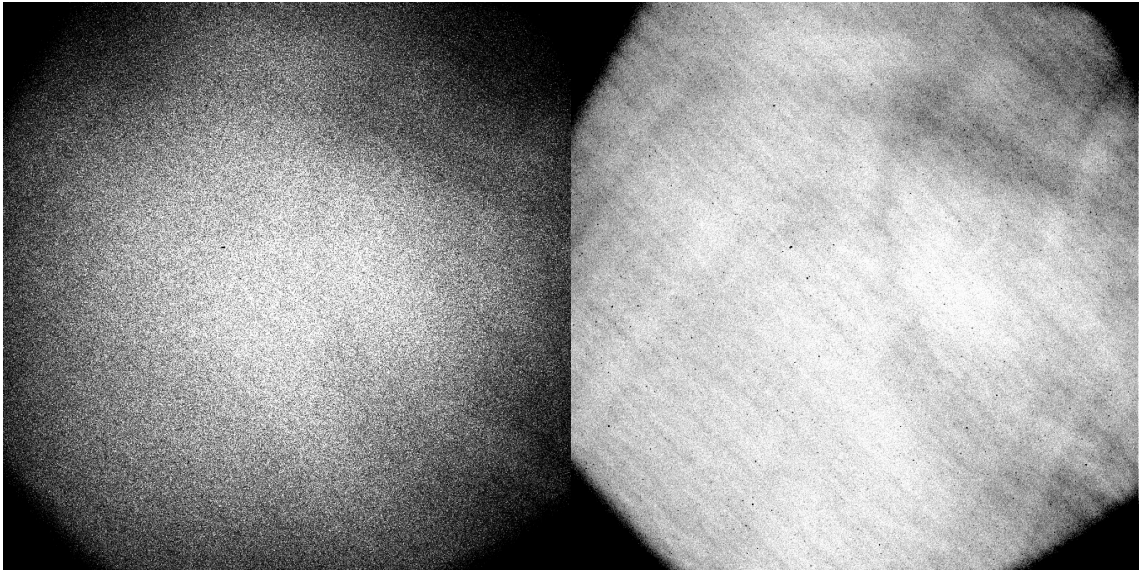


Figure 3.4 Images of a screen taken at different exposure times. Similar vignetting effects can be seen (the darkened corners) in both, but on the left, the central intensity decreases radially due to shutter error.

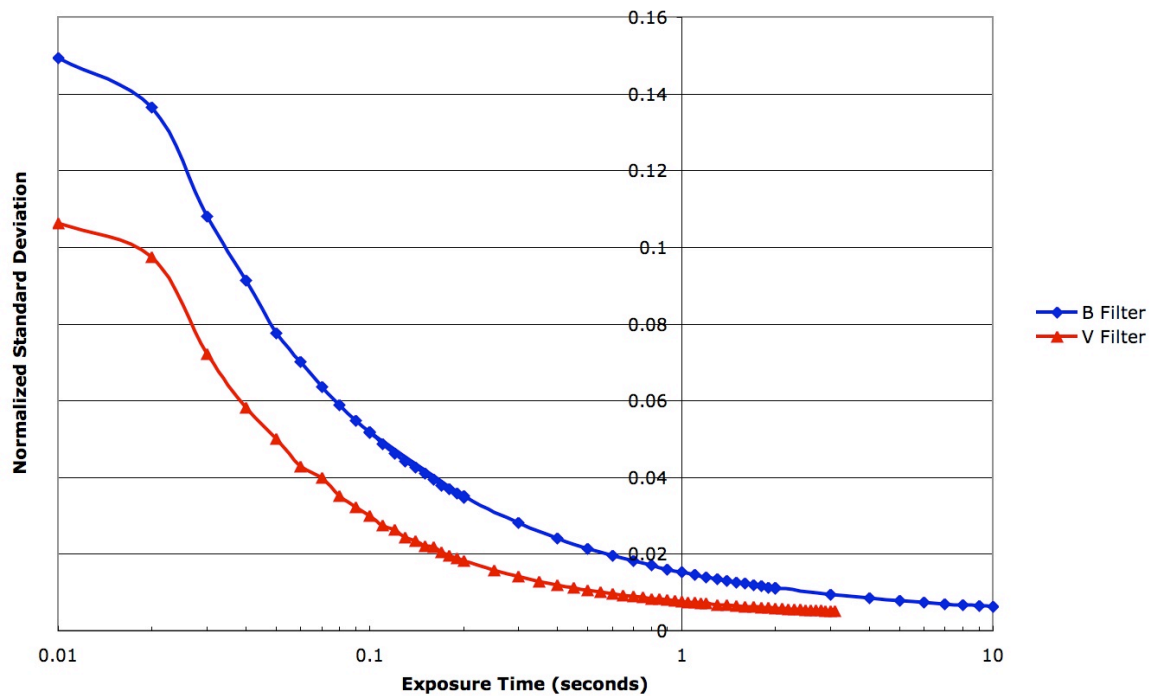


Figure 3.5 Shutter Test – Normalized standard deviation is plotted versus exposure time. Note that the curves are not aligned due to differences in transmission fraction.

comparison of each image to the image of longest exposure time. The standard deviation of this comparison image expresses the fractional deviation; e.g. if a standard deviation of a comparison image is 0.01, it has a 1% deviation. A plot of the standard deviation of the comparison images versus exposure time is presented in Figure 3.5. As the exposure time decreases, the edges of the image deviate more from the center. If the effect were to only be a loss of illumination, the standard deviation would scale with exposure time.

At this point, it is important to note that this effect will not be significant when taking science images. The reason for this is that the field will not be sufficiently bright to need short shutter times. As said before, shutter error occurs when the amount of time devoted to opening and closing the shutter requires a higher fraction of the total time. However, in order to get some calibration flats, fast shutter speeds are unavoidable.

3.2.3 Biases and Flats

The science images will have systematic errors that can be removed with calibration data such as Biases and Flats. Biases will remove the additive systematic noise, and flats will remove the multiplicative systematic noise. These processes are discussed in full detail in Chapter 4.

Sometimes the bias includes a pattern that is present on all images. If removing the additive effects are not enough to resolve this pattern, a master bias should be produced. This 'persistent' pattern will be removed in a multiplicative process separate from the flats.

3.2.4 Darks

Sometimes, CCD data have to be corrected for dark current. Dark current is caused by the accumulation of charge that is independent of the presence of light and is due to the temperature of the detector. It is approximately linear with time and independent of filter or illumination. The dark current is negligible if the CCD is cooled sufficiently, but we can verify this by taking a set of “dark” images. After shutting the slide that covers the CCD entrance, we take a series of exposures. These need to be long in duration for the temperature at which the Andor CCD is operated. After the series is complete, we correct for the bias, and combine the images to produce a dark image cleaned of cosmic ray hits. We completed this test with the Andor CCD at -80 degrees Celsius, and we found, at the conclusion of this test, the dark current has an average value of 0.232 ± 0.013 ADU per minute per pixel or 0.004 ± 0.002 ADU per second per pixel. We conclude from this result that the affect of the dark current on our short duration science data is negligible.

3.2.5 Determination of Readnoise and Gain

There are multiple ways to determine the values of the gain and the readnoise of a CCD. The first is outlined by James Bryan (2001), where the linearity test will also serve as an explicit test for gain and readnoise. After recognizing the linear regime (see Figure 3.2), we fit fitting a line to it:

$$y = mx + b \quad \text{where} \quad m = \frac{2}{g} \quad \text{and} \quad b = 2R^2$$

where g is the gain in electrons per ADU and R is the readout noise in ADU.

Bryan acknowledges the difficulty of this method to produce an accurate measurement of readout noise by supplying an alternative calculation for it:

$$R = g\sigma$$

where σ is the standard deviation of a single bias image. This method seems to correlate well in comparison the next method.

Another way to determine gain and readnoise is by using the method described in Birney et al. (2006). This method uses two bias images and two flat images:

$$g^2\sigma_{F_1-F_2}^2 = g^2\sigma_{Poiss}^2 + g^2\sigma_{B_1-B_2}^2 \quad \text{where} \quad g^2\sigma_{Poiss}^2 = g[(\overline{F_1} + \overline{F_2}) - (\overline{B_1} + \overline{B_2})]$$

where $\sigma_{F_1-F_2}$ is the difference between the standard deviations of the flat images,

$\sigma_{B_1-B_2}$ is the difference between the standard deviations of the bias images, and

$\overline{F_1}$, $\overline{F_2}$, $\overline{B_1}$, $\overline{B_2}$ are each the mean value of the pixels in their respective image.

From this the gain value is determined and another equation is used to determine readnoise:

$$g^2\sigma_{B_1-B_2}^2 = 2\sigma_R^2$$

where σ_R is the readnoise. The values we found for our data are $g=2.25$

electrons per ADU and $R=\sigma_R=5.04$ electrons per pixel. As a check to see if our

readnoise and gain were correct, we used an *IRAF*-based program called

“Noisemodel” in Figure 3.6. Originally used for the Wide Field Planetary Camera on the Hubble Space Telescope, this program plots the variance versus the bias-subtracted mean counts of the bias and flat images used for the linearity test.

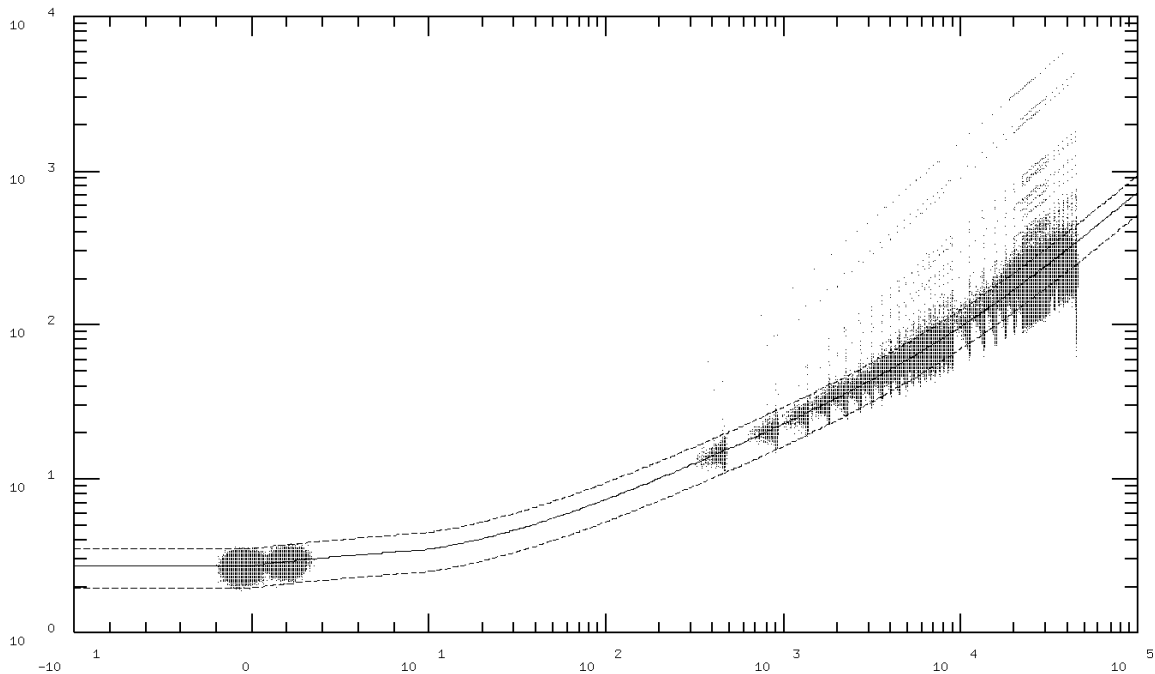


Figure 3.6 Noisemodel Output – Variance is plotted versus mean counts. The solid curve indicates the location of the median and the dotted curves represent the values for ± 2 standard deviations.

From the input values of readnoise, gain and scalenoise, it produces a curve (solid) and error curves (dotted) based on standard deviation. The user can judge whether the data is accurate by visually inspecting the solid line passes through the median of the points for each bias and flat. For our data, the plot confirms that the values above for readnoise and gain are correct.

The scalenoise produces a curve in the fit. Note that the initial bend of the line is because the axis is linear from -10 counts to 10 counts and switches to logarithmic after 10 counts. Scalenoise for our data is 0.7% increase in variance per mean count. This noise is the result of pixel-to-pixel sensitivity variations; it is seen as a nonlinearity in the variance with respect to mean counts, but this noise is systematic. It is removed when images are flat-fielded.

3.3 Program of Observation

Data was acquired by three different people, so the method of observation was standardized. In this section we discuss how that program was carried out. Table 3.1 on the next page gives a summary of the observations.

3.3.1 Positioning the Field

We will be using a photometry code designed to work with an inhomogeneous¹ set of exposures. Because of this, we do not need precise positioning of M67 on the CCD. However, since we are interested in photometry of many cluster members across several nights, it is important to have relatively the same stars visible in the field of view. After the field is positioned, the autoguider is turned on and set to a bright star. The autoguider is necessary because there is a small, but noticeable timing error in the telescope drive. Without it, the full-width at half-maximum (hereafter FWHM) of the star increases and the photometry becomes less precise.

3.3.2 Focusing

Focusing light allows a detector to distinguish more detail, and in most situations is preferred. In our case, however, having sharp focus could cause saturation of the brightest stars for the exposure times we use. By not focusing the image finely, we allow the light to be spread over a greater area of the detector, thus preventing saturation. As long as this entire area is included in

¹ Each image has a different photometric zero-point, uncertainty and central coordinates. More importantly, not all stars may be present on all frames. See further explanation in Honeycutt, 1992.

Table 3.1 Observations

Date	Images/Filter		Flats/Filter		Weather	Lunar Phase –		Mean	Obs.
	B	V	Dome	Sky		% Illumination	FWHM		
13-Mar	5	5	-	-	P. Cloudy	*Crescent – 38%	5.59 [†]	Tobin	
16-Mar	5	5	-	-	Clear	*Crescent – 13%	3.68	Gonz.	
18-Mar	5	5	-	-	Cirrus	*New – 2%	4.62 [†]	Gonz.	
20-Mar	6	6	4	-	Clear	*New – 2%	4.13	Eitter	
26-Mar	7	7	7	-	Clear	First Quarter – 53%	4.65	Tobin	
2-Apr	9	9	9	9	Clear	Full – 100%	3.58 [†]	Tobin	
5-Apr	8	9	-	-	P. Cloudy	Full – 94%	3.41	Eitter	
6-Apr	7	7	4	-	P. Cloudy	*Full – 89%	3.23	Eitter	
7-Apr	10	10	20	-	Cirrus	*Gibbous – 82%	4.37	Tobin	
8-Apr	10	10	20	10	Clear	*Gibbous – 75%	2.93	Tobin	
9-Apr	10	10	20	8	Clear	*Gibbous – 67%	3.48	Tobin	
13-Apr	6	6	4	-	Clear	*Crescent – 25%	3.88	Eitter	
16-Apr	9	9	20	-	Cirrus	*New – 3%	4.21	Tobin	
17-Apr	5	6	4	-	Clear	*New – 0%	4.09	Eitter	
19-Apr	6	6	4	-	Clear	*Crescent – 4%	3.92	Eitter	
21-Apr	9	9	20	-	Cirrus	Crescent – 18%	3.62	Tobin	
22-Apr	9	9	20	-	Cirrus	Crescent – 27%	4.83	Tobin	
29-Apr	9	9	20	8	Cirrus	Full – 91%	4.23	Tobin	
12-May	6	6	4	-	Clear	*Crescent – 29%	4.80	Eitter	
17-May	6	6	4	-	Clear	*New – 0%	4.86	Eitter	
18-May	7	6	4	-	Clear	*New – 3%	4.41	Eitter	

* The moon was not above the horizon for the duration of observations.

[†] FWHM may not be a good indicator of the seeing conditions on these nights because the autoguider failed during part of the observations.

our photometric measurements, the effects of poor focus will be insignificant for the stars we in which we are interested, and a coarse focus is adequate.

3.3.3 Exposure Times

Because we are observing Sun-like stars, we need exposures that will give accurate photometry near 14.6 in V, and likewise near 15.3 in B. For calibration and color corrections to standard stars, we need a few magnitudes brighter than this, or about magnitude 12 in V. In order to achieve this, we need sufficiently long exposures, but we also need short enough exposures so that brighter stars do not saturate. Empirically, we find that for the V filter, exposures of about 60 seconds are good for viewing stars between 11.5 and 15.5 magnitudes. Likewise, exposures of about 120 seconds are appropriate for viewing stars between 12 and 16 in the B filter.

3.3.4 Cadence

The cadence of the individual observations is greatly dependent on the CCD readout time. Readout time has three settings: 32 seconds, 16 seconds and 1 second. This corresponds to 34 seconds, 18 seconds, or 2 second of additional time for each exposure. The advantage of longer readout times is that they result in smaller readnoise. If the long readout setting is used, then the time required between exposures is comparable to the exposure time, lengthening the time on M67 on a given night. We want to avoid this due to the changes in extinction across a series of exposures, which is discussed in Chapter 5. Too short and the readout noise is greater, resulting in less precise photometry for the fainter stars. Ultimately the middle readout time allows for observing over a small range in air mass, while retaining an acceptable readnoise level. Total time

between the start of one exposure to the next is 78 seconds and 138 seconds for V filter and B filter images, respectively.

We obtain multiple images on each night so that we properly characterize photometric uncertainties. In particular, multiple closely timed images permit us a separate noise contributions from atmospheric scintillation and Poisson statistics.

The exposures for each filter are taken in series. Between each series of science images, a series of bias images are taken, the filter is changed, the focus is adjusted and sometimes the telescope is repositioned (because focusing may cause the autoguider to lose the star), all of which will effect the night-to-night cadence. Generally, the B filter images were taken first, followed by a set of biases and then the V filter images.

Ultimately, the more images we can take the higher the precision we can achieve. We take a minimum of 5 images per filter each clear night, and a few extra images (not more than 10) on nights with high cirrus or occasional clouds. Too many images will result in the second series of images occurring at a larger range of air mass and higher extinction amounts. In light of this, we limit the series to a maximum of 10 images.

3.3.5 Biases

A bias image is created by taking an image of zero duration without exposing the CCD to light. This will yield an image with pixel values that contain random noise and a bias offset value. The bias offset value is added systematically to each pixel during the readout process so that the readout noise

is properly sampled. A series of bias images (about 3 to 5) are taken at the start of the night, and then again between each series of flats or science images. The series is taken over a short period of time.

3.3.6 Flats

An important step in taking data is to correct for non-uniform illumination and pixel sensitivity variations across the CCD chip. This can be done with flat field images. There are two main types of flat field images that we employed:

3.3.6.1 Dome Flats

We obtained images of an illuminated screen, located about a meter in front of the telescope. Because the screen is so close, any marks or scratches on it will be well out of focus. Dome flats are used to correct pixel-to-pixel sensitivity variations, which is a type of systematic noise. Images can be taken at any dark time, regardless of the weather. Because of this, many dome flats can be taken and combined to produce a high signal-to-noise (hereafter S/N) ratio.

3.3.6.2 Twilight Sky Flats

Large-scale systematic variations, which may escape correction in a dome flat, can be corrected with a twilight sky flat. A twilight sky flat is produced by taking images of a region of sky, either just after sunset or just before sunrise. In order to obtain very flat illumination, the telescope should be pointed towards a point on the sky with the smallest angular brightness gradient. This point for both

B and V bands is located about 100 degrees from the Sun, opposite the zenith (Chromey and Hasselbacher, 1996) when the Sun is just below the horizon.

Twilight flats are taken in a series of about 4 or 5 at a time. The telescope is moved between exposures. We do this to limit the effect of bright stars in the field. Moving the telescope will change the location of the stars in the image. When combined, we use the median statistic to combine the flats, which is a good discriminator against outlier data values. Since the image of a given star falls on different pixels in each image, the effect of the star becomes insignificant.

3.3.7 Organization and Application

To produce higher quality flat images, we combine flats from several different nights. However, if the flats over the entire two months are combined,

Table 3.2 Master Flat Combinations

Group Number	Range of Dates (2007)	Twilight Flats per Filter	Dome Flats per Filter
1	March 13 th to March 26 th	9 [†]	11
2	April 2 nd to April 6 th	9	13
3	April 7 th to April 9 th	18	60
4	April 13 th to April 19 th	8 [†]	32
5	April 21 st to April 29 th	8	60
6	May 12 th to May 18 th	8 [†]	12

[†] The flats listed in this range of dates are replacement flats.

there may be errors due to the changing conditions (changing temperatures, twilight gradients, dust levels, etc.) Because of this, we separated our flats into groups by ranges of dates. Any flats taken within a range are combined to form

a master dome flat and a master twilight flat for the group. Table 3.2 summarizes which dates were combined to form a master twilight or master dome flat. In some cases, the original set of twilight flats did not meet specific criteria and were removed from further analysis (for information on these criteria, see Section 4.1.2 and 4.1.3). In the case that there were no remaining twilight flats for a particular group, the twilight flats from the nearest available night were used in place of the missing flats.

Chapter 4. Analysis

In this chapter, we will discuss the process by which the data is handled. First we correct the observations for systematic errors. Then we use specialized programs and methods to minimize the uncertainties and transform the data to match professional standards.

4.1 Data reduction in *IRAF*

We reduced our data in the standard way using *IRAF*. All data for the first five groups were reduced together. The data for the sixth group were added later and used the same reduction method, only at a different time. The reduction procedure is as follows.

4.1.1 Bias Subtraction

Each bias image within a series¹ of biases is combined to form a ‘series bias’. The series biases are then combined to form a master bias. This image is checked for a recognizable pattern, to ensure that there is no multiplicative noise present in the biases. Our CCD does not display a pattern, so we did not need to subtract a master bias. In our case, then, we need only subtract the mode of each series bias from each flat and science image, but only the series bias that is nearest each series of images is used. We use the mode value because it is a better discriminator against outlier data values than a simple average. We use

¹ The use of this term is explained as part of the cadence of observations in Section 3.3.4, and again for bias images in Section 3.3.5.

this method to account for the possibility of bias drift. Bias drift is a naturally changing bias level over a night due to changes in conditions of the CCD electronics.

4.1.2 Low Count Flats

Our twilight flats were taken in a series of four or five images. Several series of images were completed. The exposure times were adjusted between each series. At the end of each series, some twilight flats had a peak count lower than 20k. Peak counts this low introduce a higher amount of noise than desired, so any such flats are removed. After all these flats are removed, the final count of usable twilight flats is available in Table 3.1. This minimum for peak counts is the first criterion for removal of twilight flats.

4.1.3 Accounting for Shutter Error

Shutter error is a significant problem when taking twilight flats because the naturally bright illumination requires short exposures. In the twilight, just after sunset, the sky will dim dramatically with time. In order to get enough twilight flats, the observer begins taking exposures soon after sunset. It is possible that the first few images are short exposures, which leads to a higher shutter error in these images. In order to ensure that any shutter error introduced to the data is kept to a minimum, we will remove from our data any images that have exposure times shorter than a minimum exposure time. The minimum exposure time is based on the trend in figure 3.4. For the B filter, our minimum exposure time is 0.1 seconds. This is to keep the deviation under 5 % per B filter twilight flat. For the V filter, our minimum exposure time is set at 0.55 seconds.

Although different exposure times are expected because of differing transmission levels, the minimum exposure time for V is set to a longer exposure time than B. This is counterintuitive since the same precision in Figure 3.4 is achieved at shorter exposure times in V than in B. Since there were many V flats that satisfied the criterion listed in Section 4.1.2, we were able to be more choosy about which flats to ultimately use. We therefore set this value at a longer duration and thus achieving a higher precision.

After flats with short exposure times and low counts are removed, some groups did not have master twilight flats. In this case we use the twilight flats from a night that is closest in time to the range of dates. Specifically, we used the twilight flats from the night of April 2nd for the first group, the night of April 9th for the fourth group, and the night of April 29th for the 6th group.

4.1.4 Flat Division

Multiplicative, systematic noise, including vignetting and pixel sensitivity variations, are corrected with the use of flats. We combine the best aspects of the two types of flats to produce a flat that is better than either one. First, all flats are scaled to a mode value of 45k. We divide each master twilight flat by the master dome flat for a given range of dates. Since the twilight sky illumination is more uniform than an illuminated screen, the resulting quotient image characterizes the deviation of the dome flat from uniformity. A surface was fit to the image using 3rd order Legendre polynomials, which was smoothed by dividing up the image into 30 pixel by 30 pixel boxes and calculating the median. Therefore, this surface fit retains only the large-scale variations across

the image. This surface fit is then multiplied by the master dome flat. This corrects the master dome flat for large scale illumination variations. After normalization, this image becomes the master flat for the group. This process is repeated for each group, resulting in a total of six master flats per filter. Each science image is divided by the master flat for its date and filter.

4.1.5 Standardization

Observations were completed by three individuals, each with his own file-naming conventions. During the application of biases and flats, the files were renamed. The adopted naming convention is related to the organization of data. Filenames are a two letters followed by three numbers. The first letter is a designation for the type of image: 'b' for bias, 'o' for objective, 'f' for flat. The second letter describes the filter (for biases there is only one letter). The next three numbers are flat number, night and image.

4.2 Determining Magnitudes

4.2.1 Selecting Reference Images

For the programs that we intend to use, a single image should be selected as a reference image. We use one of the images in each filter as a reference image for the data of each filter. We choose the reference images by determining the most centralized image. We also consider the mean FWHM of the stars on the image to ensure that our reference image is of good quality. We select these reference images prior to running any programs. Though most of

the images during the twenty-one nights of data were taken in relatively good seeing conditions; most images were offset from the median central coordinates by about 100 pixels. The reference images chosen ('ob233.fit' for the B filter and 'ov214.fit' for the V filter) were offset from the median coordinates by less than 40 pixels.

4.2.2 *SExtractor* and *Astrometrica*

The next step is to extract the stellar information and find an astrometric solution. Each of these processes can be done independently with two different programs.

4.2.2.1 *SExtractor*

To extract stellar information, we use a program called *SExtractor*. This program finds stars and reports stellar Cartesian coordinates. The program also extracts basic aperture photometry based on input parameters including the gain, detection thresholds and FWHM. Though photometry is a part of the output, *SExtractor* does not produce high precision magnitude estimates. Because of this, our only purpose in using *SExtractor* is to locate stars and return their positions in Cartesian coordinates.

We use this program to extract sources based on two key points. First, this program uses a deblending algorithm that will efficiently and quickly identify and separate blended sources from each other. Though this algorithm was designed for the detection of background galaxies, the settings are easily modified to detect and deblend close stars. The second key point is the sources detected in a field can be limited only to those that do not reach a saturation level

set by the user. This is important because our break from linearity occurs much lower than the saturation level and this setting allows us to identify only those stars that are within the linear regime.

SExtractor detected 1163 stars in the B reference image. Because of the extraction settings, the information of only 856 stars were written to an output file. For the V filter, *SExtractor* detected 927 stars and only 691 stars were extracted. We can see here that the program was able to extract more stars for the B filter than for the V filter. This is due to the greater S/N ratio of the B filter.

4.2.2.2 *Astrometrica 2000.0*

To astrometrically fit the reference images, we used a program called *Astrometrica 2000.0*. This program requires the user to input the image as well as the physical properties of the optical device to create an astrometric solution to the reference image. The astrometric solution is determined from a stellar catalog that can be chosen by the user. For our research, we used the USNO CCD Astrometry Catalog 2 (hereafter UCAC2) (Zacharias et al. 2004) astrometric database, which has a reported precision of better than 70 milliarcseconds and proper motion errors of less than 7 milliarcseconds per year. Since the output of *Astrometrica* uses the standard epoch of the selected catalog, and UCAC2 standards are epoch 2000, the output equatorial coordinates are in epoch 2000. The program also outputs the standard photometry that is contained in the UCAC2 catalog. The photometry is useful as a cross-check for matching lists.

Though *Astrometrica*'s fit is applied to each detected star, we only retain the information for the "reference stars" that were matched to the UCAC2

catalog. This is for two reasons. First, the fit includes a value of the deviation from the catalog for the reference stars only. In order to understand the error of the astrometric fit, we need this value. Secondly, the photometry output data for any stars that are not matched directly to the catalog are not a part of the standard magnitudes and may have errors.

For the B filter, *Astrometrica* found 220 reference stars with an average deviation of less about .04 arcseconds. For the V filter, *Astrometrica* found 245 reference stars with an average deviation of less than 0.05 arcseconds.

Astrometrica also returns the equatorial coordinates for the center of the plate.

4.2.2.3 Matching Lists

The independent lists from *Astrometrica* and *SExtractor* are then combined, matching extracted stars from *SExtractor* and the reference stars from *Astrometrica* by comparing their Cartesian coordinates. The Cartesian coordinates are measurements of the distance of a star in units of pixels from the coordinate zero points. *SExtractor* and *Astrometrica* have different zero points. The horizontal coordinates of each match, but the vertical coordinates are inverted. This was fixed by changing the *Astrometrica* zero-point on the vertical axis from the top of the image to the bottom of the image.

4.2.3 Least-Squares Fit

Most of the stars extracted by *SExtractor* do not have a corresponding reference star from *Astrometrica*. We would like to keep the list produced by *SExtractor* because of its deblending algorithm, so this means every star on this list must be fit with equatorial coordinates.

After organizing the list of matched reference stars, the list was refined to the reference stars whose root-mean-square fit is better than 0.01 arcseconds and the estimated S/N ratio was above 100. There were 21 stars that match these criteria. It is important that these stars are spread out across the image. This is to ensure the astrometric solution will fit all stars within the image. In order to find the equatorial coordinates for all of the stars, we will use a modified version of the method described by Birney et al. (2006). The method first requires calculating plate constants:

$$\xi = \frac{\cot \delta \sin(\alpha - A)}{\sin D + \cos D \cot \delta \cos(\alpha - A)} \quad \eta = \frac{\cos D - \cot \delta \sin D \cos(\alpha - A)}{\sin D + \cos D \cot \delta \cos(\alpha - A)}$$

where A and D are the equatorial coordinates of the center of the image and α and δ are the equatorial coordinates of a star. The plate constant for each star is the linear distance along the focal plane that you would find a star, and it is derived from a spherical coordinate system. Since each star has specific Cartesian coordinates, the matching procedure is just solving a set of quadratic equations:

$$\xi - x = ax^2 + by^2 + cxy + ex + fy + g \quad \eta - y = hx^2 + iy^2 + jxy + kx + ly + m$$

where a, b, c ... m are all constants true for every star and x and y are the coordinates of each star. This is the part that is slightly modified from Birney et al. (2006), since we are using a quadratic fit process instead of the standard linear method. Although astrometric solutions were obtained with the standard linear method, quadratic and cubic methods simultaneously, we used the

quadratic method because we found that the solution fit the known coordinates of the UCAC2 reference stars with less error.

We use *Mathematica*'s built-in `Fit[]` procedure to solve for the coordinates. *Mathematica*'s natural precision limit is on the order of 10 decimal places. For this solution, we need at least 15 decimal places. This value was not chosen at random, it is the limit of precision of modern computer programming, e.g. the maximum number of places after the decimal that a standard C or C++ variable can retain. Please see Appendix A for details on the *Mathematica* code and the constants derived from it. The astrometric solution had an uncertainty of less than 0.25 arcseconds to the reference stars of the UCAC2 catalog. The detected stars are visible as red circles in the overlay in Figure 4.1.

4.2.4 Balaguer-Núñez matching

For comparison to previous research, we need to match our stars to a published catalog of M67. We chose to use the catalog from Balaguer-Núñez et al. (2007) because it identified more stars (1843) in the direction of M67 than any other, and it includes membership information. A large catalog ensures that the majority of our stars can be quickly cross-referenced to other studies. The Balaguer-Núñez catalog is also cross-referenced to the Sanders (1977) catalog, which is the most widely cited reference for identification of stars in M67.

Each star's equatorial coordinates are then match to the Balaguer-Núñez equatorial coordinates. As a check, the magnitudes listed in the catalog can be compared to the magnitudes in the outputs of *SExtractor* and *Astrometrica*.

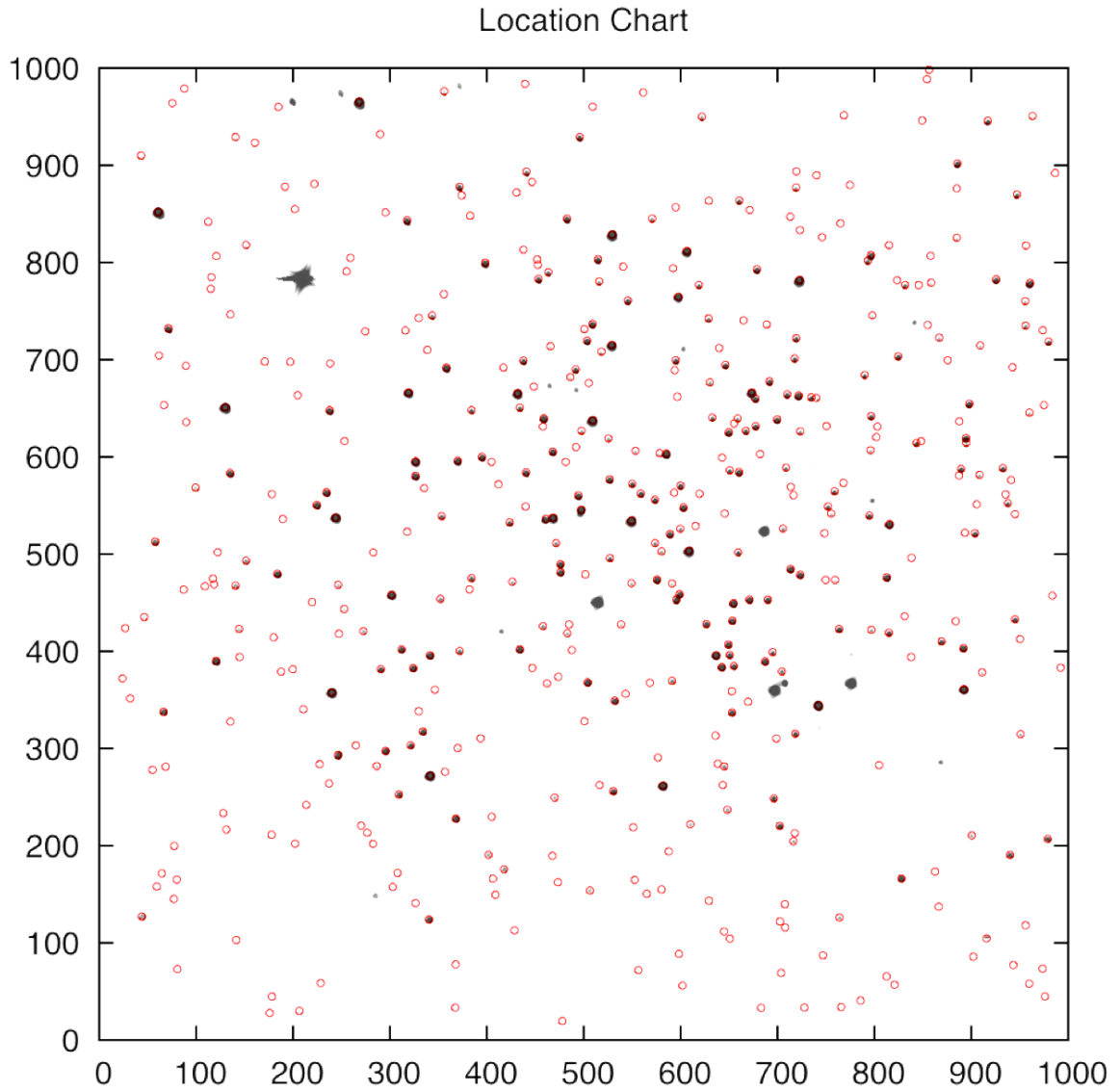


Figure 4.1 Image in B of the field of M67 with an overlay of the detected star locations in red circles. The axes are in units of pixels. Note that there are no circles around the brightest stars.

We also consider any match of stars with equatorial coordinates that deviate by greater than a radial distance of 5 arcseconds to be unmatched. The result is 542 matches, and the index number used by Balaguer-Núñez is applied to each of these stars. Some stars did not match the Balaguer-Núñez identification. The index for these stars is a count from 2001 to 2317 for B unmatched stars, and V

filter stars were labeled 2318 to 2884 if they didn't match Balaguer-Núñez or the B filter stars.

4.2.5 *Optimal Photometry*

The algorithm we used to extract photometry is called *Optimal Photometry*. There are three main parts to the algorithm.

4.2.5.1 Preliminary Setup

The *Optimal Photometry* program requires several files prior to the start of the first part of the program. The first file is a list of the stars in the reference image and their Cartesian coordinates. If stars have an identification number, it will be used in the output. If this list also contains their equatorial coordinates, those will be preserved throughout the program. The next file that is needed by the program is a list of exposure times and dates for each of the images. Here we inserted the Julian Date as our date so that the program will include it in the output. The last file that is needed by *Optimal Photometry* is a list of stars to define a point-spread function. The five stars were chosen because they are bright, unsaturated, uncrowded and midway out from the center of the image. Specifically, these are stars with a radial location greater than 128 pixels and less than 384 pixels from the center so that they are in sparse regions of the field.

4.2.5.2 *Pix_info*

Now that we have all of the files needed for input, the next step is to run the first program. The first program extracts information from the FITS header of each image file. This program also requires as input the information on the linearity, saturation, gain and readout noise of the CCD. The image is stored

with an improved header in another FITS file. This file has a similar label to the original file with only the first character changed to an 'h'.

4.2.5.3 *Mapccd*

Mapccd is a program that checks the orientation of each image relative to the reference image. As part of the input for this program, an estimate of the average FWHM is needed, as well as a detection threshold level in standard deviations from the mean. This information is used to create file called *offsets.dat* which will be fed into *Opphot*. *Mapccd* also calculates the value of the background sky noise per pixel.

Besides orientation in position and rotation angle, the *offsets.dat* also output useful statistics on the background sky noise, the number of matching stars to the reference image and the mean FWHM of a Gaussian fit to detected stars.

4.2.5.4 *Opphot*

This program reads in the output files from the previous two programs and returns aperture photometry and “optimal” photometry. As a part of the input, the user specifies an overall radius value for aperture photometry; for this research, we used a value of 5 pixels.

This program outputs many different files. There is an aperture catalog file for each image, and optimal catalog file for each image, a sky file for each image, and a file that describes the seeing over all of the images.

4.3 Color Corrections

Our instrumental magnitudes differ from published data in two important ways. Instrumental magnitudes depend on the properties of the telescope, and more importantly, they depend on the atmospheric conditions. They can be transformed to the standard system by linear least-squares fit to standard stars that have high-photometric precision.

4.3.1 Preparation of Data

Our data values are in four sets of catalogs: two sets of “optimal” photometry catalogs and two sets of aperture photometry catalogs, one set of each catalog for each filter. Individually, these catalogs offer no useful information on the color of a star. Color information is found by taking the difference between the photometry of the B filter minus the V filter for each star. In order to determine a color value for each star, the stars in the catalogs for each filter must be matched. The result is a single catalog for each type of photometry. Furthermore, stars that do not have a match in both filters have no useful color information and can not be color-corrected; such stars were removed from further analysis.

The next step is to find suitable standard stars. We used data from a published catalog known to have relatively-high precision (Sandquist 2003). First we matched stars between our data and the Sandquist catalog. Next, we use the instrumental color from our observations and standard color from Sandquist (2003) to form a baseline for a least-squares analysis.

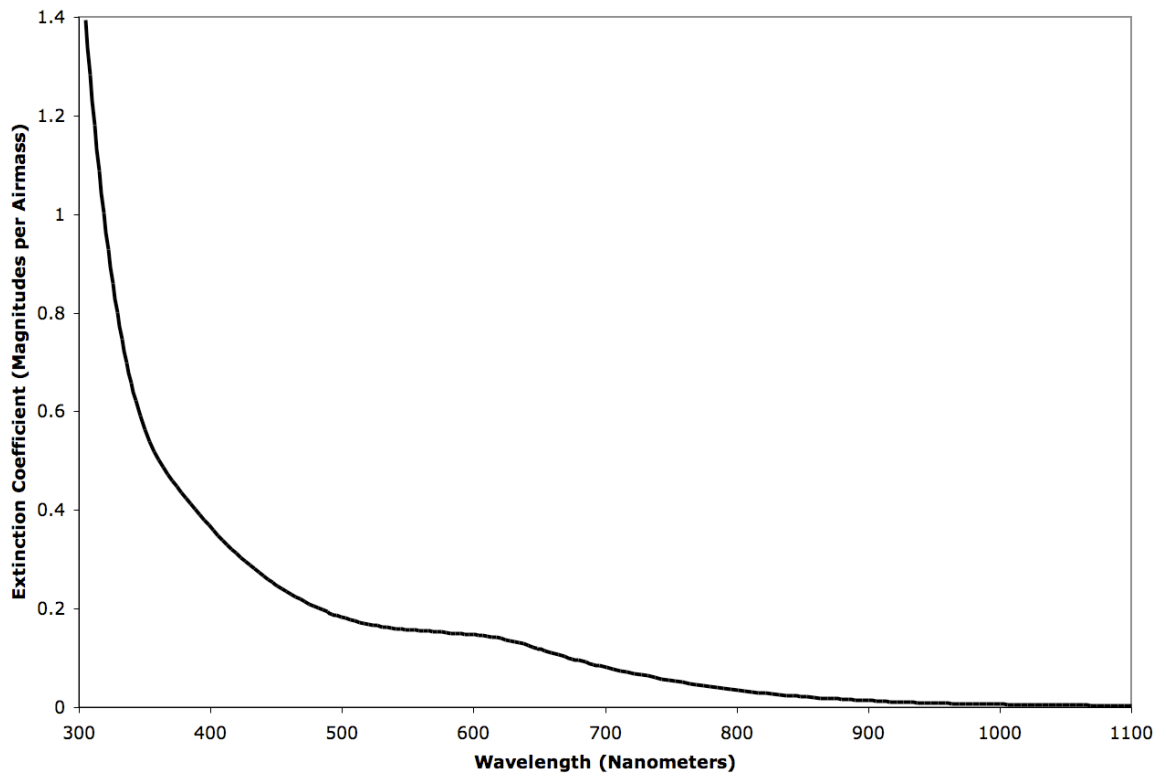


Figure 4.2 Extinction coefficient versus wavelength plot for Landolt standard stars from the Cerro Tololo Interamerican Observatory in Chile. Courtesy of Stritzinger et al., 2005.

4.3.2 Theory of Color-Corrections

The corrections use two basic processes. The first is to remove the atmospheric contribution to the color error. This is the primary reason for color corrections. This contribution, called extinction, depends on color and airmass. Stritzinger et al. (2005) show in Figure 4.2 how the extinction coefficient depends on color. This plot is for the Cerro Tololo Interamerican Observatory, so the vertical scale will be different for our data, but the effect over wavelength will essentially be the same.

A larger airmass will cause the star to become fainter, but this effect is not the same for all stars. Buchheim (2005) presented this effect, where he explained that (due to extinction) blue stars become fainter faster than red stars.

The reason that this occurs is somewhat complicated: Each star has a specific spectral distribution. The transmission of light by the filter varies over a specific spectral range. Refer to Figure 3.2 to see how the transmission varies with wavelength. The combination of these distributions determines the effective wavelength of the observed star. The first-order effect will cause a slight shift in the effective wavelength of the starlight. Since extinction is color-dependent (see Figure 4.2), for blue stars this effect is larger. The combination of a color-dependent effect of extinction and the change in the effective wavelength of a star creates a deviation from the first order correction based on the color of the star. This is evident when looking at two stars of different color and calculating their second-order extinction coefficients. Birney et al. (2006) gives us the standard equation for both orders of corrections:

$$(B - V)_{Corr.} = (B - V)_{Instr.} - k'X - k''X(B - V)_{Instr.}$$

where corrected color is found from the instrumental color, extinction coefficients (k' and k'') and airmass (X). The extinction coefficients are determined from the value of the instrumental color. Examining only the correction of the second order extinction term as it applies to two stars separated only by color:

$$\Delta(B - V)'' = -k''X\Delta(B - V)_{Instr.}$$

Using this equation, we find that we can compare two stars, a blue straggler and a red giant that have a difference in color index of about 0.5 magnitudes. With an intermediate value for airmass, $X \approx 1.4$, and Birney et al. (2006) gives an estimate of $k'' \approx -0.04$. (Buchheim (2005) also presents that this 'textbook' value for the second order extinction is consistent with observations.) The change in

magnitude based only on the second-order extinction and color is 28 millimagnitudes. This means that the color shift of the blue straggler gets redder by 28 millimagnitudes more than the color shift of the red giant. If this were not corrected, we would need to include it as an error, and it would be significant for our data since we expect 'Sun-like' variability on the order of 20 to 30 millimagnitudes.

The second process is to transform stars to a standard color given by a published catalog. Transformation, though unimportant for our goal of differential ensemble photometry, is a necessary and useful result of correcting for extinction. Birney et al. (2006) has an equation for transformation of extinction-corrected magnitudes to standard magnitudes:

$$(B - V)_{Corr.} = \phi + \mu(B - V)_0$$

where ϕ is the offset and μ is the slope of the linear fit; These two values are known as transformation coefficients. Combining equations:

$$\phi + \mu(B - V)_0 = (B - V)_{Corr.} = (B - V)_{Instr.} - k'X - k''X(B - V)_{Instr.}$$

and solving for standard color as a function of instrumental color:

$$(B - V)_0 = A_0 + A_1(B - V)_{Instr.}$$

where

$$A_0 = \frac{-k'X - \phi}{\mu} \quad \text{and} \quad A_1 = \frac{1 - k''X}{\mu}$$

For this research, we will not solve for the individual values of the transformation coefficients or the extinction coefficients. This is because we can make the correction in one step, a linear fit between standard and instrumental

colors. Once A_0 and A_1 are found from the set of standard stars, corrections can be made to the other stars in the set. Since we will be using a form of differential photometry, according to Birney et al. (2006), we can neglect the first order extinction term. We know that $A_1(B-V)_{Instr.}$ is the value that the second order extinction has contributed to the measurements. To remove this value, we only need to subtract the error contribution from the individual measurements:

$$B_0 = B_{Instr.} - A_1(B-V)_{Instr.} \quad \text{and} \quad V_0 = V_{Instr.} - A_1(B-V)_{Instr.}$$

4.3.3 Method of applying corrections

Each image was obtained at a different airmass, so color correction must be independent to each image. A linear fit between the standard colors and the observed colors will contain both a slope and an offset (or intercept) value. Once a slope is determined for the fit, we will use it to correct our instrumental magnitudes.

The data points have two values: $(B-V)_0$ and $(B-V)_{Instr.}$, using a linear least-squares method to fit a line to the data using the formula

$$(B-V)_0 = A_0 + A_1(B-V)_{Instr.}$$

where A_0 and A_1 are the coefficients of the fit. A_1 contains the information necessary to correct for second-order extinction coefficients and transformation to the standard system. A_0 and A_1 can be found by completing the linear least squares fit. The program does this by solving the following equations:

$$A_0 = \frac{\sum (B-V)_{Instr.}^2 \sum (B-V)_{Std} - \sum (B-V)_{Instr.} \sum (B-V)_{std} (B-V)_{Instr.}}{n \sum (B-V)_{Instr.}^2 - \left(\sum (B-V)_{Instr.} \right)^2}$$

$$A_1 = \frac{n \sum (B-V)_{std} (B-V)_{Instr} - \sum (B-V)_{Instr} \sum (B-V)_{std}}{n \sum (B-V)_{Instr}^2 - \left(\sum (B-V)_{Instr} \right)^2}$$

where n is the total number of data points used and the summations are over all stars. Because there are known uncertainties in our data, we can not be certain that a single fit is correct. By removing outliers from the calculations, the accuracy of the fit will increase. Outliers are determined based on their distance from the linear fit in standard deviations. After the first iteration of the program, outliers with uncertainty greater than three standard deviations were removed and the fit was calculated again. On the next iteration, outliers with uncertainty greater than two standard deviations were removed and the fit was calculated again. On this third calculation, the final values for A_0 and A_1 were calculated. The final values for each image are calculated from an average of 65 standard stars, and the fit has a correlation of better than 90%. An abridged copy of the program written to calculate the color-correction constants for each image is available as Appendix B. Figure 4.3 shows the linear fit along with data points after outliers are removed.

To apply the corrections, a new program was written. It was designed to use the same A_1 constant to correct for each night's measurements using these following equations:

$$b_{Std} = b_{Instr} - A_1(B-V) \quad v_{Std} = v_{Instr} - A_1(B-V)$$

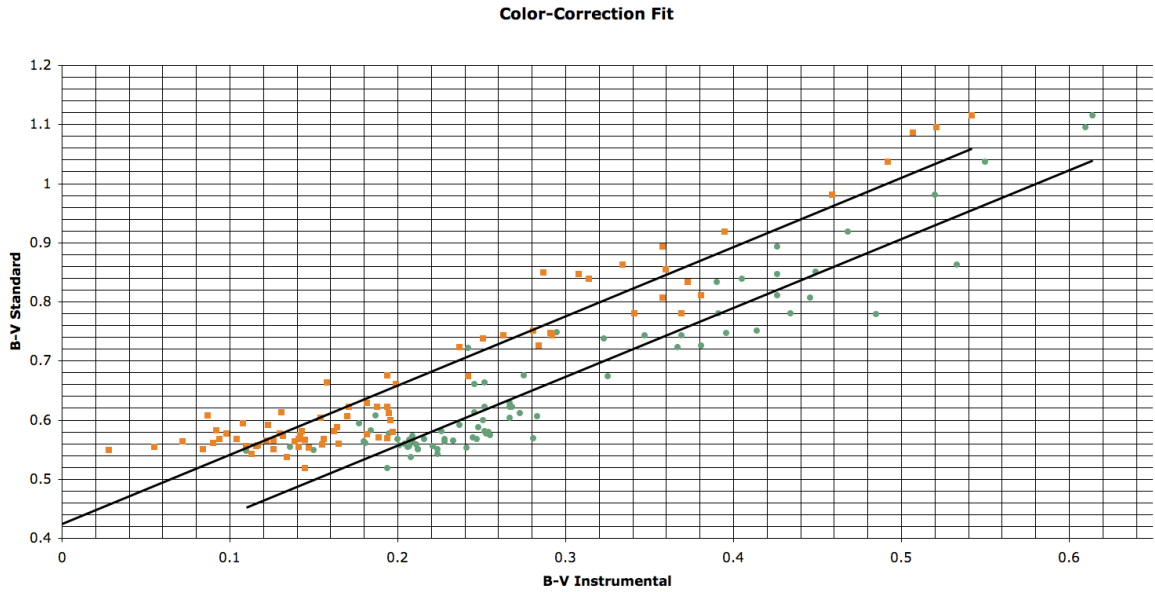


Figure 4.3 Plot showing the instrumental color versus standard color. Orange squares signify the aperture catalog data, and green circles signify the optimal catalog data.

where b_{Instr} and v_{Instr} are the instrumental values from the *Optimal Photometry* output, $(B-V)$ is the instrumental color, and b_{Std} and v_{Std} are the desired result of color-correcting.

It is useful to keep in mind that the resulting standard magnitudes do not include a calibrated zero-point offset. This is not important because we will be looking at differential photometry, where the difference between two magnitudes will result in the cancellation of the offset anyway.

The output catalog from this step contains the new color-corrected magnitudes. It does not change the uncertainties significantly, however, so the uncertainties listed in the catalog are the same uncertainties found in the input from *Optimal Photometry*. The contribution of error from this method should be small since our most significant correction is for second order extinction.

4.4 Improving Precision

Generally, differential magnitudes and their uncertainties are determined on each image independently. The concept behind ensemble photometry is that photometric uncertainties can be improved with a series of images of the same field. Ensemble photometry assumes that a star that is designated as constant will be constant across multiple images. From this, we can use a weighted average of the magnitude of the star to calculate a magnitude with less error. Strict ensemble photometry uses only the constant stars that are found on every image. This method requires a homogeneous set of exposures. The problem is that not all images contain the same stars because of varying aspects of observation, such as cloud cover, atmospheric transparency, airmass, positioning, focus, etc.

4.4.1 Ensemble Routine – Honeycutt 1992

The ensemble routine presented in Honeycutt's 1992 paper describes a method that bypasses this problem. He explains that differential time-series photometry can be obtained from an inhomogeneous set of images, not by comparison to specific stars, but by comparison of image to image. These problems are resolved by accounting for the fact that there will be many "constant" stars available to determine the magnitude zero-offset of each image. By using as many of the constant stars as are available, you can tell how each image changes in uncertainty. Using this image uncertainty, individual stars can then be compared to more well-known constant stars in the image.

The routine uses a weighting system for each star in each image. If the user is concerned that a star might be variable, the user can set the weight of the star to values near zero so that any significance of the variability is eliminated. An advantage of this program is that every star is returned in output even if it was not directly used to estimate the offset of an image.

4.4.2 Ensemble Photometry Program

This routine is available in a program written by Michael Richmond of the Rochester Institute of Technology called *Ensemble Photometry*. The program has two parts, *Multipht* and *Solvepht*. *Multipht* first identifies all stars in every image, matching them (if necessary), and reorganizing the photometry catalogs in a format that is expected by the *Solvepht*. *Solvepht* uses the stars in the input catalog to determine which are variable. Then this program minimizes the contribution of these designated variables by setting their weights to a value near zero. *Solvepht* outputs corrected magnitudes and improved uncertainties for the data. Below, these programs are explained.

4.4.2.1 Multipht

The first program retrieves information from multiple catalogs. The information it requires is Julian date, X and Y coordinates, magnitude and uncertainty to be in columns in separate catalogs, one catalog per image. Each of the catalog names must be on a list. The user inputs the column number for the data and the name of the list.

Other settings can be applied, including the 'isolate' routine, which will discard faint stars near a much brighter source. How near these sources are is

defined by the match radius. For our research the isolate function is used, but our match radius is set to 5 pixels. This means bright and faint sources greater than 5 pixels from each other will be treated as two independent sources.

The output of the program is the entire set of catalogs in one large file. In this file, the uncertainty of each star is been replaced by the weight of the individual measurement. The weight is the inverse of variance:

$$w = \frac{1}{\sigma^2}$$

For the purposes of this project, no matching between frames was required (they were already matched in a previous step), only the reorganization of the photometry catalogs was necessary.

4.4.2.2 *Solvepht*

The next program is called *Solvepht*. The information that the user must provide includes the input file (the output file from *Multipt*), the ‘variability threshold’ parameter, ‘bad image’ numbers, ‘bad star’ numbers and ‘variable star’ numbers. If bad stars are listed, they will be removed from the analysis so that they do not contribute to the overall solution.

The first part of the program uses the input data to determine corrected magnitudes and corrected uncertainties. This part makes two assumptions: (1) most of the stars are constant with well-defined magnitudes and (2) there are no second-order errors (such as scaling or color offsets) in the data. The relationship between the true magnitude and the instrumental magnitude is simple:

$$E_{i,j} = m_{i,j} - [M_i - e_j]$$

where $E_{i,j}$ is the error of each measurement, m_i is the instrumental magnitude, M_i is the true magnitude and e_j is the zero-point magnitude offset of each image.

The subscripts i and j refer to the star and the image, respectively. The intent of the program is to minimize $E_{i,j}$ for all stars by choosing M_i and e_j appropriately.

This is done by setting $E_{i,j}$ to zero and using a least-squares analysis of all data points. The resulting values for image offset and true magnitude are included in the output.

The second part of the program estimates the uncertainty of the true magnitudes by standard practices (Bevington, 1969):

$$\sigma_i^2 = \frac{N \sum w_j (m_j - M_i)^2}{(N-1) \sum w_j}$$

where σ_i is the uncertainty of the true magnitude, N is the total number of images that the star appears, w_j is the weight and m_j is the magnitude of the j^{th} image and M_i is the true magnitude.

The program includes statistics to determine if the data have discrepant values. The uncertainty of the offset for each image is calculated:

$$Z_1 = \frac{\sum z^2 w_{i,j}}{\sum S w_{i,j}} \quad \text{and} \quad Z_2 = \frac{Z_1}{\sqrt{S}}$$

where z is the difference between the corrected magnitude and the instrumental magnitude, w is the weight for each star from the *Multipht* program, and S is the total number of stars within each image. Average uncertainty of each zero-point offset is less than 1 millimagnitude.

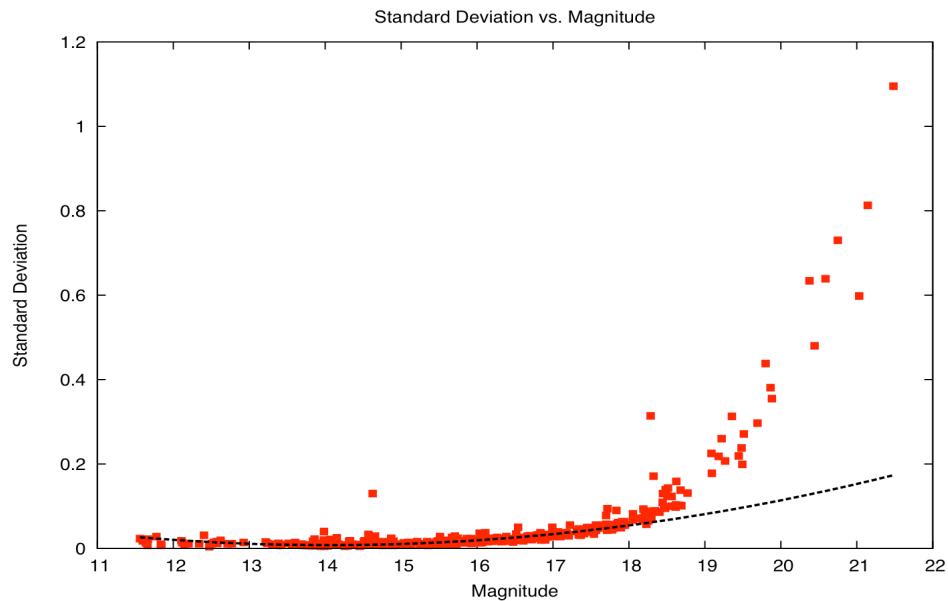


Figure 4.4 Plot of standard deviation versus magnitude with parabolic fit from B filter data. Variable stars will appear at higher standard deviations than the typical star. Note the outlier star at magnitude 14.5 has a well-known photometric variability.

The third part of the program will determine variability. All of the corrected data is divided into bins based on corrected magnitudes; the size of the bins are adjustable by the user. The median value of the uncertainty is calculated for each bin, and a parabolic curve is fit to these values. This can be seen in Figures 4.4 and 4.5. For each bin, the program also determines the average width of the scatter around the parabola. The program then calculates the distance of each star from the parabolic fit in units of the width of the scatter. This value is considered the ‘variability score’ of each star. Any star whose variability score is larger than the variability threshold will be flagged as a variable.

These three parts can be run in an iterative process, so that the program removes the variable stars on the next iteration by setting the weights of the

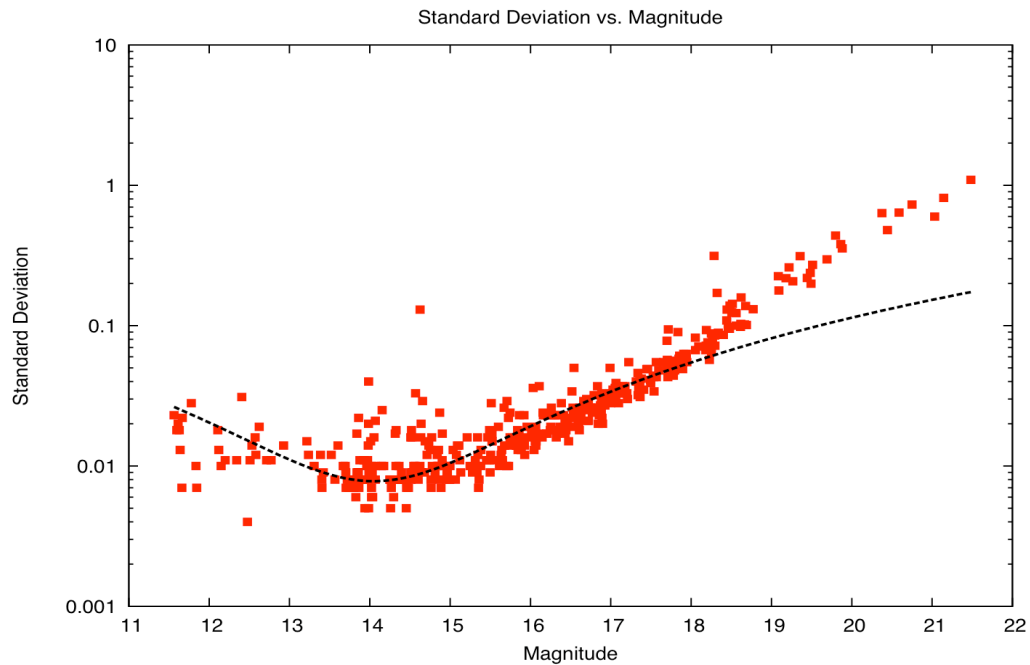


Figure 4.5 Same plot as Figure 4.4, only with a log scale. Here you can see the width of the scatter around the parabolic fit.

flagged variable stars to a value near zero. The program creator recommends at least two iterations, but for our data, we complete three iterations so that it detects variables a total of three times.

Now that variable stars have been designated, we need to determine the uncertainty in their measured magnitude. This is accomplished by using stars that are similar in mean brightness to the variable star. The idea is that the uncertainty of stars of roughly the same magnitude should have the same overall uncertainty. So, the determination of the uncertainty for a variable star is independent of its variability.

4.4.2.3 Fine Adjustments

Using different variability thresholds results in different results; a lower variability threshold will increase the number of designated variables. In Figure

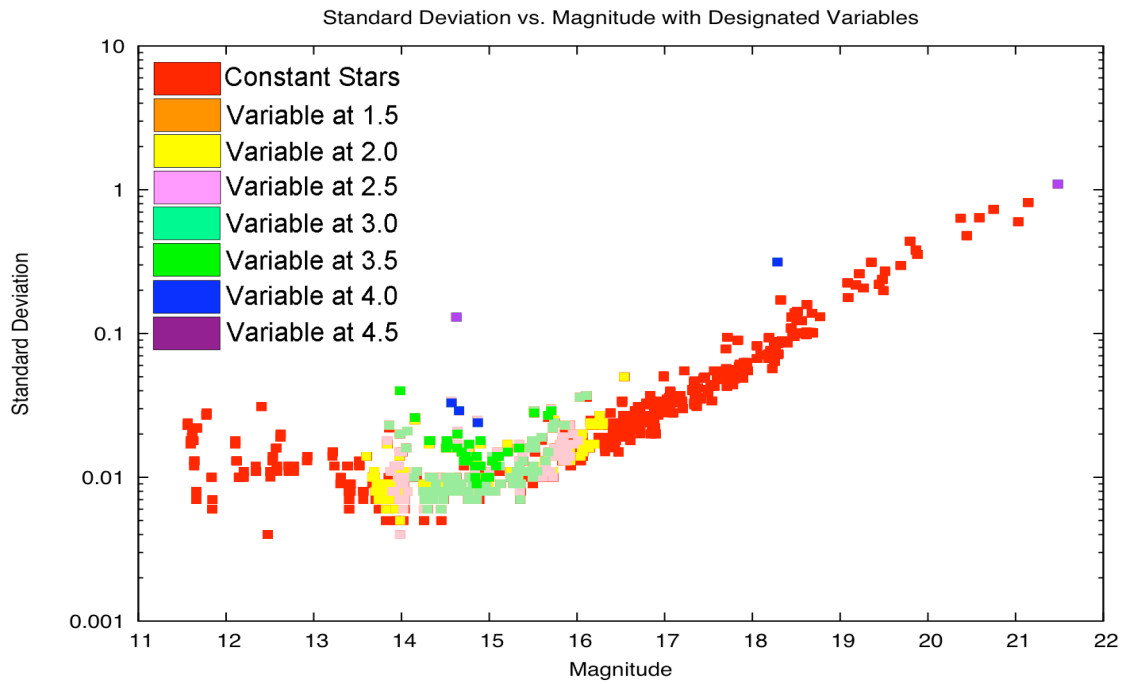


Figure 4.6 Standard deviation versus magnitude plot of the B filter data set. Multiple variability thresholds are shown, with designated variables in separate colors.

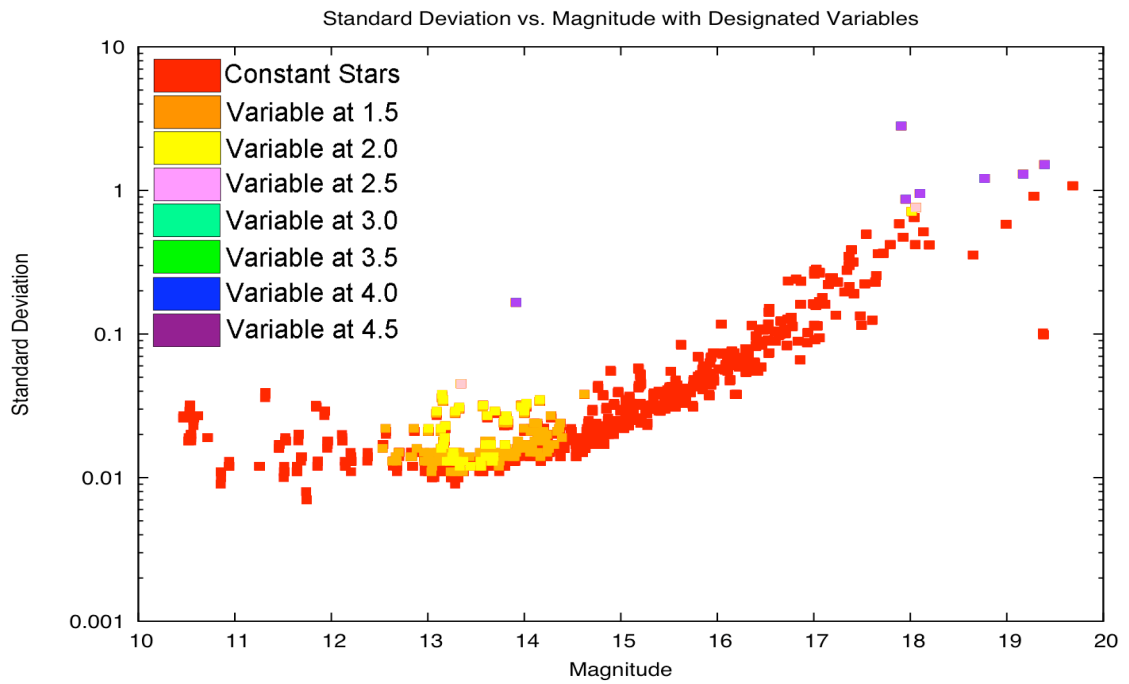


Figure 4.7 Standard deviation versus magnitude plot of the V filter data set. Multiple variability thresholds shown, with designated variables in different colors.

4.6, we use the B filter data to show clearly how changing the variability threshold affects our data. Stars that are considered constant are colored red. The designated variables are shown in orange, yellow, pink, light green, green, blue and purple for variability thresholds of 1.5 to 4.5 in steps of 0.5, respectively. Stars that are designated variables in lower thresholds may be considered constant stars when using higher thresholds, but stars that are designated variables in higher thresholds will still be designated variables in lower thresholds.

Different data sets can have different necessary adjustments. The V filter data, for instance, has a lower S/N ratio due to the shorter integration times. Because of this, the scatter of the data points from any fitted parabola is larger than you would see with the B filter data. This means that the threshold will need to be smaller than the tight-fitting B filter data. As evident in Figure 4.7, different values are needed: for the V filter data, the colors are orange, yellow, pink, light green, green, blue and purple, signifying a variability threshold of 1.5 to 4.5, respectively. Figure 4.9 also shows this problem. For the V filter, it is apparent that a much smaller variability threshold is needed to produce similar results. Further manipulation of this value will give the user the desired number of designated variable stars. Since this uses a variable score to determine the variability of a star, large numbers of variable stars can be sorted by variability score.

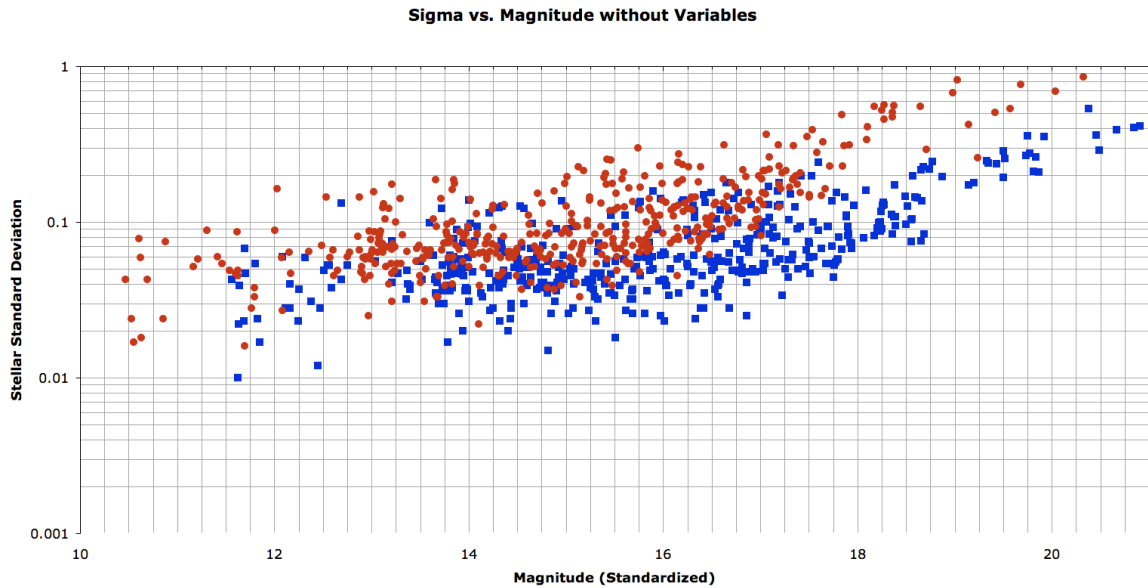


Figure 4.8 Standard deviation versus magnitude (without designated variable stars) diagrams from the optimal catalog output of *Ensemble Photometry*. Blue squares are data points from the B filter and red circles are data points from the V filter. Note the large scatter of the data, such that hardly any trend is noticeable.

4.5 Optimal versus Aperture

Up to now, we have retained both catalogs that were output by *Optimal Photometry* through each step in the analysis. Now, after processing the data through ensemble photometry the first time, the better choice becomes clear. The optimal catalog results in a much larger scatter than the aperture catalog, which is apparent when you compare Figures 4.8 and 4.9. It is important to note that the scales of these figures match. Note, in Figure 4.9, the B filter data has smaller uncertainty at a given magnitude than the V filter data.

Our original purpose of selecting the *Optimal Photometry* code for our project was to minimize the photometric uncertainties. Contrary to our expectations, the standard deviation of the optimal catalog is higher than the

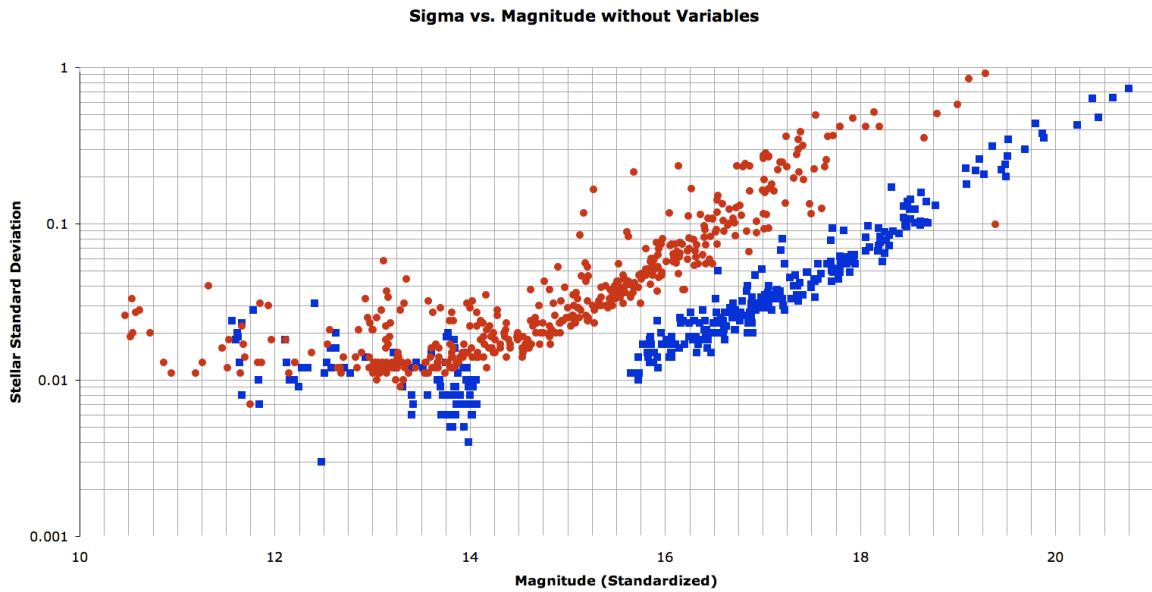


Figure 4.9 Standard deviation versus magnitude (without designated variable stars) diagrams from the aperture catalog output of *Ensemble Photometry*. Blue squares are data points from the B filter and red circles are data points from the V filter. Note the gap in the B filter data between magnitudes 14 and 15.6 is from setting the variability threshold too low, such that all stars near the bottom of the fitted parabola are designated variables.

aperture catalog, especially for the range in which we expect to find Sun-like stars. At this point we choose the aperture data catalog for the remainder of the analysis due to its smaller scatter in its reported magnitudes.

Chapter 5. Discussion of Results

5.1 Results

The following are the results of our observations. We have shown that differential photometric observations can be made at a relatively-high precision using a small research-grade telescope. In the following, we will first ‘place’ the Sun in M67 for comparison. Then we will compare observed features of M67 cluster to published characteristics. Then we will discuss the variables detected by *Ensemble Photometry*.

5.1.1 The Sun in M67

Our primary goal for this project is to measure the photometric variability of Sun-like stars. Sun-like stars in M67 should be located near the part of CMD where you would likely find the Sun if it were located at that distance and reddening. Since it is not possible to transport the Sun to M67, we can at least estimate where the Sun would be. To do this, all we have to know is the intrinsic absolute magnitude in V (M_V), color index (B-V), interstellar reddening of the cluster ($E(B-V)$) and the distance (or distance modulus) to the cluster ($(m-M)_0$). For the last two, we will use the information in Table 1.1. For the first two, we will use values from the textbook by Cox (1999), $B-V=0.65$ and $M_V=4.82$. From Binney & Merrifield (1998), we can use an equation similar to Eq. 3.59:

$$E(B-V) = (m_B - m_V) - (m_B - m_V)_0$$

where $(m_B - m_V)$ is the observed color and $(m_B - m_V)_0$ is the intrinsic color.

Plugging in numbers to this equation, we find that the Sun's observed color would be 0.69. Using the distance modulus estimate of Yadav et al. (2008), we can use the apparent distance modulus equation from Birney et al. (2007) and the typical value for the optical extinction parameter R_V for diffuse interstellar medium from Cox (1999):

$$(m - M)_\lambda = (m - M)_0 + A_\lambda \quad \text{and} \quad R_V \approx 3.1 = \frac{A_V}{E(B - V)}$$

where m is the apparent magnitude, M is the absolute magnitude, and A is the absorption of the interstellar medium at a particular wavelength. The λ means that the $m-M$ value is the apparent distance modulus in a particular wavelength (or filter), where as the 0 means that the $m-M$ value is the true distance without dependency on a particular wavelength. We solve for the apparent magnitude of the Sun if it were in M67, finding $m_V=14.58$.

5.1.2 Color-Magnitude Diagram

One way to examine two-color observations is to make a CMD. For our data, Figures 5.1-5.4 show the features that we expect to find when looking at M67. First the turnoff has a characteristic bend separating the subgiant branch and the main sequence (Figure 5.4). This bend (referred to as the 'overall contraction phase' by Iben, 1967) is due to convection in the core of massive stars ($M > 1.1M_{Sun}$). Convective mixing allows a greater fraction of hydrogen to burn in the core, causing a shift up and to the left on the CMD prior to the ignition of hydrogen shell burning and entry to the subgiant branch.

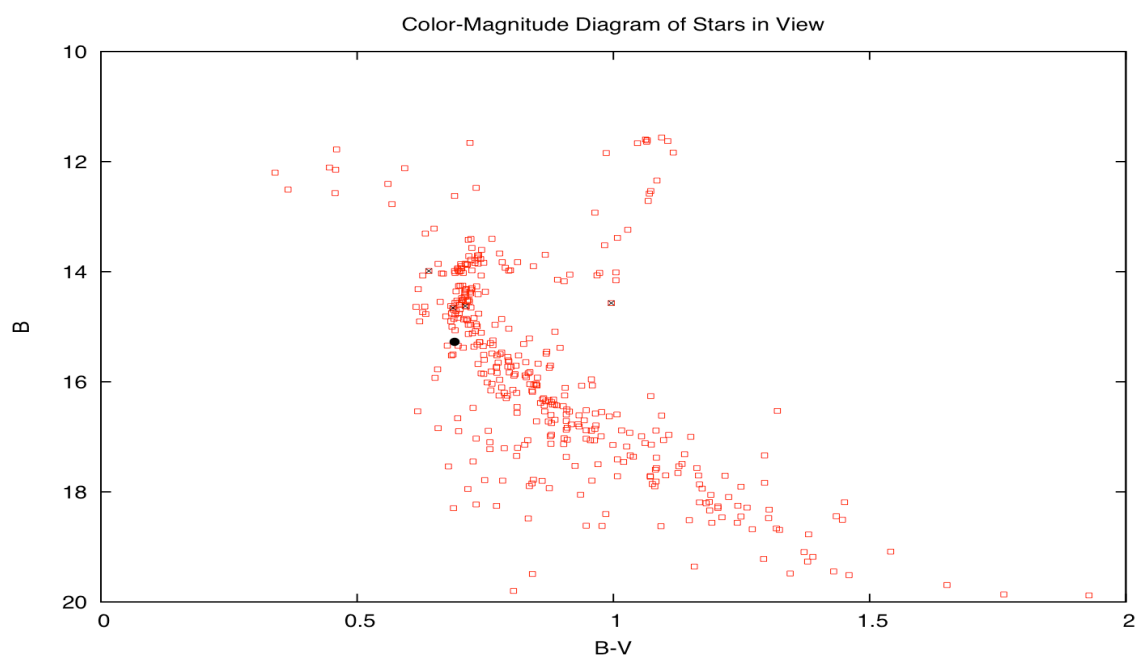


Figure 5.1 CMD of all stars in our field-of-view. The Sun is labeled with a filled black circle and designated variable stars are marked with an 'X'.

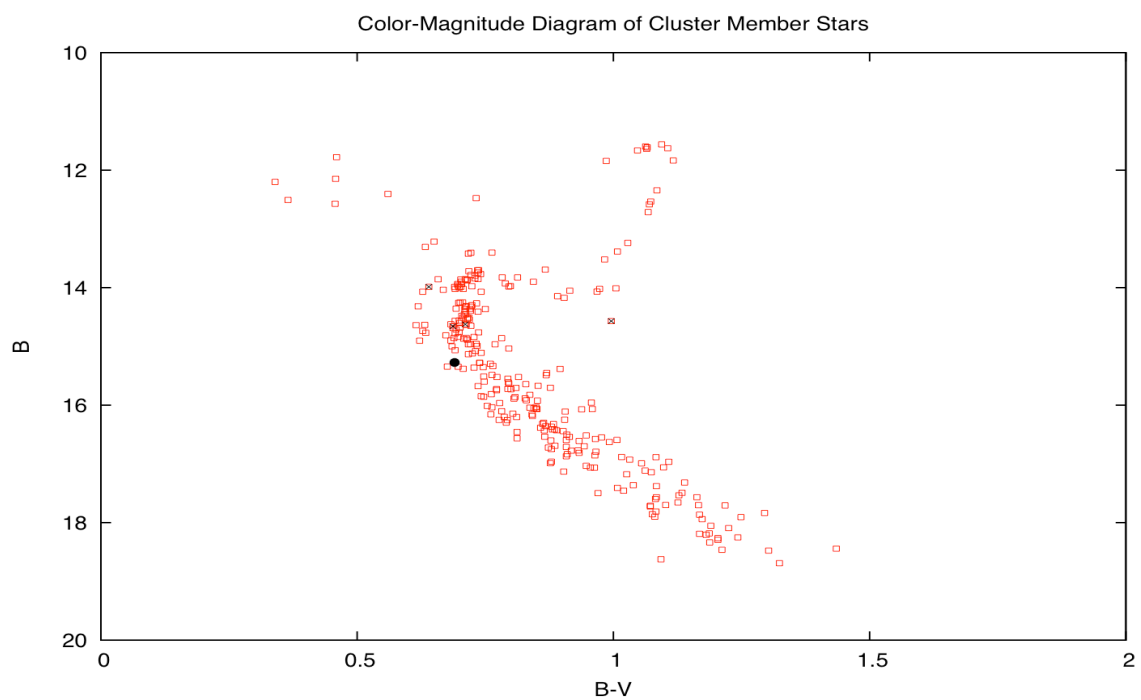


Figure 5.2 CMD of cluster member stars. The Sun is marked by a filled black circle, and designated variable stars are marked with an 'X'. The 'overall contraction phase' and binary sequence are visible.

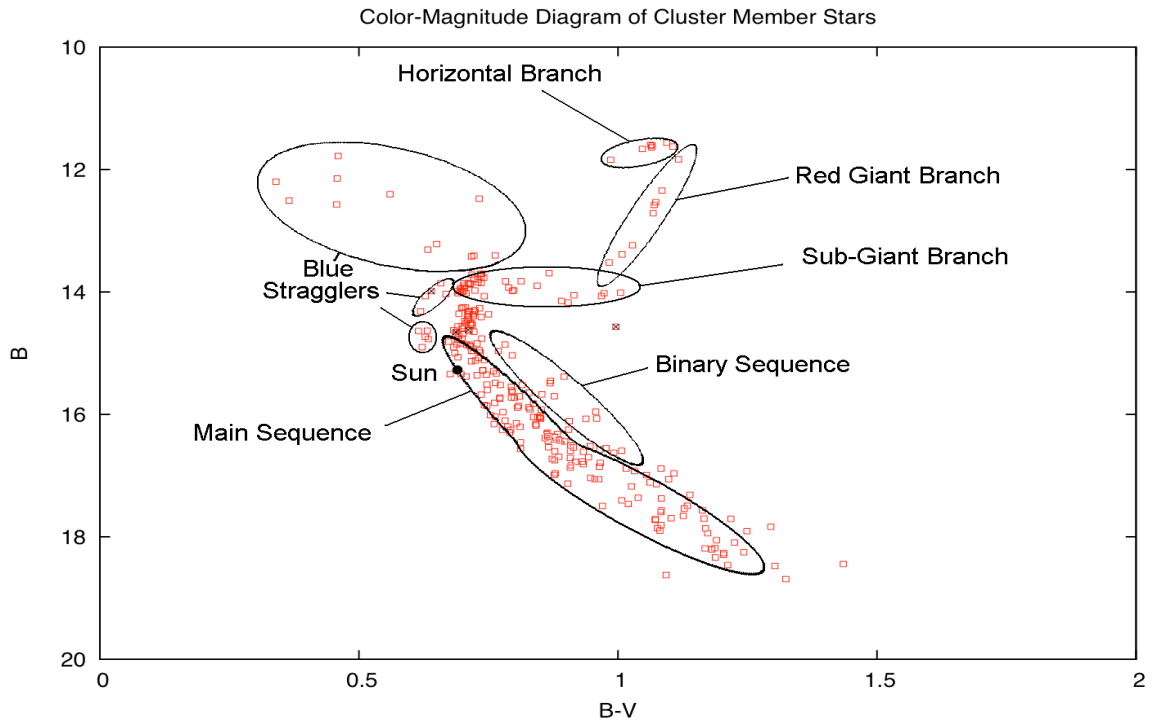


Figure 5.3 Labeled CMD.

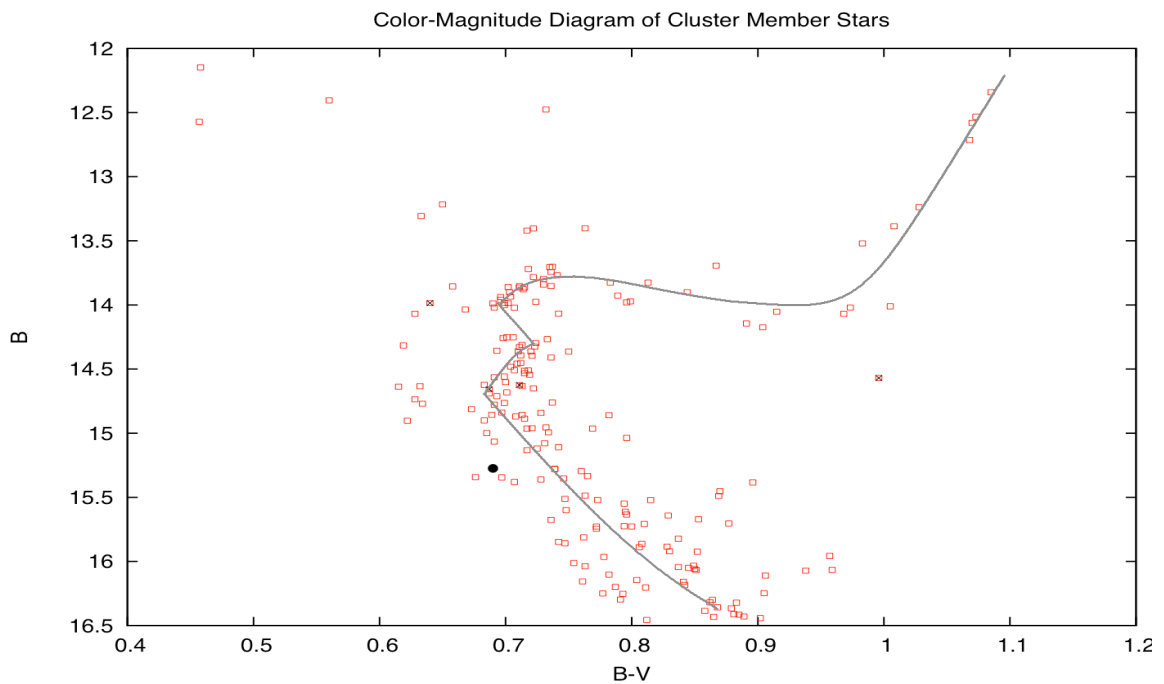


Figure 5.4 A closer look at the Turn Off reveals the bend (overall contraction phase) caused by convective core mixing in massive stars. The line is a guide for the reader and is similar to the shape and location of a plotted theoretical isochrone.

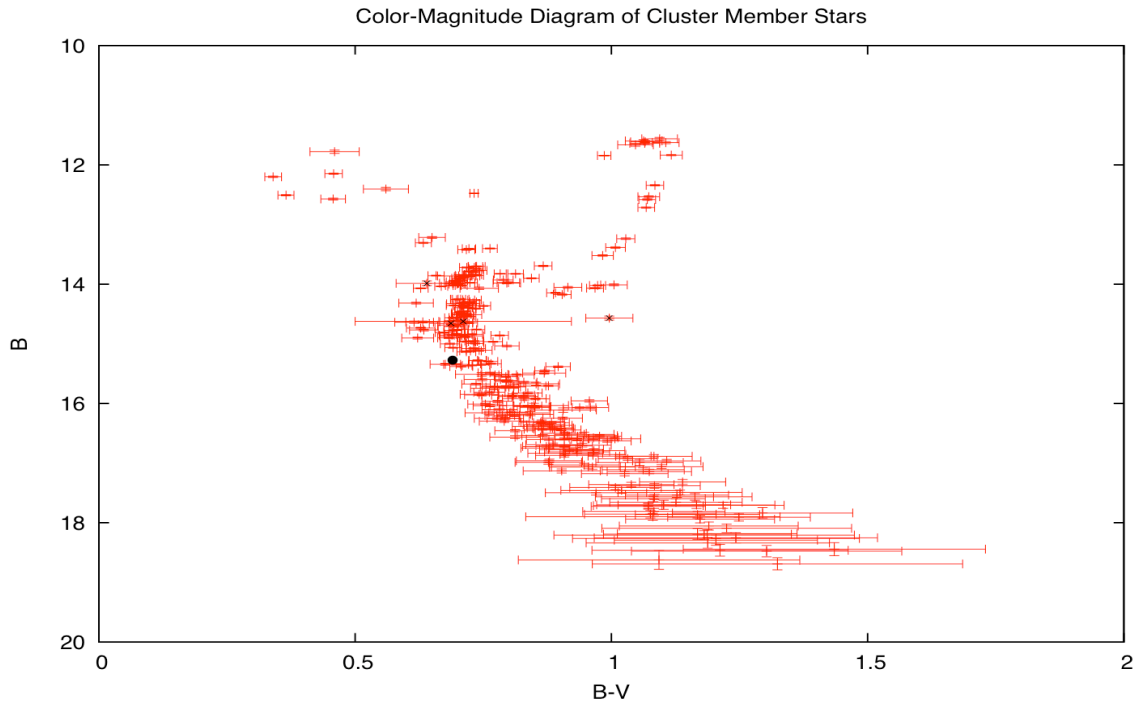


Figure 5.5 CMD of cluster members with error bars. The error bars in some cases can indicate a variable star. The unusual size of the error bar at the bottom of the turnoff indicates a large amplitude variable star at that location.

The second visible characteristic is the binary sequence (Figures 5.2 and 5.3).

This is a row of stars oriented like the main sequence, but positioned vertically higher than the main sequence. This feature of the CMD is well-documented for this cluster (Racine 1971; Sanders 1977; Girard et al. 1989; Montgomery et al. 1993; Stassun et al. 2002).

In Figure 5.5, we show a CMD with error bars. The horizontal error is largely due to the fact that conservative error propagation techniques were used to calculate the B-V error (see section 5.3.2). In this figure, we can tell several variable stars, just by the size of their error bars in relative to other stars of the same magnitude. The large error bar located near the turnoff of the sequence

indicates a variable star with a large amplitude. Variable stars like this will be discussed in the next subsection.

5.1.3 Variability

Variable stars were designated with the *Ensemble Photometry* program. For our data we recognized five variable stars. Four of these were previously identified by Balaguer-Núñez identification numbers and Sanders numbers. The

Table 5.1 Designated Variable Stars

ID	S77	\overline{M}_B	Period	Exp. Amplitude	Meas. Amplitude	Meas. σ
1176	1036	13.985	0.44 d	130 mmag	130 mmag	10 mmag
1352	1282	14.625	[†] 0.36 d	390 mmag	400 mmag	12 mmag
777	757	14.657	0.44 d	80 mmag	80 mmag	17 mmag
905	1063	14.569	~23 d	150 mmag	140 mmag	10 mmag

[†] Period varies with time. ID is the Balaguer-Núñez identification number. S77 is the identification number used in Sanders (1977). The expected amplitude is average amplitude found by Sandquist & Shetrone (2003).

fifth was extremely faint, and had not appeared in previous catalogs. The four identified designated variable stars were then checked against variable star catalogs for M67. Stassun et al. (2002) contained all four as verified variable stars, Sanders (1977) verified three. These four variables were studied more thoroughly by Sandquist & Shetrone (2003), and their properties are available in Table 5.1. Note that the measured properties are from the Ensemble program, including the average B magnitude. Light curves in B filter data are shown in figures 5.6-5.9. Each of the four variable stars matched their expected amplitudes.

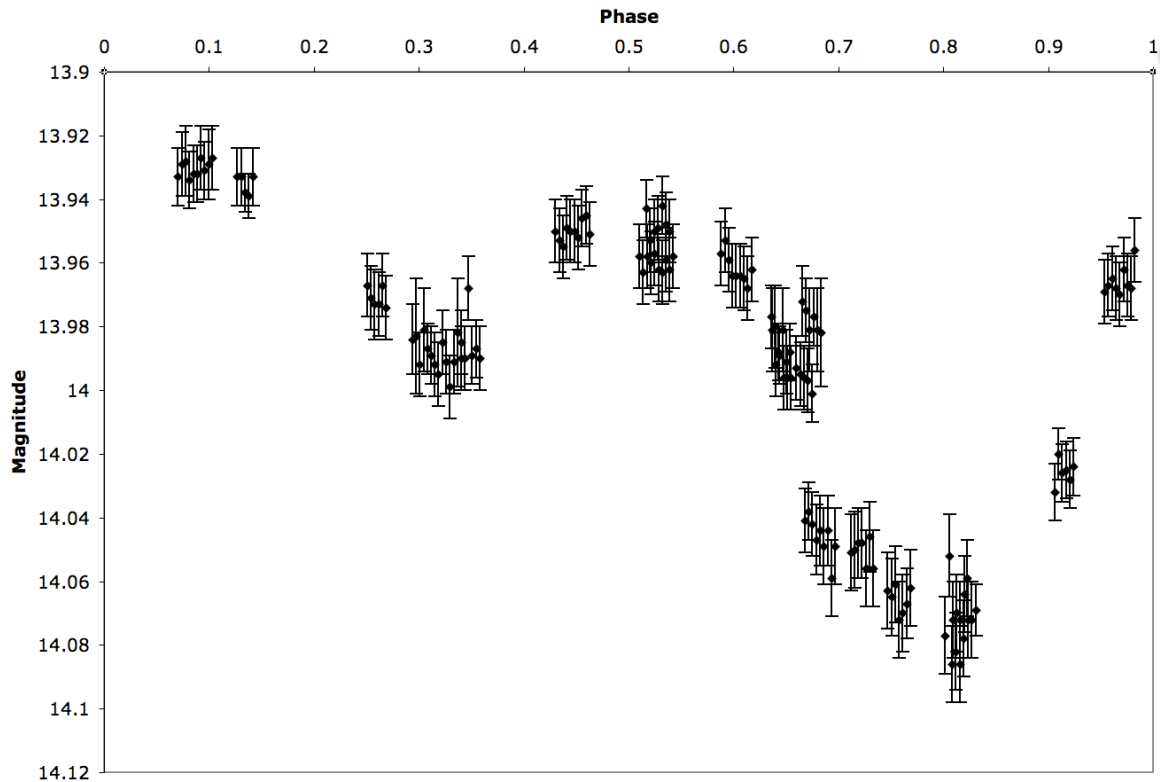


Figure 5.6 Light curve of W UMa system labeled 1176. Note the 0.02 difference in maximums and 0.09 difference in minimums.

5.1.3.1 Variable Star 1176

One of the brightest stars and X-ray sources near the turnoff, EV Cnc (1176) is classified as a blue straggler because it is nearly 100 millimagnitudes to the left of the turnoff locus on the CMD. Its period is 0.44144 days; and it is a W UMa binary system. The differences in maximums and minimums are discussed in Sandquist & Shetrone are still visible, and it is likely that the cause is not variable on short time-scales. It is important to note that this phased light curve in Figure 5.6 does agree with the period, minimum differences and maximum differences as observed by Sandquist & Shetrone.

This system is also known to be a W Ursae Majoris contact binary system. These systems display very high levels of magnetic activity. According to Ostlie

& Carroll (2007), these stars are important for studying the magnetic dynamo mechanism at extreme levels, and magnetic braking may cause these binaries to coalesce into single stars.

5.1.3.2 Variable Star 1352

Another W UMa system, AH Cnc (1352) is a well-known variable system

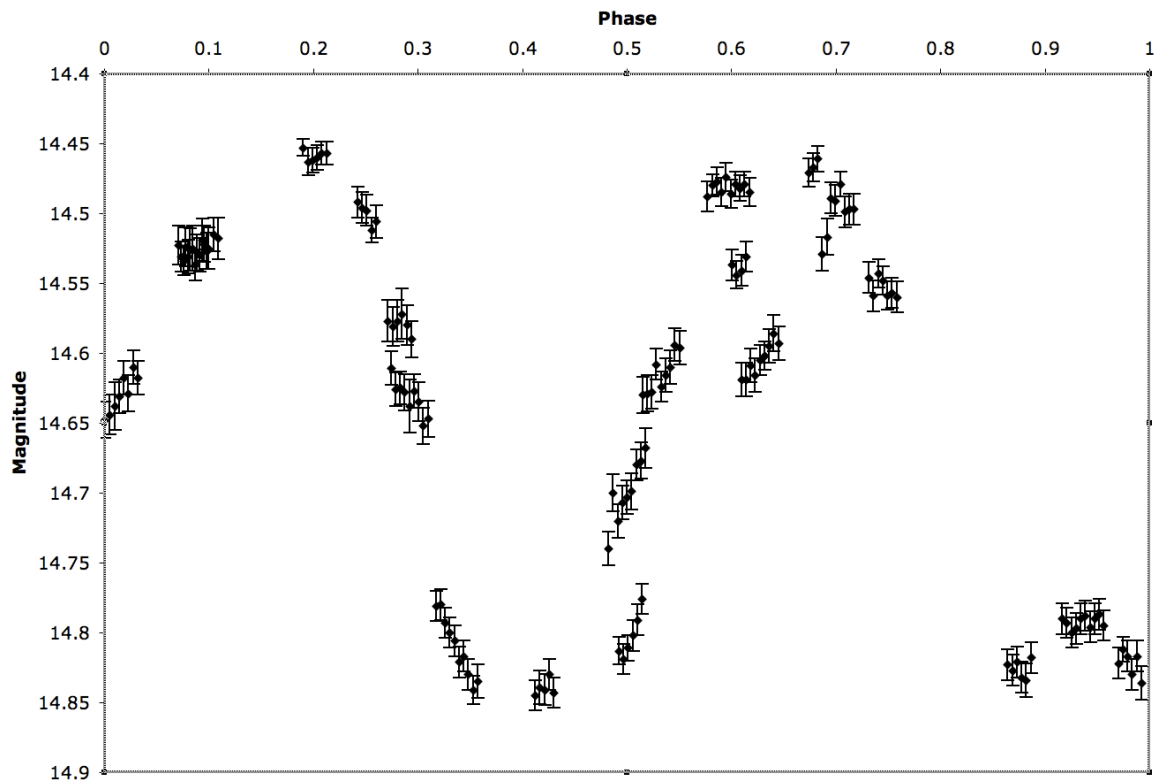


Figure 5.7 Light curve of W UMa system labeled 1352. Because of the consistently varying properties of the system, the light curve has discrepant points. There is a hint of flat bottoms indicating total eclipses.

and X-ray source. This system is an eclipsing system with a period of 0.360452 days. The peculiar nature of this variable system is that it continually changes its light curve, in period, amplitude, and even shape of minimums. At times the system shows no doubt of an eclipsing binary. Sandquist & Shetrone (2003) discuss several possibilities including high surface activity, including large

starspots, for the cause of random changes in the light curve. However, our measurements will need to be more precise before such changes can be properly characterized. This system's phased light curve can be seen in Figure 5.7.

5.1.3.3 Variable Star 777

This star is another W UMa system. The light curve in Figure 5.8 for this

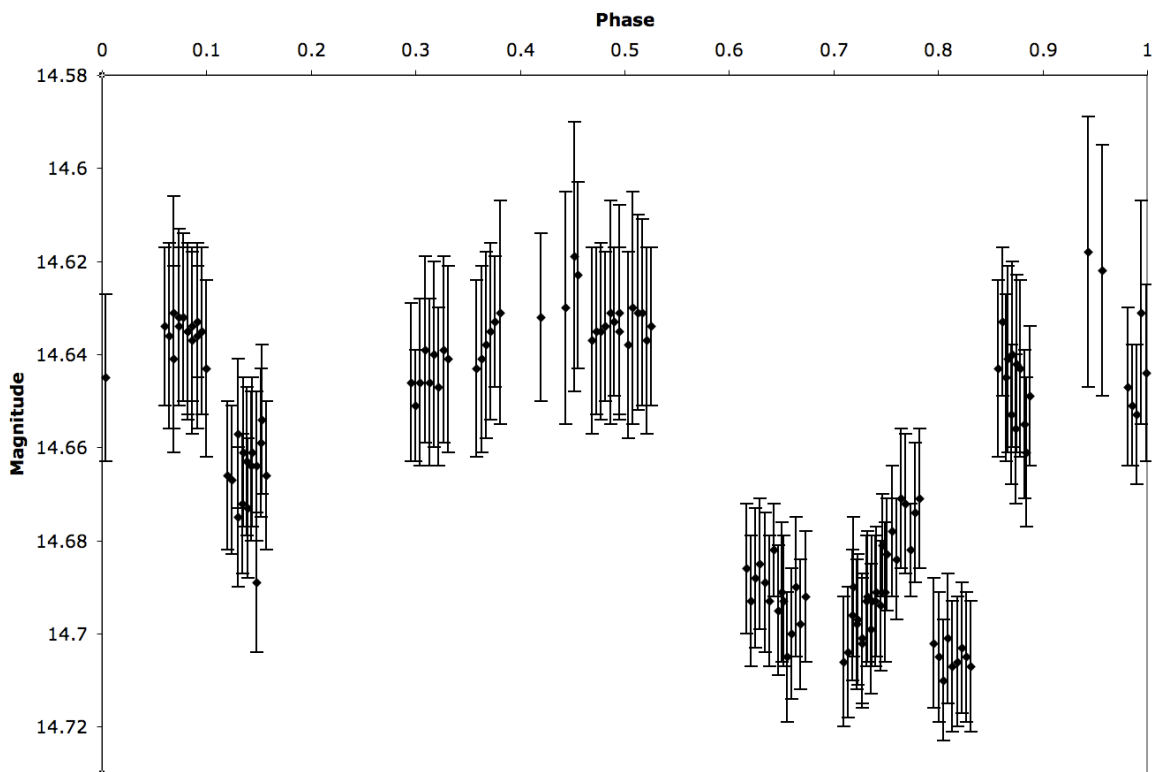


Figure 5.8 Light curve of the W UMa system labeled 777. Note that the precision is not much better than the amplitude of variability.

system matches the period of 0.35967 days. This star is known to vary due to the variable O'Connell Effect. This is where one peak will vary in relative to the other peak, sometimes dimmer than the other peak, sometimes brighter than the other peak. However, for this star, this effect is too small to be seen with the precision of our current data.

5.1.3.4 Variable Star 905

This star is the most peculiar star in the M67 cluster. It exists (and can easily be found) dimmer than the subgiant branch and nearly inline with the red giant branch. Another peculiarity is that it is an X-ray source (Belloni et al. 1998). Unlike the last three, this star is not a W UMa binary system. Its variability is not obviously linked to the orbital characteristics of the system. Sandquist & Shetrone (whose published data is the most recent for this object), indicate that

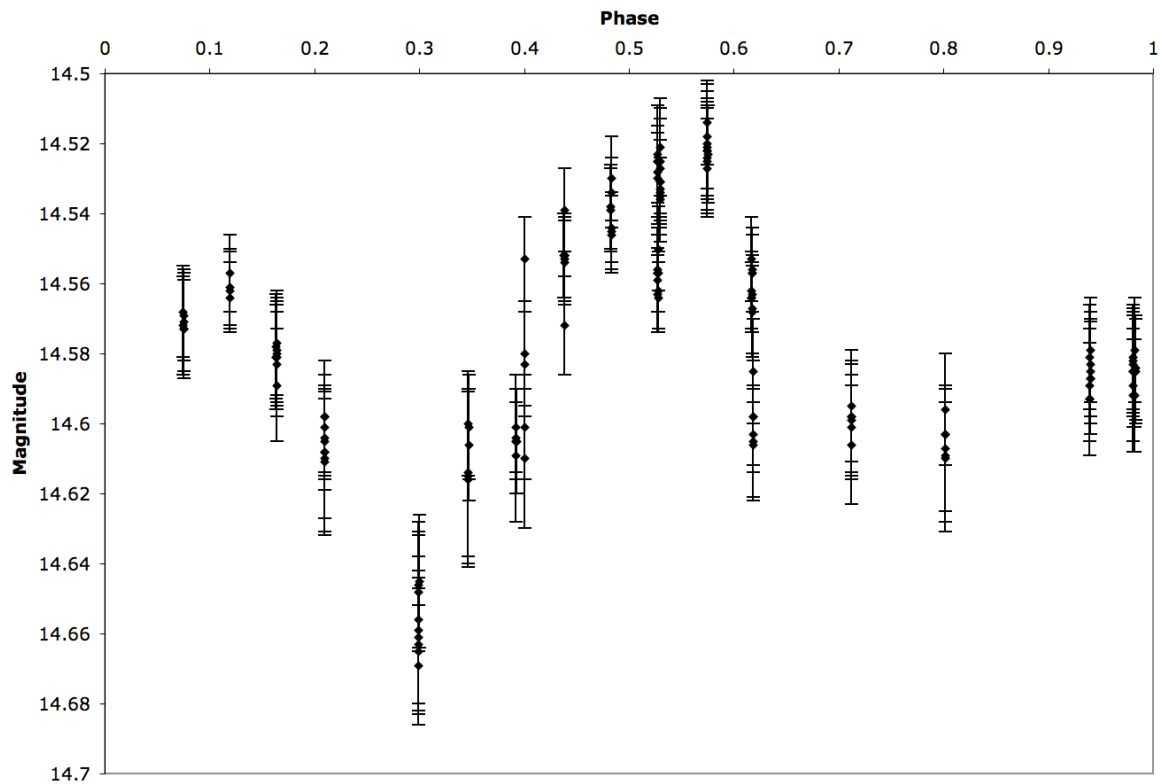


Figure 5.9 Light curve for the variable system labeled 905. This system is peculiar in its location and its variation of unknown origin. Note the variation of data points and error bars.

this system likely varies on multiple time-scales. Their data supports a primary time-scale of about 23 days. The measurements that we took indicate that the value should be closer to 22 days. Sandquist & Shetrone also indicate that there

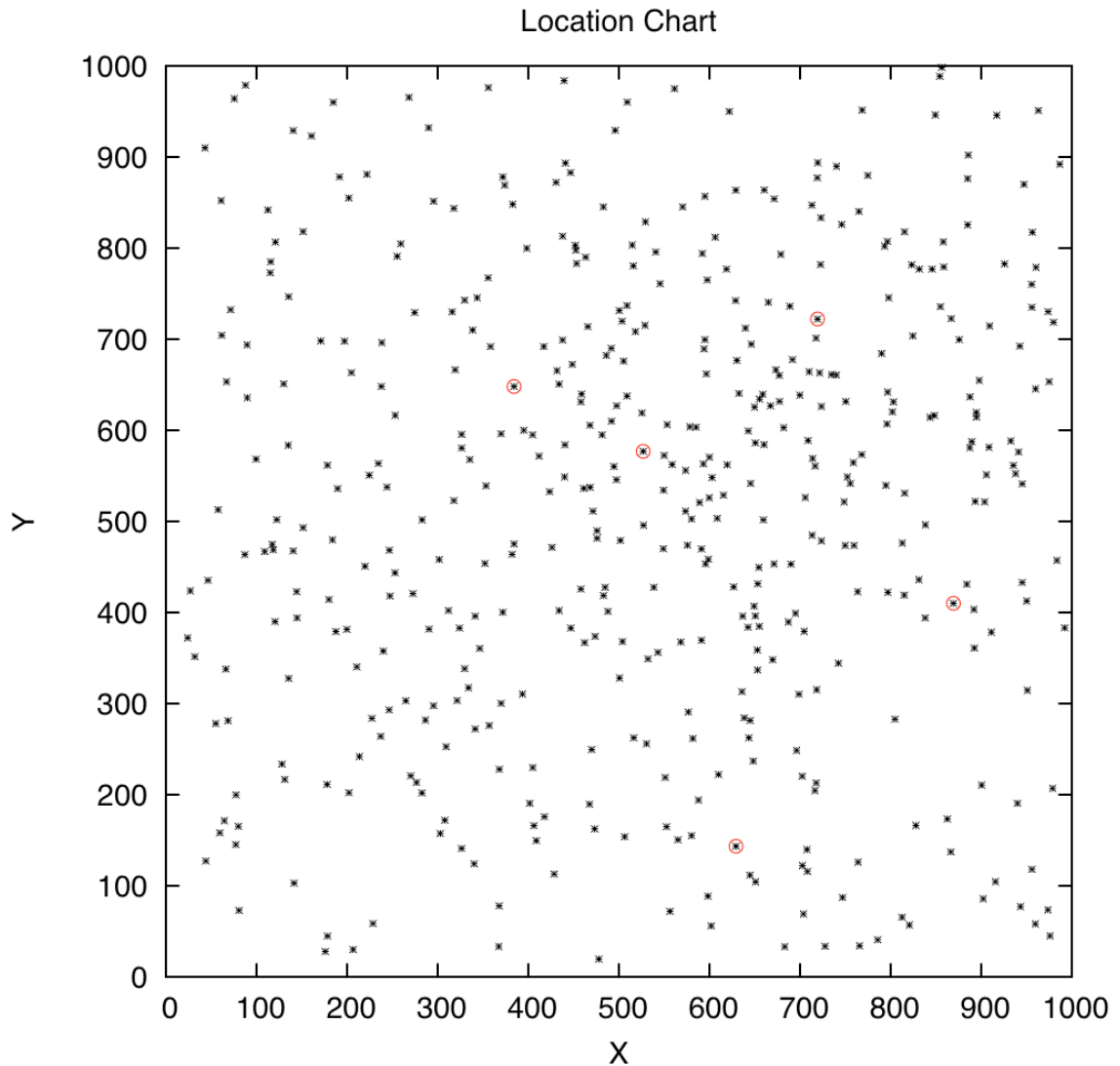


Figure 5.10 Variable star locations. Notice that these stars are well-separated from other stars. Axes units are in pixels.

was a large variation between cycles of the light curve. They state that the light curve probably varies by a tens of millimagnitudes from cycle to cycle. However, for our data the light curve is nearly dominated by error. To reduce the effect of error, we can complete a weighted average of multiple measurements on a night to get one data point per night. This should improve certainty. Normally we can do this if the variability of this star is on a time-scale of larger than a night. For

time-scales less than a day, the amplitude of variation would be significantly affected. However, the uncertainty of night averages are based on the spread of the data points of the images over a given night. Because of the spread of our data points is large, due to first-order extinction, this results in higher uncertainty than each image alone.

All measurements and light curves use the B filter data. This is because of two important reasons. First, the photometric variation is larger in shorter wavelengths (Pap et al.). Also, the data from the B filter have a higher S/N ratio, and therefore, smaller uncertainty. For the relative position of a star, refer to the map in Figure 5.10 where the designated variable stars are circled.

5.2 The Sun-like M67

5.2.1 Define Sun-like

Generally, all of the stars in the cluster have the same metallicity and age as the Sun. The primary difference between the stars in the cluster and the Sun is the mass of those cluster members. Since we will not be deriving masses in any way in this research (which is in no way trivial, considering the large portion of binary systems present), we are left with two choices. Take a subset of the whole and compare the variability, or use the entire cluster and compare the variability between all stars. Since we are not interested in the variability of red giant stars, blue stragglers or lower main sequence stars, the answer is to take a subset.

We select a subset of cluster members by defining a box, equally brighter and dimmer than the Sun and equally bluer and redder than the Sun. This box is defined by two criteria. First, the box will not contain obvious members of the binary sequence, and secondly, the box will not contain obvious members of the subgiant branch. Figure 5.11 shows how the box is set on the CMD. This box is defined as ± 0.5 magnitudes vertically by ± 0.075 magnitudes horizontally from the solar magnitude and color. Variability of all of the stars that reside in this box will

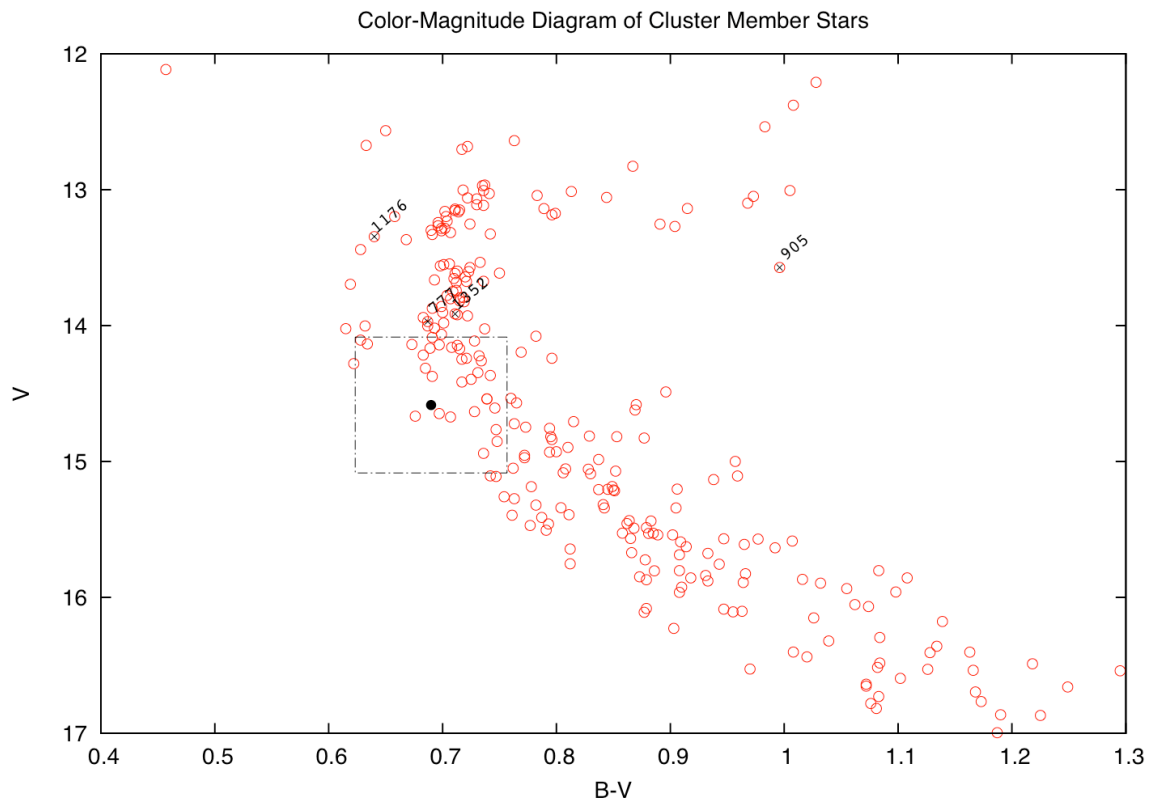


Figure 5.11 CMD with variables marked and box indicating the definition of Sun-like stars. The black filled circle is the Sun and designated variables are both marked with an 'x' and labeled.

be compared.

The box surrounds 36 stars. After reviewing Stassun et al. (2002) for known variable stars within the region, we found that two of the 36 stars were

known variables. One of them (star 1006) is a single star and one of them (star 1029) is a binary system. The variability of the single star has an amplitude of 23 millimagnitudes and the other is 15 millimagnitudes according to Stassun et al.. Our measurements show that these stars have uncertainties of 12 and 11 millimagnitudes, respectively. These uncertainties, however, are similar to other stars with the same magnitude. Because of this, it is unlikely that our measurements show any variability of these two stars.

Since little data is available on the variability of the single Sun-like star, it is possible that the variability is based on stellar surface activity. The expected amplitude of variability of this star is at the level that we would expect to see from surface activity. The star's location on the main sequence is a near mirror-image of the Sun, and it is located in a relatively sparse neighborhood in the cluster making the detection of photometric variability likely in future observations. Further investigation is necessary to confirm the nature of this variability.

5.2.2 Solar-type Stars with Relatively-High Uncertainty

Of the 36 Solar-type stars that we detect, we find that some of them have uncertainties higher than the two known variables. Uncertainty in the Sun-like region of M67 is from 10 to 14 millimagnitudes. Two stars have uncertainties of more than double these values (1604 and 1569), indicating that this uncertainty is from something other than typical measurement error.

Each of these stars, however, are located near the corners of the frames where vignetting effects are strongest. To explore this effect, we examine the uncertainty of several stars of similar magnitude, both near the corners of the

frame and near the center. We find that uncertainty appears to increase significantly near 550 pixels. The average increase in uncertainty is 8 millimagnitudes for corner¹ stars and less than 2 millimagnitudes for central² stars. Because of this, we determine that this variability is a result of vignetting, and should be considered when confirming designated variables.

Four other stars (1348, 728, 646, 663) are found to have higher-than-expected uncertainties in the Sun-like region. None of these four are previously known as variables. However, because their uncertainty is less than double the standard deviation of the scatter of stars for Sun-like magnitudes, the uncertainty may be due to neglected error sources. After checking to see if any of these stars are located in vignetting regions (corners and edges) of the frame, we find that each star is near the edge of the observation region. Larger uncertainties would occur if partial starlight is lost due to the FWHM of the star falling off the edge of an image.

Other variability in Sun-like stars is difficult to differentiate from measurement errors. Other stars that have higher-than-average uncertainties have increased uncertainties around 2-3 millimagnitudes. However, since the uncertainties of these stars have a standard deviation of 4 millimagnitudes, this error is only due to the scatter of the measurements.

¹ Stars whose radius from the center is larger than 550 pixels

² Stars whose radius from the center is smaller than 550 pixels

5.3 Single versus Binary

In this section, we examine stars in known binary systems. We are checking to see if there is a correlation between variability and binary systems. To do this, we use the catalog of known multiple systems presented in Sandquist (2003), of which we have detected 22 systems. Using the average uncertainty, as we did in the previous section, we find that several systems exhibit uncertainties that are higher-than-average: 18 out of 21 systems.

5.3.1 Uncertainties

Ensemble Photometry uses uncertainty as a marker for variability in the variability score of the program output. Significant uncertainty results in being flagged as a variable. However, to be designated a variable star, the star must be variable in both filters. Though this process has resulted in four correctly-identified variable stars, some variable stars are likely lost in the process because their variability in the V filter has a smaller amplitude.

The uncertainty levels for the four recovered variables are more than 20 millimagnitudes above the average. Another star, however, has uncertainty in the B filter that is comparable to the four recovered variables. After checking previous studies, this star is a well-known RS Canum Venaticorum (hereafter RS CVn) variable star (Stassun et al. 2002; Sandquist et al. 2003; van den Berg et al. 2001).

Thirteen of the 18 higher-than-average systems have uncertainties that are on the order of the scatter of the system. Upon checking for known variability in these systems, two stars are known to be variable according to Stassun et al.

(2002), and one is a known Am star with flare detected by Sandquist & Shetrone (2003). However, these uncertainties are within the scatter of measurements of the system.

5.3.2 RS CVn System 1046

According to Ostlie and Carroll (2007), these kinds of stars are known to

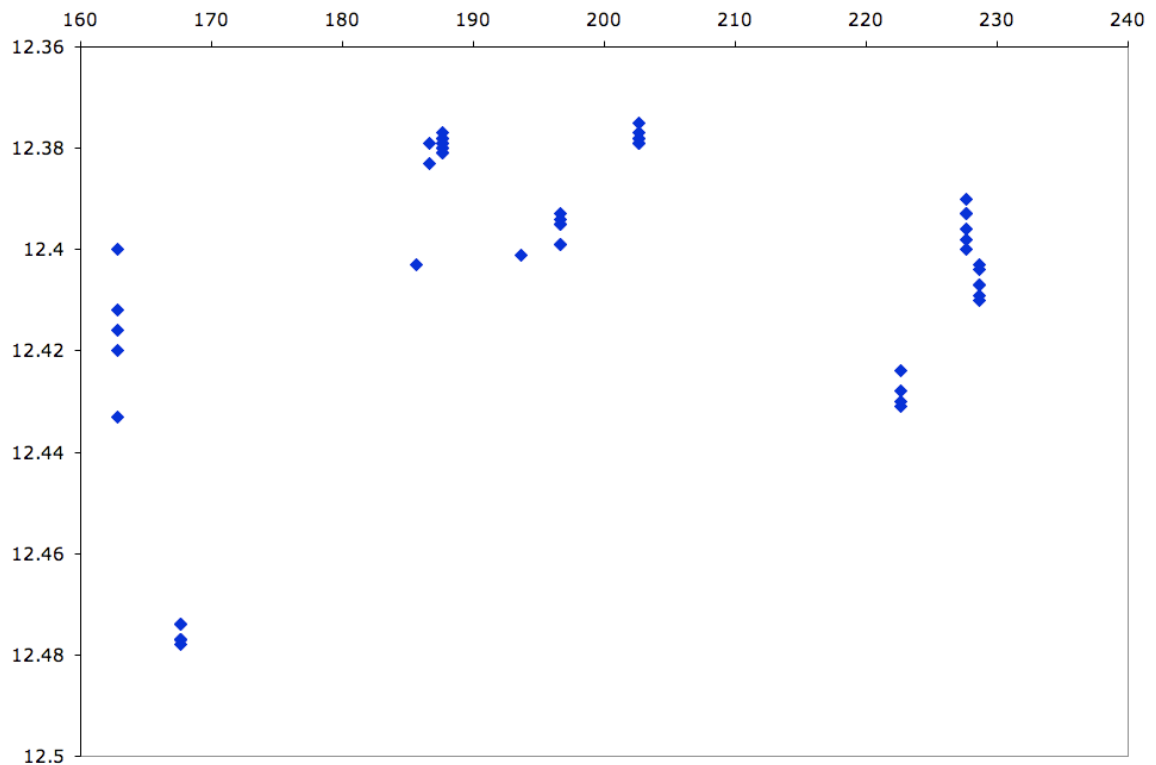


Figure 5.12 A light curve showing the variability of the RS CVn system. The horizontal axis is in Julian date, and the vertical axis is in B magnitude. Note that the light curve varies by about 107 millimagnitudes.

be tidally locked binary systems with enhanced magnetic activity. This enhanced magnetic activity manifests as starspots, flares and other processes that cause photometric variation. Furthermore, the typical timescale of photometric variations are believed to be significant in long timescales.

The expected variation of this star is 115 millimagnitudes (Stassun et al. 2002; Sandquist et al. 2003) based on the orbital period of the system. However, our measurements only show 20 millimagnitudes of increased uncertainty. A view of the light curve in Figure 5.12 shows that the uncertainty determined by *Ensemble Photometry* is only a standard deviation of the variation of the star, whereas the maximum amplitude of variability may be much larger than the uncertainty. Due to the period of orbit (1.06 days), the variation may elude observations over a two month timescale. Any surface activity would be seen as a deviation from a natural light curve. This deviation is expected to be about 20 millimagnitudes (Sandquist et al. 2003), however, we have too few of observations to estimate a light curve.

5.4 Uncertainties and Errors

As with any experimental science, the most valuable part of the discussion is the uncertainty of the measurements. We discuss error contributions from multiple sources including corrections to systematic errors and characterization of random errors.

5.4.1 General Uncertainties

Photometric measurements can be characterized by the measurement's signal divided by the noise in ADUs. The CCD equation below gives the S/N ratio (this is SNR in the equation):

$$SNR = \frac{gN_{star}^{net}}{\sqrt{gN_{star}^{net} + ngN_{sky} + ngN_{dark} + nN_R^2}}$$

where g is the gain, n is the total number of pixels in the aperture, N_{star} is the number of counts for the star in question (without sky contribution), N_{sky} is the sky count per pixel, N_{dark} is the number of counts from dark current. N_R is the readnoise. For our data, N_{dark} is nearly zero so we can disregard it.

However, there are several problems that can ruin a photometric observation. Observing a star at a part of the CCD where pixels are ‘bad’ will cause loss in data. For each of the variable stars we found, each were checked to ensure that they were not located where a bad pixel can have a large effect.

Other problems include the naturally occurring cosmic rays. Cosmic rays are high-energy atomic particles that travel near the speed of light. Once they enter the atmosphere, they create a particle shower. These particles cause streaks across the image. Cosmic rays are most easily removed by comparing multiple images, since each cosmic ray bombards the CCD at a different location. When you cannot combine images, or you are completing time-series photometry, each measurement should be checked for an unusual spike in photometry; this would indicate a likely cosmic ray in the data. Overall the effect of cosmic rays is small for Earth-based photometry, and so the error from this source is usually insignificant.

5.4.2 Propagation of Error

Errors from measurements must be maintained through any data manipulation. This includes standard procedures like additive and multiplicative error propagation:

$$z = x + y, \quad z = x - y \quad \text{uses} \quad \sigma_z = \sqrt{\sigma_x^2 + \sigma_y^2}$$

$$z = xy, \quad z = \frac{x}{y} \quad \text{uses} \quad \sigma_z = \sqrt{\left(\frac{z}{x} \sigma_x\right)^2 + \left(\frac{z}{y} \sigma_y\right)^2}$$

These are standard methods for simple procedures. The rest of the subsection will be based on the more complicated procedures.

5.4.2.1 Data Reduction Errors

There are two sources of random error from the data reduction method. The first is bias drift. The value of the bias offset will vary based on varying conditions of the electronic components. To ensure that this error does not affect our data, it is important to employ bias calibration images nearest in time to the science images.

The second source of random error can come from the calibration flats. This is based on the S/N level of the flats. When the flats are combined, their total signal is additive. Error from applying a master flat is important only if the total counts from the flat is comparable to or less than that of the maximum signal of any science image. Over all groups, the lowest average for a master flat is 268,000 counts per pixel. Since we require our science data to conform to the linear regime of the CCD, we can safely say that each star is dimmer than 26,000 counts per pixel. Because the counts per pixel is much higher than the brightest star, the contribution of error from the master flats is insignificant for our data.

5.4.2.2 List Matching, Astrometry and Blended Stars

If there is an error in matching stars, the result would be the misidentification of a star. Since the matching routine discards any matches

worse than 4 pixel difference between lists, there is a very low probability that a star was misidentified. Astrometry would have even less contribution since the average error of the fit was under an arcsecond.

After the first run of *Ensemble Photometry*, the majority of designated variables were stars with brighter optical companions. Because of this, we removed stars that had any optical companions within two FWHM (10 pixels). This removed the last possible error contribution from misidentification.

5.4.2.3 Optimal Photometry

The design of this program was to complete a complicated algorithm in order to improve photometric uncertainties. Since we found that aperture photometry had better uncertainties, error contribution from this step is straightforward to determine. The user specifies an aperture. The program calculates the sky background per pixel by removing the effect of stars via fitting a point-spread function to each detected star. Once this is completed, the photometry of the star is the total number of counts of the star and the uncertainty is based on the CCD equation listed on a previous page. The uncertainty in the measurement is the inverse of the S/N ratio.

5.4.2.4 Color Corrections

The error from this step comes from confidence of the linear fit and the uncertainty of the data points to the known source. Since it is a second-order adjustment, the error from this step is small. For the purposes of this research we will assume it is negligible.

However, to review the amount of error that this calculation may provide, we use the standard procedures above. First, we must find the uncertainty of the regression coefficient using the equations found in Birney et al. (2006):

$$\sigma^2 = \frac{1}{n} \sum (\delta y_i)^2$$

$$\sigma_b^2 = \frac{n \sigma^2}{n \sum x_i^2 - \left(\sum x_i \right)^2}$$

where n is the number of stars used in the linear regression, x is the instrumental color of a star, y is the standard color of a star, and σ_b is the uncertainty of the regression coefficient (the variable used for the regression coefficient is A_1). The value that we typically find for σ_b is 0.04.

Next, we can use the standard procedures at the beginning of the section to calculate a conservative estimate for the typical sun-like star. The typical error for Sun-like star is 0.01 for B and 0.016 for V. Therefore, B-V would have an uncertainty of 0.019. Color effects are removed by multiplying the regression coefficient by the instrumental color, and subtracting that value from the instrumental magnitude.

Average instrumental values for B, V and B-V are -11.6, -11.5 and -0.08 respectively. The resulting error from multiplying the regression coefficient by the instrumental color is 0.019. Finally, we see that the error of converting our instrumental magnitudes to standard magnitudes produces a final error for 0.021 in B and 0.025 in V. This is 11 millimagnitudes higher in B and 9 millimagnitudes higher in V. At first glance, we can already see an improvement: Section 4.3.2

reports that a typical error from not correcting for second-order extinction is about 28 millimagnitudes, higher than our maximum error estimate of 11 millimagnitudes.

However, since *Ensemble Photometry* uses all the stars in each frame to find variable stars, and it does not account for second-order extinction, it is likely that not correcting for this here could be extremely detrimental to the functionality of *Ensemble Photometry* program.

It is also important to note that this conservative error is extremely dependent on the error of the original errors, and that the contribution of the regression coefficient is insignificant. If our regression coefficient error stays the same, and our uncertainties are lessened, the resulting error from color-correction is also lessened. Furthermore, since the uncertainty of the observation scales with magnitude, the uncertainty of the color-correction step also scales with magnitude.

5.4.2.5 *Ensemble Photometry*

This program is designed to correct both photometry and uncertainties. For errors, the original uncertainties are converted into weights (w_j) and the final uncertainty follows the standard process of Bevington (1969):

$$\sigma_i^2 = \frac{N \sum w_j (m_j - M_i)^2}{(N - 1) \sum w_j}$$

where the variables are explained in Section 4.4.2.2.

5.4.2.6 Group Statistics

Using multiple images across a single night reduces the uncertainty for that night. This is useful in two ways. First, variables with periods longer than a day will benefit from having higher precision data points for a light curve. The second way is that scintillation effects can be measured and characterized. This step, however, requires correcting for first-order extinction effects across the frame and over the duration of the cadence of observations (see Section 5.4.3). Though we have not used this method to produce useful data, it is a necessary step to complete the research.

Theoretically, we can model the effect uncertainty sources by using the CCD equation and a theoretical estimate for scintillation. To do this, we must combine several parts, all of which can be found in Birney et al. (2006). First, scintillation noise can be found by using the equation:

$$\varepsilon = 90 \frac{X^{\frac{7}{4}}}{D^{\frac{2}{3}} \sqrt{2t}} \left(\frac{\lambda}{550} \right)^{-\frac{7}{12}} \exp\left(-\frac{h}{8000}\right)$$

where X is the airmass of the observation, D is the aperture of the telescope in centimeters, t is the exposure time, λ is the wavelength in nanometers, h is the elevation above sea level in meters, and ε is the scintillation noise in millimagnitudes. For λ , we use the center wavelength of the filter. Other values are listed in Chapter 3. A plot of how scintillation noise changes as a function of airmass is shown in Figure 5.13. Note that the curve is different for each filter, the top curve is from the V filter information, and the bottom curve is from the B

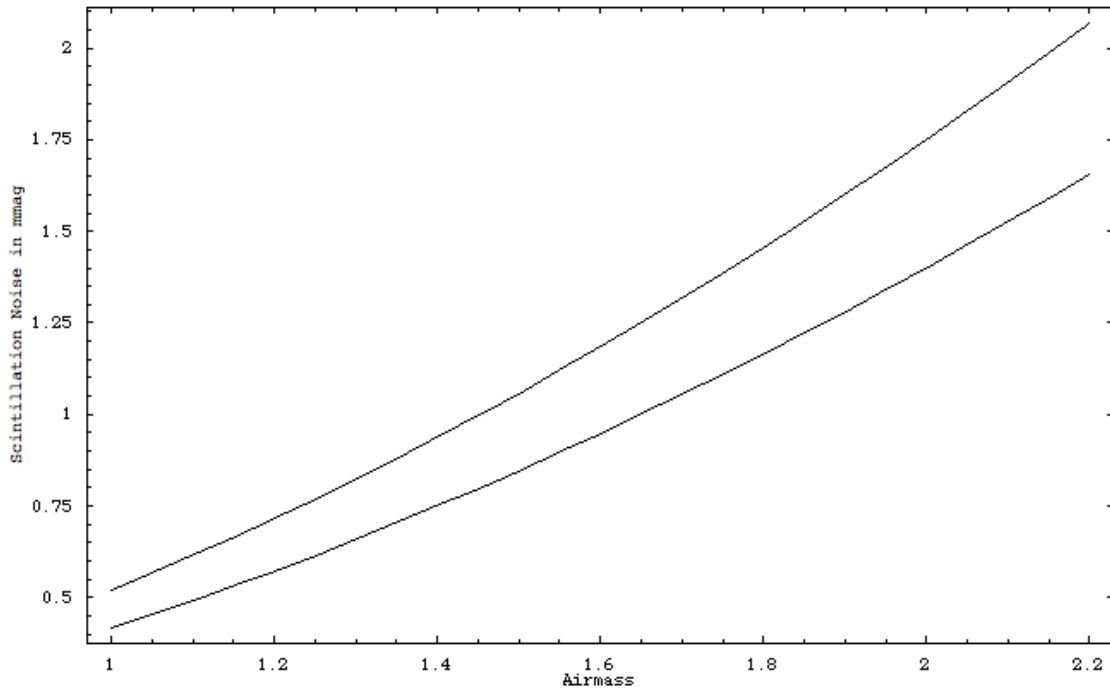


Figure 5.13 Plot of scintillation noise in millimagitudes versus airmass. Typical airmass for our observations is closer to 1.2, and never exceeds 2.0. The top curve is using the V filter characteristics, whereas the bottom curve is using the B filter characteristics.

filter information.

Another equation that is necessary is the relationship between magnitude and net star counts¹:

$$m = C - 2.5 \log(N_{star}^{net}) + 2.5 \log[t]$$

where m is the magnitude and C is a constant of the observation. C can be found by using the data, and comparing the net star count to its magnitude and solving for C . For our observations, we find that C is 20.7816 and 20.8593 for the B and V filters, respectively. Solving for net star counts as a function of

¹ Net star counts are the total number of counts within the aperture of photometry after subtracting the total sky counts.

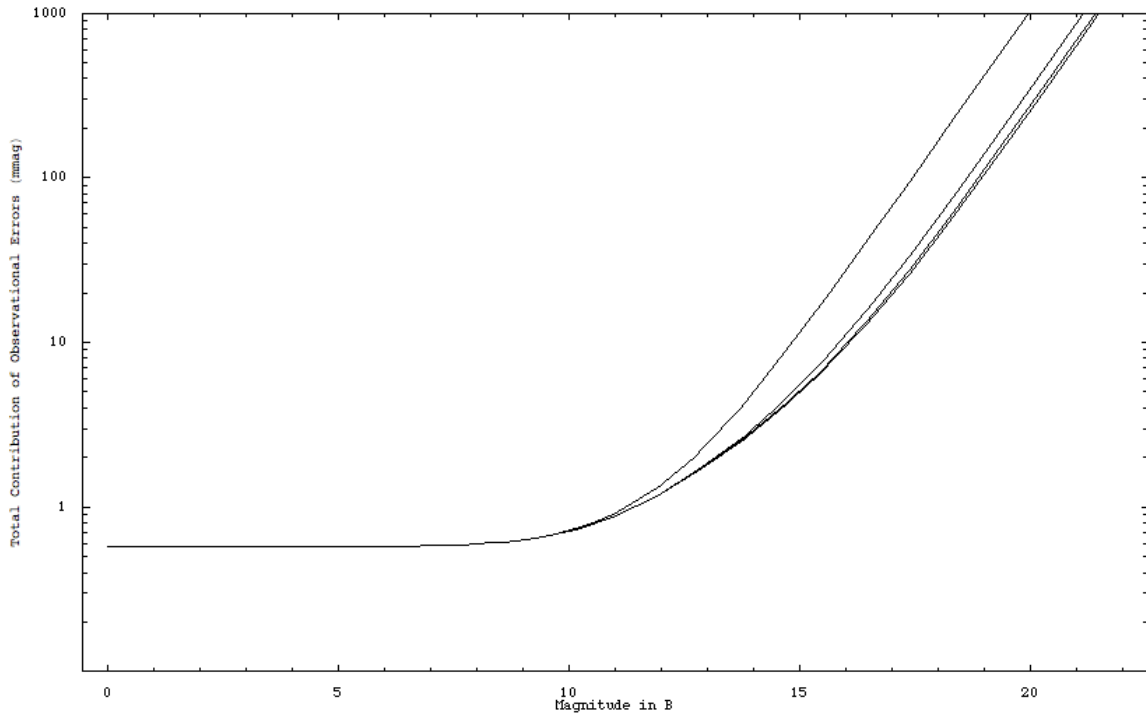


Figure 5.14 Sigma versus magnitude plot. Vertical axis is in milli-magnitudes. Note that there are several curves, each represent a different background sky count per pixel. Higher background sky count per pixel values result in the leftmost curve, whereas lower count per pixel values result in the rightmost curve.

magnitude:

$$N_{star}^{net} = t^{2.5} \sqrt{10^{C-m}}$$

Another equation that is necessary for our is the CCD equation. We mentioned this briefly at the beginning of Section 5.4. Here the equation is:

$$SNR = \frac{gN_{star}^{net}}{\sqrt{gN_{star}^{net} + ngN_{sky} + ngN_{dark} + nN_R^2}}$$

S/N ratio is measured in magnitudes⁻¹. By inverting, we are using the noise to signal ratio. This can be expressed as an uncertainty. We combine

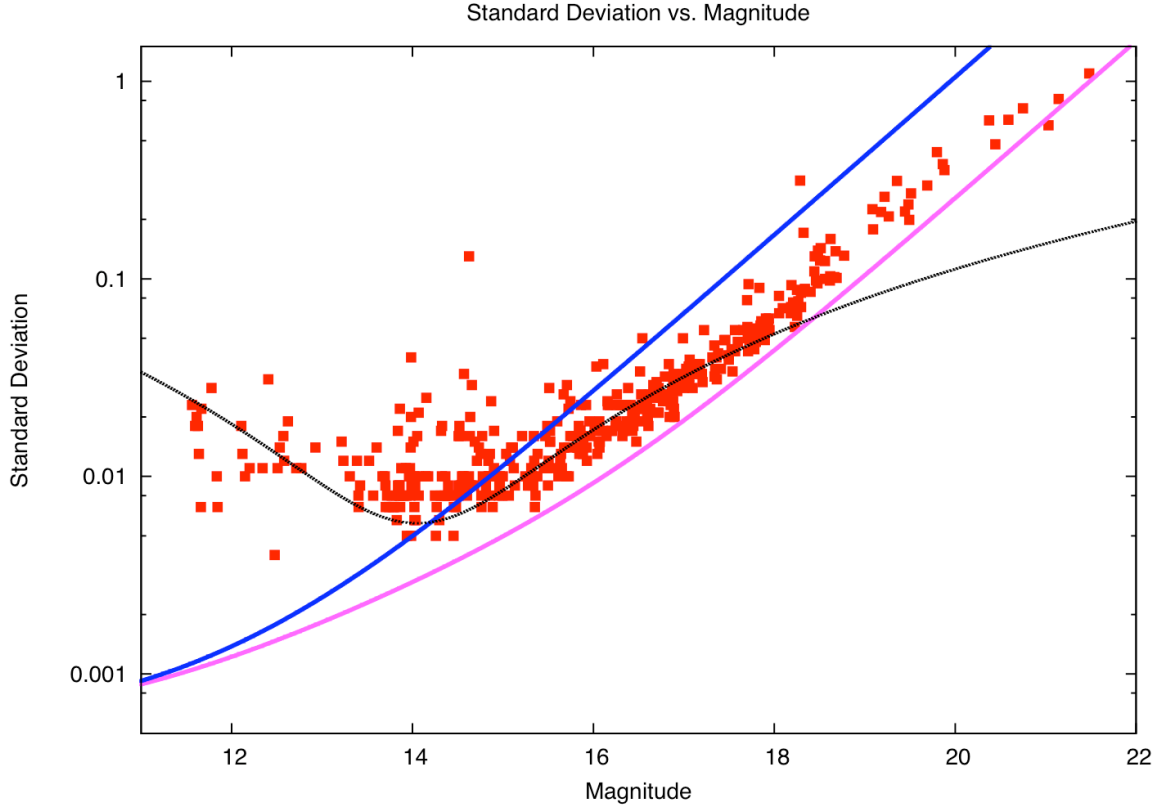


Figure 5.15 Standard deviation versus magnitude plot. The black line is the *Ensemble Photometry* parabola that is fit to the data. The blue curve (on top) is the estimate of error using the highest sky counts per pixel. The pink curve (on bottom) is the estimate of error using the lowest sky counts per pixel.

independent uncertainties by adding in quadrature, so:

$$\sigma^2 = \varepsilon^2 + \frac{1000^2}{SNR^2} = \varepsilon^2 + 1000^2 \frac{gN_{star}^{net} + ngN_{sky} + ngN_{dark} + nN_R^2}{g^2N_{star}^{net^2}}$$

and including the net star counts as a function of magnitude:

$$\sigma^2 = \varepsilon^2 + 1000^2 \frac{gN_{star}^{net} + ngN_{sky} + ngN_{dark} + nN_R^2}{g^2 \left(t^2 \sqrt{10^{C-m}} \right)^2}$$

N_{dark} is nearly zero, so we can remove that term. The others are known or estimated using our data. Readnoise and gain are found in Chapter 3. The n is the number of pixels in the aperture. Since the aperture radius is five pixels, the

total number of pixels in the aperture is 78.54 pixels. N_{sky} is the number of counts per pixel that the sky background contributes. This value can be different for a variety of situations. For example, the N_{sky} value is 1900 counts per pixel during a clear night with a full moon. For a clear night without a full moon, this value is only 100 counts per pixel. Once a value is chosen, we can plot σ versus magnitude, as shown in Figure 5.14.

This is a theoretical model of how our data should look when plotted. To compare this to our data, we overlay this plot on top of our data plots, as shown in Figure 5.15. Since the data points (in red) are from the *Ensemble Photometry* program, the values should correspond to an average sky count model.

5.4.3 First-Order Extinction

In this project we have neglected the effects of first-order extinction in our magnitude determinations. This is because: 1) we are using a differential ensemble photometry program, so the zero-point of the system will not matter, and 2) we are assuming that, for each image, the extinction effects across the frame are constant. This second point is where we find trouble. We can, however, calculate the maximum contribution to error of neglecting first-order extinction.

Using average first-order extinction coefficients $k_B = 0.39$ and $k_V = 0.25$ (Birney et al. 2006), we can estimate the maximum contribution from extinction to our differential magnitudes. Applying Bouguer's law to photometric measurements at two different values of airmass:

$$m_{\lambda_0} = m_{\lambda} - k_{\lambda}X \quad \text{and} \quad m_{\lambda_0} = m_{\lambda'} - k_{\lambda}X'$$

where $m_{\lambda,0}$ is the intrinsic magnitude, m_{λ} is the observed magnitude, k_{λ} is the extinction coefficient for some particular wavelength λ , and X is the airmass at a point in time. Subtracting the second equation from the first, and assuming that the first-order extinction coefficient is constant between the observations, we find that:

$$m_{\lambda_0} - m_{\lambda_0} = 0 = m_{\lambda} - m_{\lambda'} - k_{\lambda}X + k_{\lambda}X' = \Delta m - k_{\lambda}\Delta X$$

$$\text{simplified, } \Delta m = k_{\lambda}\Delta X$$

So, the difference in magnitude due to first-order extinction is based on the difference in airmass of the two separate observations. Airmass, however is not constant over the duration of an image, nor from one edge of the image to the other. If we examine stars with the same color and magnitude (thus canceling any contribution of second-order extinction), first-order extinction will depend upon the difference in airmass between those stars.

For our data, we calculate the maximum and minimum airmass values for each filter. Since the airmass of the observation will vary in three dimensions (duration of time, right ascension and declination), the effect of the first-order extinction will vary. The maximum and minimum effects based on the change in airmass are presented in four pairs of columns in Table 5.2.

Table 5.2 Extinction Effect

Interval Over:	Max ΔX B filter	ΔM_B (mmag)	Max ΔX V filter	ΔM_V (mmag)	Min ΔX B filter	ΔM_B (mmag)	Min ΔX V filter	ΔM_V (mmag)
Time	0.019	7.2	0.011	2.7	0.00005	0.02	0.00003	0.01
Dec.	0.021	8.1	0.024	5.9	0.007	2.7	0.007	1.8
R.A.	0.022	8.6	0.026	6.4	0.00006	0.02	0.00008	0.02

First-order extinction effects will also cause a scatter in nightly data. For example, in Figure 5.12, each night's data makes column of data points. The first night in particular, where airmasses range from 1.7 to 1.8, we find that the scatter between images is about 34 millimagnitudes from beginning to end. Using Table 5.2, we find that the maximum contribution from the time duration of five images would be 36 millimagnitudes¹. This shows that the scatter in one night is less than the maximum contribution of first-order extinction. By correcting extinction across the frame, it would allow *Ensemble Photometry* to correct the zero-points appropriately.

¹ This is using the maximum extinction values for the B filter because the light curve is plotted in B magnitude versus Julian date.

Chapter 6. Conclusions

6.1 Summary of Research

6.1.1 Observations and Procedure

Observations were made at Fick Observatory. 311 science images were acquired over 21 nights stretching just over two months. 156 science images were taken using the B and 155 images were taken using the V filter.

General data reduction was completed with *IRAF*. After extracting stellar information, the images are processed with *Tim Naylor's Optimal Photometry* software where the aperture photometry method was determined to be superior for our data. After color corrections, the data was processed with *Ensemble Photometry* to use the series of exposures and constant stars to our benefit. This program also designates variable stars using an objective algorithm and can be fine-tuned to provide the best results.

6.1.2 Variability

The analysis of the data yielded four variable stars, each of which is a known binary system. Their variability was verified with Stassun et al. (2002) and the expected conditions of their variability and light curves were matched. This gives us confidence that: 1) our photometry is reliable, and 2) the variable detection method we employed is successful. A fifth 'variable' star was declined after realizing that the sky background contributes about 10 % to the noise of this star.

Though *Ensemble Photometry* did not detect other variable stars, our analysis suggests that more variable stars would be detected with a lower variability threshold. An example of this is the detection of the RS CVn variable system. This system is well known to exhibit variability, but even the high uncertainty of this star is too low to be flagged as a variable star with the current *Ensemble Photometry* settings.

Other stars with relatively-high uncertainties were found. Most of these stars have uncertainties that are smaller than the standard deviation at their magnitudes. Higher levels of uncertainty are likely due to vignetting effects at the corners of images or the edges of the frame.

6.1.3 Small Research-Grade Telescope Limitations

Overall, there are several limitations when using this telescope: 1) the sky brightness is close to 21 magnitudes per square arcsecond on a moonless, clear night (Cinzano et al. 2001). Any photometric observations with precisions better than 10 millimagnitudes must be at $M_V < 19$. 2) Extinction will lower the limiting magnitude of observations further. Error due to extinction is about 8 millimagnitudes for intermediate airmasses from the duration of a two-minute exposure alone. The effect is larger when comparing two stars that are not near each other.

Overall I do think that further investigation of this cluster will result in precisions to at least 10 millimagnitudes for Sun-like stars and with statistical manipulation we may be able to reach higher precisions. This decrease in

uncertainty will also decrease the contribution of error from some steps, including both color-corrections and *Ensemble Photometry*.

6.2 Suggestions for Improvements

6.2.1 Longer Exposures

Longer exposures will reduce the uncertainties due to random errors, especially in fainter stars. Some brighter stars will be lost because of saturation. This should, however, result in a better ensemble correction and will lead to a higher precision of variable star detection. More importantly, *Ensemble Photometry* uncertainties would be minimized for the Sun-like region. A visual representation of how longer exposures would affect our data is available in Figure 6.1.

6.2.2 First-Order Extinction

The most significant problem is the first-order extinction error. In Section 5.4.3, we discuss that, since there is a gradient of airmass across the frame, there must also be a gradient in the first-order extinction. Since *Ensemble Photometry* uses all of the stars over each image to calculate an magnitudes and uncertainties, first-order extinction errors on some stars are a significant problem to all of the stars. To correct this, we have two methods.

6.2.2.1 Multiple Ensemble Photometry

When using a cluster of stars, we find that we have enough stars to complete ensemble photometry on a section of the image. For a section of the

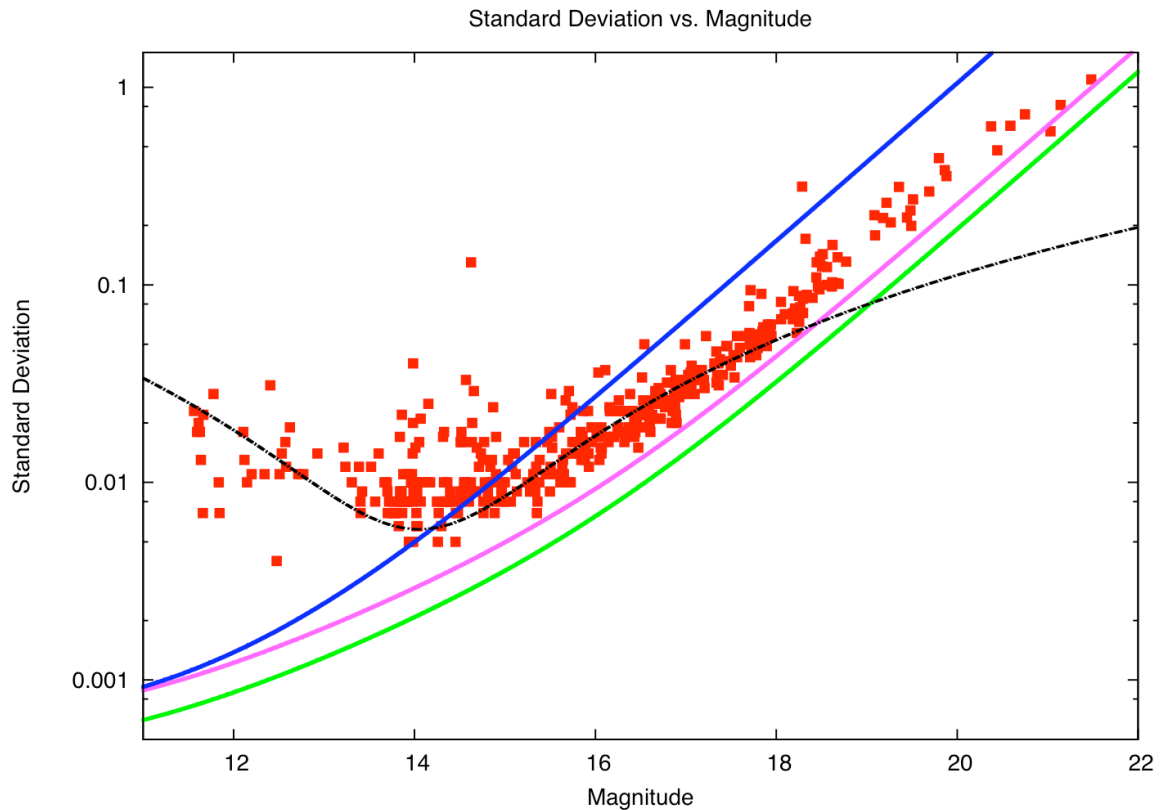


Figure 6.1 Standard deviation versus magnitude plot. The black curve is the parabola fit produced by *Ensemble Photometry*. The blue curve (top) is a theoretical model of where the data should be located during a full moon. The pink curve (middle) models where the data is expected for a clear night when the moon is not bright. The green curve (bottom) is the expected location of data for a clear, moonless night using the same conditions as the pink curve, except it uses a 4-minute exposure (double the original exposure time).

image, the first-order extinction gradient is smaller, resulting in a smaller error from first-order extinction. In order to complete this process, each section would need to overlap, so that stars near the edge of a section are not determined by using stars on the other side of the section where the effects of first-order extinction are largest.

6.2.2.2 Correction by Location

Since we know the location relative to the center of the image of each star, and we know the value of airmass of the center (and by proxy, each star), then we can estimate the amount of first-order extinction for each star. Once we know this, we can correct each star for this error.

6.2.2.3 Effects of First-Order Extinction over Time

It is important to note that in Section 5.4.2.6, we mention that group statistics can not be completed because of the scatter from image to image over a single night. This scatter is due to the change in airmass over the duration of the series of science images. Once first-order extinction effects are corrected across the frame, each image should have a zero-point offset that is related to the first-order extinction over the duration of images. In essence, removing errors across the frame will result in removing the errors due to time.

6.2.3 Vignetting Correction

Several stars were detected with unusually high uncertainties. We determined that this was due to vignetting effects. There are two types of vignetting effects: 1) 'corner vignetting', where the radius from the center of the frame is greater than 550 pixels, and 2) 'edge vignetting', where the star is close enough to the edge that the whole of the star may fall off of the sides of the image.

The ensemble process, where all stars are collectively used to determine the magnitude of each star, does not account for these effects. Because of this,

the precision of the output may be significantly effected. These stars must be removed from calculations in order to achieve the highest precision.

6.2.4 Longer Baseline

This study was limited to a baseline of one season or about 2 months of data. Stellar cycles are also known to be important on scales longer than one year (Lockwood et al. 1997; Pap et al. 1999). An extra season will give us the ability to look for variability along yearly baselines. The Sun, for instance varies most noticeably on an eleven year cycle but also on longer timescales. It is evident that long-term photometric monitoring should improve our chances of detecting solar-cycle-like activity.

6.2.5 Focus

In this research, we were not concerned with the focus of the images. This is because we were concerned with saturation of the brighter stars. With a slightly defocused system, we can make our exposures longer without stars saturating. However, because of this, we may have lost useful information (in the form of FWHM) about the seeing conditions. Without this estimate, we cannot characterize the effect of the weather conditions on our data.

Focusing the image to the best focus possible is one way to ensure that any information on the seeing conditions of an observation is retained. The disadvantage of using the best focus method is that the brighter stars will saturate, limiting the level at which your observations can be made.

If very dim and very bright stars are needed, a defocused image method would be preferred. Standardizing the amount that an image is defocused can be

done in several ways. The first way is to use three or four stars across the image and a range of expected FWHM for each. Deemed correct focus would be when each of the stars enter their respective range. One problem with this is that the FWHM changes with weather conditions as well as with focus.

Another way to standardize the focus is to find the best focus for a series of exposures, and then change the focus by an offset amount. The problem with this method is that we are assuming that focus adjustment is similar across the observations in a season. If it is not, then the focus offset must be a function of other variables, resulting in a complicated system.

Appendix A. Mathematica Code for Least-Squares Analysis

```

In[1]:= RA = {8.866564722, 8.866253056, 8.864819167, 8.863873889, 8.863650278, 8.863423056, 8.862957778,
8.862426667, 8.861451111, 8.862223611, 8.861791389, 8.862152222, 8.861854722, 8.861650278,
8.860896667, 8.860389722, 8.859937222, 8.860001944, 8.859520833, 8.858873333, 8.859048056,
8.858929167, 8.8581675, 8.858492222, 8.857999444, 8.858675833, 8.85786, 8.857615278,
8.857817222, 8.858153056, 8.857046111, 8.856689167, 8.856363611, 8.855213056, 8.855713611,
8.855280833, 8.855777778, 8.855588611, 8.855148611, 8.855189722, 8.854375556, 8.854996667,
8.854342222, 8.854260556, 8.854289167, 8.853777778, 8.854098611, 8.8523275, 8.852639444,
8.850047778, 8.850903333, 8.850292222, 8.849486667, 8.850227778}; Ra = RA * 15 Degree;
Dec = {11.88265556, 11.78138056, 11.80577222, 11.82530556, 11.82875, 11.85329167, 11.74943611,
11.77943056, 11.90804722, 11.77345833, 11.83107778, 11.75410833, 11.77679167, 11.72698333,
11.83437778, 11.83478056, 11.89295556, 11.77597778, 11.828825, 11.88657778, 11.84459722,
11.83431944, 11.90385278, 11.82031667, 11.86663611, 11.76404722, 11.87151111, 11.89069444,
11.82428611, 11.75765833, 11.79282778, 11.80606667, 11.81371111, 11.855175, 11.77120278,
11.83491389, 11.75067778, 11.77824444, 11.82261944, 11.78406389, 11.88298889, 11.76503889,
11.84892778, 11.83730278, 11.79205556, 11.84388611, 11.88998611, 11.78668611,
11.69582222, 11.90889722, 11.76315278, 11.83633889, 11.87285278, 11.66045278} * Degree;
α = 8.857916666666667; A = α * 15 Degree; δ = 11.803333333333333 Degree;
xcoord = {101.771, 151.028, 214.464, 255.038, 265.052, 268.177, 326.055, 342.539, 348.181,
354.634, 356.941, 364.751, 371.906, 398.736, 400.431, 425.587, 428.677, 464.585,
470.923, 483.865, 489.18, 498.544, 513.245, 525.002, 534.065, 534.698, 539.394,
545.182, 557.339, 562.895, 606.295, 619.647, 633.34, 676.788, 680.027, 680.204,
683.694, 683.869, 690.913, 701.819, 709.234, 717.827, 722.272, 730.232, 744.023,
752.128, 754.186, 843.605, 858.515, 916.196, 922.481, 928.392, 956.259, 990.731};
ycoord = {742.18, 399.679, 489.563, 560.514, 573.306, 657.759, 307.274, 411.77, 853.341,
392.556, 590.333, 327.204, 405.668, 237.477, 605.908, 609.763, 809.493, 411.956,
593.832, 793.062, 649.672, 615.366, 855.173, 569.933, 729.659, 377.912, 746.861,
813.217, 586.737, 358.837, 483.701, 530.495, 557.984, 704.427, 416.831, 635.285,
346.822, 441.355, 594.186, 463.086, 802.927, 399.421, 687.471, 648.418, 494.64,
673.114, 488.567, 486.061, 175.976, 912.201, 413.151, 664.638, 792.576, 67.768};

ξ = 1. / (Sin[δ] + Cos[δ] Cot[Dec] Cos[Ra - A]); η = 1. / (Sin[δ] - Cot[Dec] Sin[δ] Cos[Ra - A]);
a = {xcoord, ycoord, ξ}; b = {xcoord, ycoord, η}; c = Transpose[a]; d = Transpose[b];
SetPrecision[Fit[c, {1, x, y}, {x, y}], 15]
SetPrecision[Fit[d, {1, x, y}, {x, y}], 15]
SetPrecision[Fit[c, {1, x, y, x^2, x y, y^2}, {x, y}], 15]
SetPrecision[Fit[d, {1, x, y, x^2, x y, y^2}, {x, y}], 15]
SetPrecision[Fit[c, {1, x, y, x^2, x y, y^2, x y^2, y x^2, x^3, y^3}, {x, y}], 15]
SetPrecision[Fit[d, {1, x, y, x^2, x y, y^2, x y^2, y x^2, x^3, y^3}, {x, y}], 15]

Out[8]= 0.00310625809933254 - 5.09084943939770 × 10-6 x - 5.01861946906533 × 10-7 y

Out[9]= -0.00234176107744899 - 5.01167161570721 × 10-7 x + 5.09051818632381 × 10-6 y

Out[10]= 0.00310616773393655 - 5.08981078050208 × 10-6 x - 1.05251671754933 × 10-12 x2 -
5.02407856108819 × 10-7 y + 2.43339299393316 × 10-13 x y + 3.34087593886459 × 10-13 y2

Out[11]= -0.00234050046827004 - 5.02307020502874 × 10-7 x - 7.93452277291096 × 10-14 x2 +
5.08705692246195 × 10-6 y + 2.10751460228385 × 10-12 x y + 1.98217271085466 × 10-12 y2

Out[12]= 0.00310490477706993 - 5.08674624854262 × 10-6 x -
3.72373922824447 × 10-12 x2 + 8.54801289477169 × 10-16 x3 - 4.98267656015976 × 10-7 y -
5.36179500685205 × 10-12 x y + 1.87719243338701 × 10-15 x2 y -
4.22827086212270 × 10-12 y2 + 2.85719335947268 × 10-15 x y2 + 1.62596809636636 × 10-15 y3

Out[13]= -0.00233966652257528 - 5.04063309052118 × 10-7 x -
1.22893362852955 × 10-12 x2 + 2.02745108139211 × 10-15 x3 + 5.08436238809750 × 10-6 y +
9.50025112183833 × 10-12 x y - 3.24775252811529 × 10-15 x2 y +
3.38270370627516 × 10-12 y2 - 3.30652003128207 × 10-15 x y2 + 2.43193193527731 × 10-16 y3

```

Appendix B. C++ Code for Color-Correction

```

#include <iomanip>
#include <iostream>
#include <fstream>
#include <string>
#include <math.h>

using namespace std;

int main ()
{
    ifstream tin ("times2.dat",ios::in);
    string filename, hfile, vfile, checkfile,file,bfile;
    int toss1, toss2;

    tin>>filename>>toss1>>toss2;

    string dec1;
    int id, ra1, ra2, dec2,n;
    double bJD, vJD, vx, vy, bx, by, ra3, dec3, bam, bamerr, bom, bomerr, vam, vamerr, vom, vomerr, bvam, bvom, bvs,aal, oa1,bvamerr,bvomerr;
    double bas,bos,vas,vos,JD,JDerr;
    double a[3000]={0};
    double b[3000]={0};
    int flag[3000]={0};

    ifstream in ("h237.cat",ios::in);

    in>>bJD>>vJD>>id>>bx>>by>>vx>>vy>>ra1>>ra2>>ra3>>dec1>>dec2>>dec3>>vam>>vamerr>>vom>>vomerr>>bam>>bamerr>>bom>>bomerr>>bvam>>bvom;

    while(tin.eof())
    {
        a[id]=bx;
        b[id]=by;
        flag[id]=1;
        in>>bJD>>vJD>>id>>bx>>by>>vx>>vy>>ra1>>ra2>>ra3>>dec1>>dec2>>dec3>>vam>>vamerr>>vom>>vomerr>>bam>>bamerr>>bom>>bomerr>>bvam>>bvom;
    };

    in.close();

    ofstream blist ("b.lst");
    ofstream vlist ("v.lst");

    while(!tin.eof())
    {
        filename=filename.erase(0,2);
        filename=filename.erase(filename.length()-4,4);
        bfile="b"+filename+".cat";
        vfile="v"+filename+".cat";
        hfile="h"+filename+".cat";
        file=filename.erase(filename.length()-1,1);
        blist<<bfile<<endl;
        vlist<<vfile<<endl;

        ifstream in (hfile.c_str(),ios::in);
        ofstream bout (bfile.c_str());
        ofstream vout (vfile.c_str());
        in>>bJD>>vJD>>id>>bx>>by>>vx>>vy>>ra1>>ra2>>ra3>>dec1>>dec2>>dec3>>vam>>vamerr>>vom>>vomerr>>bam>>bamerr>>bom>>bomerr>>bvam>>bvom;
        while(!in.eof())
        {
            if (strcmp(file.c_str(),"11")==0)
            {
                aal=1.193604;
                oa1=1.186314;
            }
            else if (strcmp(file.c_str(),"12")==0)
            {
                aal=1.323218;
                oa1=1.302816;
            }
            else if (strcmp(file.c_str(),"13")==0)
            {
                aal=1.295758333;
                oa1=1.207418333;
            }
            else if (strcmp(file.c_str(),"14")==0)
            {
                aal=1.329461667;
                oa1=1.16474;
            }
            else if (strcmp(file.c_str(),"15")==0)
            {
                aal=1.28197;
                oa1=1.283794286;
            }
            else if (strcmp(file.c_str(),"21")==0)
            {
                aal=1.187904444;
                oa1=1.214828889;
            }
            else if (strcmp(file.c_str(),"22")==0)
            {
                aal=1.307126667;
                oa1=1.149346222;
            }
            else if (strcmp(file.c_str(),"23")==0)
            {
                aal=1.281702857;
                oa1=1.226258571;
            }
            else if (strcmp(file.c_str(),"31")==0)
            {
                aal=1.323138;
                oa1=1.32866;
            }
            else if (strcmp(file.c_str(),"32")==0)
            {
                aal=1.338383;
                oa1=1.0045878;
            }
            else if (strcmp(file.c_str(),"33")==0)
            {
                aal=1.242645;
                oa1=1.1609766;
            }
            else if (strcmp(file.c_str(),"41")==0)
            {
                aal=1.276075;
                oa1=1.251093333;
            }
        }
    }
}

```



```

    } else if (strcmp(file.c_str(),"42")==0)
    {
        aa1=1.291533333;
        oa1=1.314222222;
    } else if (strcmp(file.c_str(),"43")==0)
    {
        aa1=1.24326;
        oa1=1.267745;
    } else if (strcmp(file.c_str(),"44")==0)
    {
        aa1=1.291648333;
        oa1=1.293748333;
    } else if (strcmp(file.c_str(),"51")==0)
    {
        aa1=1.314934444;
        oa1=1.324857778;
    } else if (strcmp(file.c_str(),"52")==0)
    {
        aa1=1.280806667;
        oa1=1.286647778;
    } else if (strcmp(file.c_str(),"53")==0)
    {
        aa1=1.208877778;
        oa1=1.005618444;
    } else if (strcmp(file.c_str(),"61")==0)
    {
        aa1=1.294505;
        oa1=1.302765;
    } else if (strcmp(file.c_str(),"62")==0)
    {
        aa1=1.318493333;
        oa1=1.331768333;
    } else if (strcmp(file.c_str(),"63")==0)
    {
        aa1=1.328961429;
        oa1=1.35013;
    } else
    {
        cout<<"data not found!";
        return 0;
    }
};

bas=bam-aa1*bvam;
vas=vam-aa1*bvam;

bos=bom-oa1*bvom;
vos=vom-oa1*bvom;

if (flag[id]==1)
{
    vout<<fixed<<setprecision(6)<<vJD<<" "<<setprecision(3)<<" "<<a[id]<<" "<<b[id]<<" "<<vas<<" "<<vamerr<<" "<<vos<<" "<<vomerr<<endl;
    bout<<fixed<<setprecision(6)<<bJD<<" "<<setprecision(3)<<" "<<a[id]<<" "<<b[id]<<" "<<bas<<" "<<bamerr<<" "<<bos<<" "<<bomerr<<endl;
};

in>>bJD>>vJD>>id>>bx>>by>>vx>>vy>>ra1>>ra2>>ra3>>dec1>>dec2>>dec3>>vam>>vamerr>>vom>>vomerr>>bam>>bamerr>>bom>>bomerr>>bvam>>bvom;
};

bout.close();
vout.close();

tin>>filename>>toss1>>toss2;
cout<<chfile<<endl;

};

tin.close();
vlist.close();
blist.close();

id=1;

ofstream out ("starlist.cat");

while(id<3000)
{
    if (flag[id]==1)
    {
        out<<id<<" "<<a[id]<<" "<<b[id]<<endl;
    };

    id++;
};
out.close();
return 0;
}

```

Appendix C. C++ Code for Categorization and Group Statistics

```
#include <iomanip>
#include <iostream>
#include <fstream>
#include <string>
#include <math.h>
#include <stdio.h>

using namespace std;

int main () {
    int hilo[22]={0,5,10,16,22,29,38,47,54,64,74,84,90,99,105,111,120,129,138,144,150,157};
    int index,image, dummyint,dummyvar,star, s, c, p, i,j,increm[22]={0}, q, id[465]={0}, m[465]={0}, starsused[160][2]={0}, starsmatch[160][2]={0}, sat[465][160][2]={0};
    var[465][2]={0};
    double dummydouble, a, b, k, l, dummymag, dummyweight, dummymag2, dummyvarscore, dummyerr, n[22][33]={0}, cmag[22][11][2]={0}, x[465]={0}, y[465]={0}, jd[160][2]={0};
    eid[465]={0}, origmag[465][160][2]={0}, weight[465][160][2]={0}, avemag[465][2]={0}, cormag[465][160][2]={0}, magerr[465][160][2]={0},
    varscore[465][2]={0}, zero[160][2]={0}, rmsoff[160][2]={0}, rmsoffdivsqn[160][2]={0}, trumagerr[465][2]={0};
    char dummychar[10];
    string dummystring, filename[160][2], name;
    ifstream in;
    ofstream out, bout("./output/binage.dat"), vout("./output/vimage.dat"), mout("./output/members.cat"), maout("./output/exceptnm.cat"), sout("./output/stars.cat");
    //////////////////////////////////////
    in.open("compiled1.dat",ios::in);
    for(index=0;in.eof();index++) in>>id[index]>>x[index]>>y[index]>>m[index]; // LOADING previously compiled data
    in.close();
    cout<<"Compiled Data File Load Complete..."<<endl;
    //////////////////////////////////////
    in.open("b.out",ios::in);
    in>>dummyint>>dummystring>>dummyint>>dummystring;
    for(index=0;index<157;index++) in>>image>>filename[index][0]>>dummydouble>>jd[index][0]>>starsused[index][0]>>starsmatch[index][0];
    while(in.eof()) {
        in>>star>>a>>b>>c;
        for(index=0;index<465;index++)
            if(x[index]==a && y[index]==b) {
                for(i=0;i<c;i++) {
                    in>>star>>image>>a>>b>>s>>dummymag>>dummyweight; //LOADING the Multipt Output File Part 1
                    origmag[index][image][0]=dummymag;
                    weight[index][image][0]=dummyweight;
                    eid[index]=star;
                    sat[index][image][0]=s;
                }
                break;
            }
    }
    in.close();
    in.open("v.out",ios::in);
    in>>dummyint>>dummystring>>dummyint>>dummystring;
    for(index=0;index<157;index++) {
        in>>image>>filename[index][1]>>dummydouble>>jd[index][1]>>starsused[index][1]>>starsmatch[index][1];
    };
    while(in.eof()) {
        in>>star>>a>>b>>c;
        for(index=0;index<465;index++)
            if(x[index]==a && y[index]==b) {
                for(i=0;i<c;i++) {
                    in>>star>>image>>a>>b>>s>>dummymag>>dummyweight; //LOADING the Multipt Output File Part 2
                    origmag[index][image][1]=dummymag;
                    weight[index][image][1]=dummyweight;
                    eid[index]=star;
                    sat[index][image][1]=s;
                }
                break;
            }
    }
    in.close();
    cout<<"Multipt Output File Data Load Complete..."<<endl;
    //////////////////////////////////////
    in.open("b37.cat",ios::in);
    in>>star>>a>>b>>image>>dummydouble>>dummymag>>dummymag2>>dummyerr>>dummyvar>>dummyvarscore;
    while(in.eof()) {
        for(index=0;index<465;index++)
            if(x[index]==a && y[index]==b && eid[index]==star && dummyerr!=99) {
                avemag[index][0]=dummymag;
                cormag[index][image][0]=dummymag2; // Loading the B Catalogue File
                magerr[index][image][0]=dummyerr;
                var[index][0]=dummyvar;
                varscore[index][0]=dummyvarscore;
            }
        in>>star>>a>>b>>image>>dummydouble>>dummymag>>dummymag2>>dummyerr>>dummyvar>>dummyvarscore;
    }
    in.close();
    in.open("v22.cat",ios::in);
    in>>star>>a>>b>>image>>dummydouble>>dummymag>>dummymag2>>dummyerr>>dummyvar>>dummyvarscore;
    while(in.eof()) {
        for(index=0;index<465;index++)
            if(x[index]==a && y[index]==b && eid[index]==star && dummyerr!=99) {
                avemag[index][1]=dummymag;
                cormag[index][image][1]=dummymag2; // Loading the B Catalogue File
                magerr[index][image][1]=dummyerr;
                var[index][1]=dummyvar;
                varscore[index][1]=dummyvarscore;
            }
        in>>star>>a>>b>>image>>dummydouble>>dummymag>>dummymag2>>dummyerr>>dummyvar>>dummyvarscore;
    }
    in.close();
}
```

```

cout<<"Catalogue File Data Load Complete..."<<endl;
////////////////////////////////////////////////////////////////////////////////////////////////////////////////////////////////
in.open("b37.img",ios::in);
in>>image;
in>>dummystring>>dummydouble>>dummydouble>>zero[image][0]>>rmsoff[image][0]>>rmsoffdivsqtrn[image][0];
while(!in.eof()) {
    in>>image;
    in>>dummystring>>dummydouble>>dummydouble>>zero[image][0]>>rmsoff[image][0]>>rmsoffdivsqtrn[image][0]; // Loading the B Image File
}
in.close();
in.open("v22.img",ios::in);
in>>image;
in>>dummystring>>dummydouble>>dummydouble>>zero[image][1]>>rmsoff[image][1]>>rmsoffdivsqtrn[image][1];
while(!in.eof()) {
    in>>image;
    in>>dummystring>>dummydouble>>dummydouble>>zero[image][1]>>rmsoff[image][1]>>rmsoffdivsqtrn[image][1]; // Loading the V Image File
}
in.close();
cout<<"Image File Data Load Complete..."<<endl;
////////////////////////////////////////////////////////////////////////////////////////////////////////////////////////////////
in.open("b37.sig",ios::in);
in>>stars>>dummymag>>dummyerr>>dummyvar>>dummyvarscore>>a>>b;
while(!in.eof()) {
    for(index=0;index<465;index++)
        if(x[index]==a && y[index]==b && eid[index]==star) trumagerr[index][0]=dummyerr; // Loading the B Sig File
    in>>stars>>dummymag>>dummyerr>>dummyvar>>dummyvarscore>>a>>b;
}
in.close();
in.open("v22.sig",ios::in);
in>>stars>>dummymag>>dummyerr>>dummyvar>>dummyvarscore>>a>>b;
while(!in.eof()) {
    for(index=0;index<465;index++)
        if(x[index]==a && y[index]==b && eid[index]==star) trumagerr[index][1]=dummyerr; // Loading the V Sig File
    in>>stars>>dummymag>>dummyerr>>dummyvar>>dummyvarscore>>a>>b;
}
in.close();
cout<<"Sigma File Data Load Complete..."<<endl;
////////////////////////////////////////////////////////////////////////////////////////////////////////////////////////////////
for(index=0;index<157;index++) {
    if(zero[index][0]>0) bout<<index<<" "<<filename[index][0]<<" "<<fixed<<setprecision(6)<<jd[index][0]<<setprecision(3)<<" "<<zero[index][0]<<" "<<rmsoff[index][0]<<"
"<<rmsoffdivsqtrn[index][0]<<" "<<starsused[index][0]<<" "<<starsmatch[index][0]<<endl;
    if(zero[index][1]>0) vout<<index<<" "<<filename[index][1]<<" "<<fixed<<setprecision(6)<<jd[index][1]<<setprecision(3)<<" "<<zero[index][1]<<" "<<rmsoff[index][1]<<"
"<<rmsoffdivsqtrn[index][1]<<" "<<starsused[index][1]<<" "<<starsmatch[index][1]<<endl;
}
bout.close(); // Image Information Output
vout.close();
cout<<"Beginning distribution of data into various files, this could take some time..."<<endl;
////////////////////////////////////////////////////////////////////////////////////////////////////////////////////////////////
vout.open("./output/vars.cat");
for(index=0;index<465;index++) {
    sprintf(dummychar,"%d",id[index]);
    dummystring="";
    dummystring=dummystring+dummychar; // Full Starly Information Output
    name="./Stars/star"+dummystring+".cat";
    out.open(name.c_str());
    if(avemag[index][0]!=0)sout<<id[index]<<" "<<eid[index]<<" "<<m[index]<<" "<<avemag[index][0]<<" "<<avemag[index][1]<<" "<<avemag[index][0]-avemag[index][1]<<"
"<<trumagerr[index][0]<<" "<<trumagerr[index][1]<<" "<<sqrt((trumagerr[index][0])*(trumagerr[index][0])+(trumagerr[index][1])*(trumagerr[index][1]))<<" "<<var[index][0]<<"
"<<var[index][1]<<" "<<varscore[index][0]<<" "<<varscore[index][1]<<endl;
    if(avemag[index][0]!=0 && m[index]==1) mout<<id[index]<<" "<<eid[index]<<" "<<m[index]<<" "<<avemag[index][0]<<" "<<avemag[index][1]<<"
"<<avemag[index][0]-avemag[index][1]<<" "<<trumagerr[index][0]<<" "<<trumagerr[index][1]<<"
"<<sqrt((trumagerr[index][0])*(trumagerr[index][0])+(trumagerr[index][1])*(trumagerr[index][1]))<<" "<<var[index][0]<<" "<<var[index][1]<<" "<<varscore[index][0]<<"
"<<varscore[index][1]<<endl;
    if(avemag[index][0]!=0 && (m[index]==1 || m[index]==2)) maout<<id[index]<<" "<<eid[index]<<" "<<m[index]<<" "<<avemag[index][0]<<" "<<avemag[index][1]<<"
"<<avemag[index][0]-avemag[index][1]<<" "<<trumagerr[index][0]<<" "<<trumagerr[index][1]<<"
"<<sqrt((trumagerr[index][0])*(trumagerr[index][0])+(trumagerr[index][1])*(trumagerr[index][1]))<<" "<<var[index][0]<<" "<<var[index][1]<<" "<<varscore[index][0]<<"
"<<varscore[index][1]<<endl;
    if(avemag[index][0]!=0 && var[index][0]!=0 && var[index][1]!=0) vout<<id[index]<<" "<<[index]<<" "<<y[index]<<" "<<eid[index]<<" "<<m[index]<<" "<<avemag[index][0]<<"
"<<avemag[index][1]<<" "<<avemag[index][0]-avemag[index][1]<<" "<<trumagerr[index][0]<<" "<<trumagerr[index][1]<<"
"<<sqrt((trumagerr[index][0])*(trumagerr[index][0])+(trumagerr[index][1])*(trumagerr[index][1]))<<" "<<var[index][0]<<" "<<var[index][1]<<" "<<varscore[index][0]<<"
"<<varscore[index][1]<<endl;
    for(i=0;i<157;i++) if(cormag[index][i][1]!=cormag[index][i][0] && cormag[index][i][1]!=0 && cormag[index][i][0]!=0) out<<id[index]<<" "<<eid[index]<<" "<<m[index]<<"
"<<var[index][0]<<" "<<var[index][1]<<" "<<varscore[index][0]<<" "<<varscore[index][1]<<" "<<avemag[index][0]<<" "<<avemag[index][1]<<" "<<trumagerr[index][0]<<"
"<<trumagerr[index][1]<<" "<<origmag[index][i][0]<<" "<<origmag[index][i][1]<<" "<<cormag[index][i][0]<<" "<<cormag[index][i][1]<<" "<<magerr[index][i][0]<<"
"<<magerr[index][i][1]<<" "<<sat[index][i][0]<<" "<<sat[index][i][1]<<" "<<weight[index][i][0]<<" "<<weight[index][i][1]<<" "<<filename[i][0]<<" "<<filename[i][1]<<"
"<<starsused[i][0]<<" "<<starsused[i][1]<<" "<<starsmatch[i][0]<<" "<<starsmatch[i][1]<<" "<<fixed<<setprecision(6)<<jd[i][0]-2454000.000<<" "<<jd[i][1]-2454000.
000<<setprecision(3)<<" "<<zero[i][0]<<" "<<zero[i][1]<<" "<<rmsoff[i][0]<<" "<<rmsoff[i][1]<<" "<<rmsoffdivsqtrn[i][0]<<" "<<rmsoffdivsqtrn[i][1]<<endl;
    out.close();
}
mout.close();
sout.close();
vout.close();
////////////////////////////////////////////////////////////////////////////////////////////////////////////////////////////////
for(q=1;q<22;q++) {
    sprintf(dummychar,"%d",q);
    dummystring="";
    dummystring=dummystring+dummychar;
    name="./night/night"+dummystring+".cat";
    mout.open(name.c_str());
    mout.close();
}
////////////////////////////////////////////////////////////////////////////////////////////////////////////////////////////////
for(index=0;index<465;index++) {
    sprintf(dummychar,"%d",id[index]);
    dummystring="";
}

```

```

dummystring=dummystring+dummychar;
name="./nights/star"+dummystring+".cat"; //Compiling Nightly Data
out.open(name.c_str());
for(q=1;q<22;q++) {
    for(i=0;i<157;i++) n[q][i]=0.0000;
    increm[q]=0;
    for(i=hilo[q-1];i<hilo[q];i++) {
        if(cormag[index][i][1]!=cormag[index][i][0] && (cormag[index][i][1]!=0 && cormag[index][i][0]!=0))
        {
            n[q][0]=n[q][0]+id[index]; //Star ID from Balaguer-Nunez
            n[q][1]=n[q][1]+eid[index]; //Star ID from Ensemble
            n[q][2]=n[q][2]+m[index]; //Membership 1=yes, 0=no, 2=I don't know
            n[q][3]=n[q][3]+var[index][0]; //B Filter Variability 1=yes, 0=no
            n[q][4]=n[q][4]+var[index][1]; //V Filter Variability 1=yes, 0=no
            n[q][5]=n[q][5]+varscore[index][0]; //B Filter Variability Score
            n[q][6]=n[q][6]+varscore[index][1]; //V Filter Variability Score
            n[q][7]=n[q][7]+avemag[index][0]; //B Filter Average Magnitude over All Images
            n[q][8]=n[q][8]+avemag[index][1]; //V Filter Average Magnitude over All Images
            n[q][9]=n[q][9]+trumagerr[index][0]; //B Filter Error from Average Magnitudes
            n[q][10]=n[q][10]+trumagerr[index][1]; //V Filter Error from Average Magnitudes
            n[q][11]=n[q][11]+origmag[index][i][0]; //B Filter Original Magnitude from Multipt
            n[q][12]=n[q][12]+origmag[index][i][1]; //V Filter Original Magnitude from Multipt
            n[q][13]=n[q][13]+cormag[index][i][0]; //B Filter Corrected Magnitude from Multipt
            n[q][14]=n[q][14]+cormag[index][i][1]; //V Filter Corrected Magnitude from Multipt
            n[q][15]=n[q][15]+magerr[index][i][0]; //B Filter Uncertainty
            n[q][16]=n[q][16]+magerr[index][i][1]; //V Filter Uncertainty
            n[q][17]=n[q][17]+sat[index][i][0]; //B Saturation 1=yes, 2=no
            n[q][18]=n[q][18]+sat[index][i][1]; //V Saturation 1=yes, 2=no
            n[q][19]=n[q][19]+weight[index][i][0]; //B Filter Weight = 1/sigma^2
            n[q][20]=n[q][20]+weight[index][i][1]; //V Filter Weight = 1/sigma^2
            n[q][21]=n[q][21]+(jd[i][0]-2454000.0000); //Julian Date of B Filter image
            n[q][22]=n[q][22]+(jd[i][1]-2454000.0000); //Julian Date of V Filter image
            cmag[q][increm[q][0]]=cormag[index][i][0]; //Corrected Magnitude Set for determining Standard Deviations
            cmag[q][increm[q][1]]=cormag[index][i][1]; //Corrected Magnitude Set for determining Standard Deviations
            increm[q]++; //Number of images applied for averages
        }
    }
    for(i=0;i<23;i++) if(increm[q]>0) n[q][i]=(n[q][i])/(double(increm[q]));
    if(n[q][0]!=0) {
        n[q][23]=0.0000;
        n[q][24]=0.0000;
        for(j=0;j<increm[q];j++) {
            if(q==1 && n[q][0]==965) cout<<endl<<c<<" "<<n[q][23]<<" "<<cmag[q][j][0]<<" "<<cmag[q][j][1]<<" "<<cormag[index][j][0]<<" "<<cormag[index][j][1]<<"
"<<n[q][13]<<endl;
            if(cmag[q][j][0]!=0.0000) n[q][23]=n[q][23]+cmag[q][j][0]-n[q][13])*cmag[q][j][0]-n[q][13]);
            if(cmag[q][j][1]!=0.0000) n[q][24]=n[q][24]+cmag[q][j][1]-n[q][14])*cmag[q][j][1]-n[q][14]);
        }
    }
}
for(q=1;q<22;q++) {
    sprintf(dummychar,"%d",q);
    dummystring="";
    dummystring=dummystring+dummychar;
    name="./night/night"+dummystring+".cat";
    mout.open(name.c_str(), ios::app);
    if(n[q][0]!=0) {
        for(i=0;i<23;i++){
            if(n[q][0]!=0) mout<<n[q][i]<<" ";
            n[q][23]=sqrt(n[q][23]/double(increm[q])); //Standard Deviation from Mean
            n[q][24]=sqrt(n[q][24]/double(increm[q])); //Standard Deviation from Mean
            n[q][25]=n[q][23]/sqrt(double(increm[q])); //Standard Deviation of the Mean
            n[q][26]=n[q][24]/sqrt(double(increm[q])); //Standard Deviation of the Mean
            n[q][27]=n[q][13]-n[q][14]; //B-V of Nightly Corrected Mean Magnitudes
            n[q][28]=sqrt(n[q][25]*n[q][25]+n[q][26]*n[q][26]);
        }
        p=0;
        for (j=q;j>0;j--) {
            n[q][29]=n[q][29]+n[j][13];
            n[q][30]=n[q][30]+n[j][14];
            n[q][31]=n[q][31]+n[j][25];
            n[q][32]=n[q][32]+n[j][26];
            if (n[q][29]==0) p--;
            p++;
        }
        for (j=29;j<33;j++) n[q][j]=n[q][j]/double(p);
        for(i=23;i<33;i++) mout<<n[q][i]<<" "; //Output of Night-to-Night Data
        mout<<endl;
    }
    mout.close();
}
for(i=1;i<22;i++)
    if(n[i][0]!=0) {
        out<<" ";
        for(j=0;j<33;j++) out<<n[i][j]<<" "; //Output of Night-Averaged Starly Data
        out<<endl;
    }
    out.close();
}
cout<<endl;
return 0;
}

```

Bibliography

- [1] Arfken, G. and Weber, H., 2005, *Mathematical Methods for Physicists*, 6th ed., Amsterdam: Elsevier Academic Press.
- [2] Balaguer-Núñez, L., Galadí-Enríquez, D. and Jordi, C., 2007, *A&A*, vol.470, pp. 585-596.
- [3] Belloni, T., Verbunt, F. and Mathieu, R.D., 1998, *A&A*, vol.339, pp. 431-439.
- [4] Bessel, M.S., 1990, *PASP*, vol.102, pp. 1181-1199.
- [5] Bevington, P.R, 1969, *Data Reduction and Error Analysis for the Physical Sciences*, New York: McGraw-Hill.
- [6] Binney, J. and Merrifield, M., 1998, *Galactic Astronomy*, Princeton: Princeton University Press.
- [7] Birney, D.S., Gonzalez, G., and Oesper, D., 2006, *Observational Astronomy*, 2nd ed., Cambridge: Cambridge University Press.
- [8] Bonnarel, F., Fernique, P., Bienayme, O., Egret, D., Genova, F., Louys, M., Ochsenbein, F., Wenger, M., and Bartlett, J.G., 2000, *A&AS*, vol.143, pp. 33-40.
- [9] Bryan, J., 2001, *J.Br.Astron.Assoc.*, vol.111, pp. 29-32.
- [10] Buchheim, B., 2005, *The Society for Astronomical Sciences Symposium on Telescope Science*, vol.24, pp. 111-119.
- [11] Cinzano, P., Falchi, F., and Elvidge, C.D., 2001, *MNRAS*, vol.328, pp.689-707.
- [12] Cox, A.N., 1999, *Allen's Astrophysical Quantities*, 4th ed., New York: Springer.

- [13] Chromey, F.R. and Hasselbacher, D.A., 1996, *PASP*, vol.108, pp. 944-949.
- [14] Eggen, O.J. and Sandage, A.R., 1964, *ApJ*, vol.140, pp. 130-143.
- [15] Francic, S.P., 1989, *AJ*, vol.98, pp. 888-925.
- [16] Giampapa, M.S., Radick, R.R., Hall, J.C. and Baliunas, S.L., 2000, *BAAS*, vol.32, p. 832.
- [17] Giampapa, M.S., Hall, J.C., Radick, R.R. and Baliunas, S.L., 2006, *ApJ*, vol.651, pp. 444-461.
- [18] Girard, T.M., Grundy, W.M., López, C.E. and van Altena, W.F., 1989, *AJ*, vol.98, pp.227-243.
- [19] Grevesse, N. and Sauval, A.J., 1998, *Space Science Reviews*, vol.85, pp. 161-174.
- [20] Iben, I., 1967, *Annual Review of Astronomy & Astrophysics*, vol.5, pp. 571-626.
- [21] Honeycutt, R.K., 1992, *PASP*, vol.104, pp. 435-440.
- [22] Johnson, H.L. and Morgan, W.W., 1953, *ApJ*, vol.117, pp. 313-352.
- [23] Johnson, H.L. and Sandage, A.R., 1955, *ApJ*, vol.121, pp. 616-627.
- [24] Jones, B.F., 1997, *Memorie della Società Astronomica Italiana*, vol.68, pp. 833-844.
- [25] Jones, B.F. and Walker, M.F., 1988, *AJ*, vol.95, pp. 1755-1782.
- [26] Kharchenko, N.V., Piskunov, A.E., Röser, S., Schilbach, E. and Scholz, R.-D., 2005, *A&A*, vol.438, pp. 1163-1173.
- [27] Landolt, A.U., 1992, *AJ*, vol.104, pp. 340-371, 436-491.
- [28] Lean, J.L. and Rind, D., 2001, *Science*, vol.292, pp. 234-236.

- [29] Lockwood, G.W., Skiff, B.A. and Radick, R.R., 1997, *ApJ*, vol.485, pp. 789-811.
- [30] Lockwood, G.W., Skiff, B.A., Henry, G.W., Henry, S., Radick, R.R., Baliunas, S.L., Donahue, R.A. and Soon, W., 2007, *ApJS*, vol.171, pp. 260-303.
- [31] Loktin, A.V. and Beshenov, G.V., 2002, *Astronomy Reports*, vol.47, pp. 6-10.
- [32] Montgomery, K.A., Marschall, L.A. and Janes, K.A., 1993, *AJ*, vol.106, pp. 181-219.
- [33] Ostlie, D.A. and Carroll, B.W., 2007, *An Introduction to Modern Stellar Astrophysics, 2nd Ed.*, San Francisco: Pearson Addison-Wesley.
- [34] Pap, J., Anklin, M., Frölich, C., Wehrli, C., Varadi, F. and Linton, F., 1999, *Advances in Space Research*, vol.24, pp. 215-224.
- [35] Racine, R., 1971, *AJ*, vol.168, pp. 393-404.
- [36] Randich, S., Sestito, P., Primas, F., Pallavicini, R. and Pasquini, L., 2006, *A&A*, vol.450, pp. 557-567.
- [37] Sanders, W.L., 1971, *A&A*, vol.14, pp. 226-232.
- [38] Sanders, W.L., 1977, *A&AS*, vol.27, pp. 89-116.
- [39] Sandquist, E.L., 2003, *MNRAS*, *astroph/0308547*
- [40] Sandquist, E.L., Latham, D.W., Shetrone, M.D. and Milone, A.A.E., 2003, *AJ*, vol.125, pp. 810-824.
- [41] Sandquist, E.L. and Shetrone, M.D., 2003, *AJ*, vol.125, pp. 2173-2187.

- [42] Stassun, K.G., van den Berg, M., Mathieu, R.D. and Verbunt, F., 2002, *A&A*, vol.382, pp. 899-909.
- [43] Stritzinger, M., Suntzeff, N.B., Hamuy, M., Challis, P., Demarco, R., Germany, R. and Soderberg, A.M., 2005, *PASP*, vol.117, pp. 810-812.
- [44] Tadross, A.L., Werner P., Osman A., Marie, M., 2002, *New Astronomy*, vol.7, pp. 553-575.
- [45] Taylor, B.J., 2007, *AJ*, vol.133, pp. 370-386.
- [46] Vandenberg, D.A., 1985, *ApJS*, vol.58, p. 711-769.
- [47] Vandenberg, D.A., Gustafsson, B., Evardsson, B., Eriksson, K. and Ferguson, J., 2007, *ApJ*, vol.666, L105-L108.
- [48] van den Berg, M., Orosz, J., Verbunt, F. and Stassun, K., 2001, *A&A*, vol.375, pp. 375-386.
- [49] van den Berg, M., Stassun, K.G., Verbunt, F. and Mathieu, R.D., 2002, *A&A*, vol.382, pp. 888-898.
- [50] Willson, R.C. and Hudson, H.S., 1981, *ApJ*, vol.244, pp. L185-L189.
- [51] Xin, Y. and Deng, L., 2005, *ApJ*, vol.619, pp. 824-838.
- [52] Yadav, R.K.S., Bedin, L.R., Piotto, G., Anderson, J., Cassisi, S., Villanova, S., Platais, I., Pasquini, L., Momany, Y. and Sagar, R., 2008, *A&A*, *astroph/0803.0004*
- [53] Zacharias, N., Urban, S.E., Zacharias, M.L., Wycoff, G.L., Hall, D.M., Monet, D.G. and Rafferty, T.J., 2004, *AJ*, vol.127, pp. 3043-3059.
- [54] Zhao, J.L., Tian, K.P., Pan, R.S., He, Y.P. and Shi, H.M., 1993, *A&AS*, vol.100, pp. 243-261